

KINETIC CHARACTERIZATION OF CATALYSIS BY OXALATE DECARBOXYLASE
USING MEMBRANE INLET MASS SPECTROMETRY

By

MARIO EDGAR GABUA MORAL

A DISSERTATION PRESENTED TO THE GRADUATE SCHOOL
OF THE UNIVERSITY OF FLORIDA IN PARTIAL FULFILLMENT
OF THE REQUIREMENTS FOR THE DEGREE OF
DOCTOR OF PHILOSOPHY

UNIVERSITY OF FLORIDA

2011

© 2011 Mario Edgar Gabua Moral

To my parents, my sister, and my late grandparents

ACKNOWLEDGMENTS

This project was supported by grants from the National Institutes of Health (NIH DK061666 & GM25154) and the National Science Foundation (CHE-0809725).

I would like to thank my committee members: Dr. David Silverman for the use of the modified Membrane Inlet Mass Spectrometer in his lab; Dr. Alex Angerhofer, for the continued support on the EPR side of the project; Dr. Nicole Horenstein; and Dr. Gail Fanucci for all the insights and useful discussions on enzyme kinetics and physical chemistry; and most especially, my research adviser Dr. Nigel G. J. Richards, for providing me a part in the oxalate decarboxylase project and in his collaborations which got us to where we are now.

I owe a debt of gratitude to Dr. Chingkuang Tu for the fruitful collaboration behind our MIMS experiments, and for inspiring my creativity in research through his innovativeness and insight on every scientific problem we had to process.

I would like to acknowledge Dr. Stephan Bornemann and his research group at the John Innes Institute in Norwich, U.K. for generously providing the plasmid containing the gene for the C-terminal polyhistidine tagged (His6-tagged) OxDC from *Bacillus subtilis*.

I am deeply grateful for my former research colleagues: Dr. Patricia Moussatche, Dr. Ellen Moomaw, and Erin Holmes for the invaluable skills I learned in the beginning of my research. I thank Dr. Witcha Imaram for his assistance with the EPR experiments, and Ms. Mithila Shukla for the characterization and generous provision of the tyrosine OxDC mutant Y200F. I especially would like to acknowledge the generosity of Dr. Giovanni Gadda and Dr. Kevin Francis of Georgia State University for the use of their Hansatech oxygen electrode in the early stages of this project.

I thank Dr. Cris Dancel for recruiting me to the graduate chemistry program of UF, Drs. Dodge and Jhoana Baluya, Lilibeth Salvador, Carmello Callueng, Benjamin Raterman, Dr. Mandy Blackburn, Dr. Modesto Chua, Dr. Flerida Carino, and Dr. Florecita de Guzman for all the encouragement and invaluable support throughout my graduate school.

Finally, I thank my sister Diane, my parents and late grandparents for instilling in me the value of hard work, perseverance, and faith.

TABLE OF CONTENTS

	<u>page</u>
ACKNOWLEDGMENTS.....	4
LIST OF TABLES.....	9
LIST OF FIGURES.....	10
LIST OF ABBREVIATIONS.....	13
ABSTRACT.....	14
CHAPTER	
1 BACKGROUND.....	16
<i>Bacillus subtilis</i> Oxalate Decarboxylase (<i>BsOxDC</i>) Structure and Reaction.....	16
Decarboxylase Activity Assays.....	22
Formate Dehydrogenase (FDH)-Coupled Assay.....	22
Fourier Transform Infrared (FTIR) Spectrophotometric Assay.....	23
Limitations of Current Decarboxylase Activity Assays.....	24
Membrane Inlet Mass Spectrometry (MIMS).....	25
Research Objectives.....	26
2 CHARACTERIZATION OF OXDC BY MEMBRANE INLET MASS SPECTROMETRY.....	27
Introduction.....	27
Reaction Vessel.....	27
Membrane Inlet Probe and (Electron Impact) Ionization.....	28
Mass Analyzer.....	29
Results and Discussion.....	31
Real-time Monitoring of catalysis.....	31
Reproducibility.....	35
Response time.....	36
Buffer conditions: Air equilibrated vs. O ₂ -depleted (He-bubbled).....	36
Background CO ₂ and Isotope-labeled substrate (¹³ C ₂ -oxalate).....	38
o-Phenylenediamine (o-PDA).....	39
Calibration.....	39
Data Analysis: Michaelis-Menten Kinetics.....	42
Steady state.....	42
Initial velocities.....	43
Sources of error.....	44
Kinetic constants (MIMS vs FDH).....	45
Experimental Section.....	48
Materials.....	48

	His ₆ -tagged Oxalate Decarboxylase Expression and Purification	49
	Formate Dehydrogenase (FDH)-Coupled Activity Assay	50
	Membrane Inlet Mass Spectrometry (MIMS)	50
	Reaction Mixtures.....	51
3	NITRIC OXIDE INHIBITION OF CATALYSIS BY OXDC	53
	Introduction	53
	Nitric Oxide as Dioxygen Mimic.....	53
	Nitric Oxide from NONOates	53
	Data Analysis: Inhibition	55
	Results and Discussion.....	61
	Reversible Inhibition of NO.....	61
	OxDC inhibition by DEA NONOate	65
	Dependence of OxDC inhibition on NONOate concentration.....	66
	Mode of Inhibition of NO	66
	Inhibition of NO on catalysis by site-specific mutants of OxDC.....	68
	Constant Wave Electron Paramagnetic Resonance (CW-EPR) Experiments..	72
	Experimental Section	74
	Materials.....	74
	His6-tagged Oxalate Decarboxylase Expression and Purification.....	74
	Untagged Recombinant Wild-type and C383S OxDC Mutant	75
	Membrane Inlet Mass Spectrometry (MIMS)	75
	Reaction Mixtures.....	75
	Continuous Wave EPR Measurements	76
4	SMALL ANION INHIBITION OF CATALYSIS BY OXDC	79
	Introduction	79
	Results and Discussion.....	79
	Catalytic Products	80
	Anionic Buffer Effects	82
	Nitrate and Nitrite	83
	Bicarbonate	84
	Azide and Thiocyanate	86
	Experimental Section	89
	His6-tagged Oxalate Decarboxylase Expression and Purification.....	89
	Membrane Inlet Mass Spectrometry (MIMS)	89
	Reaction Mixtures.....	89
	Anion Inhibition.....	89
	Initial Rates.....	90
	Mode of Inhibition and Statistical Estimation of Parameters.....	90
5	CONCLUSIONS AND FUTURE WORK	91
	MIMS and OxDC Catalysis	91
	Insights on Future Work.....	92

Michaelis Menten Complex of OxDC.....	92
Oxygen-binding site and Oxygen Dependence	93
MIMS and Site-specific Mutants	94
Effect of Periodate and biSulfite anions.....	95

APPENDIX

A EXPRESSION AND PURIFICATION OF BACILLUS SUBTILIS OXDC	96
B OXDC SEQUENCES AND ALIGNMENTS	99
LIST OF REFERENCES	102
BIOGRAPHICAL SKETCH.....	108

LIST OF TABLES

<u>Table</u>		<u>page</u>
2-1	Steady state constants for decarboxylation of oxalate catalyzed by polyhistidine-tagged OxDC measured by MIMS and by formate dehydrngenase coupled assay	47
3-1	Table of comparison between graphical features of Lineweaver-Burke and Hanes plots.....	61
3-2	Modes of Inhibition represented by Lineweaver Burke and Hanes Plots.....	61

LIST OF FIGURES

<u>Figure</u>	<u>page</u>
1-1 Reactions catalyzed by the three classes of oxalate-degrading enzymes.....	16
1-2 Ribbon structure of germin oxalate oxidase from <i>Hordeum vulgare</i>	17
1-3 Ribbon structure of <i>B. subtilis</i> oxalate decarboxylase hexamer, trimer, and monomeric unit.	18
1-4 Partial sequence alignment of OxDC with OxOx showing the conserved active-site lid glutamate in OxDC which is not present in OxOx.	18
1-5 Mn(II) centers of the <i>B subtilis</i> OxDC monomer and the conserved set of one glutamate and three histidine ligand-binding residues.....	19
1-6 Proposed mechanism of the <i>B. subtilis</i> OxDC catalyzed decarboxylation of oxalate.....	20
1-7 Coupling reaction of the FDH Assay for oxalate decarboxylases.	23
2-1 The membrane inlet inserted in an air-tight cell for mass spectrometric measurements.....	27
2-2 Picture of the modified MIMS instrument and block diagram illustrating the main components of the system.	28
2-3 Cartoon showing how the time-dependent growth in peak height of a selected signal is reillustrated as a progress curve on the monitor of the MIMS instrument.	30
2-4 Experimental scheme for air-equilibrated catalytic experiments.....	32
2-5 Ion currents (arbitrary scale) in the production of carbon dioxide from ¹² C and ¹³ C ₂ -labeled oxalate catalyzed by OxDC in air equilibrated buffer.....	32
2-6 Ion current in the production of ¹³ CO ₂ from ¹³ C ₂ -oxalate catalyzed by OxDC.....	35
2-7 Superimposed ion currents (arbitrary scale) of three separate experiments involving the production of ¹³ CO ₂ from ¹³ C ₂ -oxalate catalyzed by OxDC.....	36
2-8 Experimental scheme for oxygen depleted catalytic experiments.	37
2-9 Ion currents in the production of carbon dioxide from ¹² C and ¹³ C ₂ -labeled oxalate potassium oxalate catalyzed by OxDC in deoxygenated buffer.	37
2-10 Overlay of m/z 44 ion currents illustrating background CO ₂ detected from the air-equilibrated OxDC enzyme aliquot in the absence of substrate.	39

2-11	Ion current (arbitrary scale) at m/z 44 using the membrane inlet mass spectrometer observed using solutions of known CO ₂ content.....	40
2-12	Ion current (arbitrary scale) at m/z 32 using the membrane inlet mass spectrometer observed using solutions of calculated O ₂ content.	41
2-13	Example of deriving initial rates from a progress curve of CO ₂ formation.....	44
2-14	Accumulation of ¹³ CO ₂ in solution resulting from the catalysis by OxDC.....	45
2-15	Initial rates of the appearance of ¹³ CO ₂ in solutions resulting from catalysis of the decarboxylation of oxalate by OxDC.	46
2-16	Initial rates of catalysis by polyhistidine-tagged <i>B. subtilis</i> oxalate decarboxylase determined by the formate dehydrogenase-coupled endpoint assay	48
3-1	Structures of MAHMA / DEA NONOates at pH 8.5, and their respective reaction byproducts at pH ≤7	54
3-2	Modified experimental scheme for testing the effects of NO on catalysis by OxDC.....	55
3-3	Fundamental enzymatic reaction model.	57
3-4	Enzymatic scheme for competitive inhibition.	57
3-5	Enzymatic scheme for uncompetitive inhibition.	58
3-6	Enzymatic scheme for noncompetitive/mixed inhibition.....	59
3-7	Effect of NO on catalysis by C-terminally His ₆ -tagged OxDC.	62
3-8	Effect of N ₂ on catalytic inhibition by NO.	63
3-9	MIMS experiment showing the effect of adding MAHMA NONOate to OxDC during catalytic turnover.	64
3-10	MIMS experiments showing that OxDC inhibition is not dependent on the source of NO.	65
3-11	Dependence of OxDC inhibition on initial MAHMA NONOate concentration.	66
3-12	Mode of Inhibition of NO.....	67
3-13	Effect of NO on catalysis by untagged C383S OxDC mutant.	68
3-14	Effect of NO on catalysis by Y200F OxDC mutant.	69

3-15	Effect of hemoglobin on catalytic inhibition by NO.....	70
3-16	Effect of hemoglobin on catalytic inhibition by NO after bubbling with N ₂	71
3-17	Overlaid CW-EPR spectra of the Mn (II) centers in OxDC in the presence and absence of NO released from MAHMA NONOate.....	72
4-1	Inhibition by azide ions of catalysis by OxDC.	80
4-2	Effects of dissolved halides on catalysis by OxDC.	81
4-3	Inhibition by nitrite ion of catalysis by OxDC.....	83
4-4	Inhibition by bicarbonate of catalysis by OxDC.....	85
4-5	Mode of inhibition by azide of catalysis by OxDC.....	87
A-1	12% SDS PAGE gel of fractions from the expression and purification of C-terminally His ₆ -tagged wild-type <i>BsOxDC</i>	97
A-2	12% SDS PAGE gel of fractions from the expression and purification of untagged wild-type <i>BsOxDC</i>	97
A-3	12% SDS PAGE gel of fractions from the expression and purification of untagged C383S <i>BsOxDC</i> mutant.....	98
B-1	Amino acid sequence alignment of several bacterial and fungal OxDC using ClustalW.	99
B-2	Amino acid sequence alignment of bacterial and fungal OxDC with the bicupin oxalate oxidase (OxOx) from yeast.....	100
B-3	Amino acid and <i>yvrk</i> gene sequences of oxalate decarboxylase from <i>B. subtilis</i>	101

LIST OF ABBREVIATIONS

AC	alternating current
DC	direct current
DEA NONOate	diethylammonium (Z)-(N,N-diethyl-amino)diazen-1-ium-1,2-diolate
FDH	formate dehydrogenase
HCO ₃ ⁻	bicarbonate anion
His6-tagged	protein bearing a polyhistidine affinity tag comprised of six histidine residues
MAHMA NONOate	(Z)-1-(N-methyl-N-[6-(N-methylammoniohexyl)amino]diazen-1-ium-1,2-diolate
MIMS	membrane inlet mass spectrometry
MnSOD	manganese superoxide dismutase
N ₃ ⁻	azide anion
NAD ⁺	nicotinamide adenine dinucleotide
Ni-NTA	nickel-nitrilotriacetic acid
NO	nitric oxide
NO ₂ ⁻	nitrite anion
NO ₃ ⁻	nitrate anion
O-PDA	ortho-phenylenediamine
OxDC	oxalate decarboxylase
SCN ⁻	thiocyanate anion
SDS PAGE	sodium dodecyl sulfate-polyacrylamide gel electrophoresis

Abstract of Dissertation Presented to the Graduate School
of the University of Florida in Partial Fulfillment of the
Requirements for the Degree of Doctor of Philosophy

KINETIC CHARACTERIZATION OF CATALYSIS BY OXALATE DECARBOXYLASE
USING MEMBRANE INLET MASS SPECTROMETRY

By

Mario Edgar Gabua Moral

December 2011

Chair: Nigel G. J. Richards
Major: Chemistry

Oxalate Decarboxylase (OxDC) from *Bacillus subtilis* is a manganese (II)-containing enzyme which catalyzes the breakdown of monoprotonated oxalate to carbon dioxide and formate. A hallmark of the reaction is its reported dependence on oxygen, which is not consumed in the process. Nothing is known about how Mn(II) catalyzes the reaction, or how the oxygen cofactor even participates in catalysis. However, efforts on further studying the enzyme have been severely limited by the indirect and discontinuous nature of assays established to measure enzymatic activity.

My work reports on the application of Membrane Inlet Mass Spectrometry (MIMS) on catalysis by OxDC to develop a quick, direct and continuous assay through the measurement of product CO₂. This real-time alternative has shown to deliver comparable measurements in OxDC kinetics, and additional ways to investigate catalysis which were difficult to achieve in previously established methods.

In my work, MIMS was also employed to assess the product inhibition of OxDC catalysis and determine the reversible inhibition of a structural analog of O₂ – nitric oxide (NO). Formate was weakly inhibitory ($K_i > 200$ mM) while high levels of carbon dioxide had no effect on catalysis. Inhibition by NO was found to be uncompetitive with

a micromolar K_i value comparable to the reported binding constant of O_2 on this enzyme. Continuous wave Electron Paramagnetic Resonance (cw-EPR) measurements of the enzyme in the presence of NO showed no binding interaction between NO and catalytic manganese of OxDC. This may either suggest a binding interaction of NO with the other Mn(II) center, or an undiscovered binding pocket for NO (or O_2) elsewhere on the enzyme.

A systematic study on the catalytic effect of small anions has shown nitrite, azide, thiocyanate, and bicarbonate to be inhibitory. Inhibition constants for these anions were in the low millimolar range, with interestingly different modes of inhibition on the enzyme. Nitrite was uncompetitive; azide and thiocyanate were noncompetitive, and bicarbonate was competitive. These results show the complexity of OxDC catalysis and areas for further study in elucidating the catalytic mechanism of the enzyme. Other aspects of OxDC explored by this new assay are also described.

CHAPTER 1 BACKGROUND

***Bacillus subtilis* Oxalate Decarboxylase (BsOxDC) Structure and Reaction**

Oxalate decarboxylases are one of three classes of oxalate degrading enzymes, which are found in fungi and bacteria. The other two classes are either found mostly in plants (oxalate oxidases), or bacteria (Oxalyl-CoA decarboxylases).

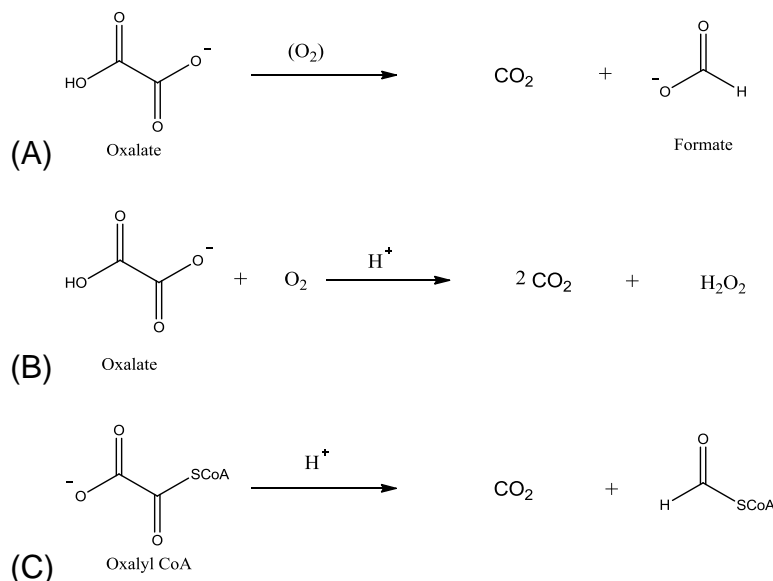
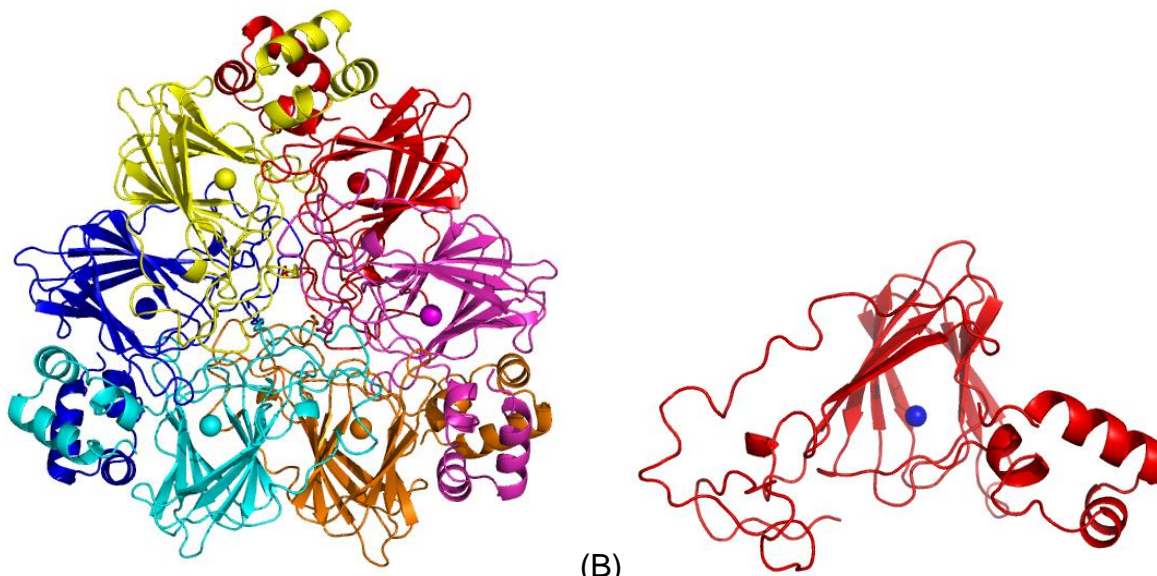


Figure 1-1. Reactions catalyzed by the three classes of oxalate-degrading enzymes. Oxalate degraded by (A) oxalate decarboxylases are found mostly in fungi and bacteria, (B) oxalate oxidases are found mostly in plants, while (C) Oxalyl CoA decarboxylase are found in bacteria.

Oxalate decarboxylases catalyze the breakdown of monoprotonated oxalate to formate and carbon dioxide Figure 1-1A (1-5). Catalysis is believed to be aerobic, though the required oxygen is not consumed in the reaction (1-4). This non-oxidative reaction feature of oxalate decarboxylase contrasts from that of a closely related class of enzyme – oxalate oxidase, which shares the same oxalate substrate and requirement for dioxygen for catalysis, but in contrast, oxidatively breaks down monoprotonated oxalate into an additional molecule of carbon dioxide and hydrogen peroxide (Figure 1-1B) (5, 6) The striking similarity between the structures of oxalate decarboxylase and

oxidase (Figures 1-2 and 1-3) has strongly suggested an evolutionary relationship between the two enzymes. This idea was supported by the fact that the oxalate decarboxylase from soil bacterium *B. subtilis* was observed to have a small (0.2-0.4%) inherent oxidase activity amidst its more predominant decarboxylase activity (7).



(A) (B)
Figure 1-2. Ribbon structure of germin oxalate oxidase from *Hordeum vulgare*.⁽⁸⁾ Colored spheres are respective Mn(II) atoms in the (A) homohexamer comprised of a trimer of dimeric units. (B) monomeric unit is a single domain defined by a β -barrel fold containing a Mn(II) atom. PDB: 1FI2. Structures were generated using PyMol v0.99 DeLano Scientific (San Francisco, CA).

B. subtilis oxalate decarboxylase crystallizes as a hexamer composed of a dimer of trimeric units (Figure 1-3 a-b). Each monomeric unit is characterized to have two Mn(II) atoms, each held in place by coordination with the sidechains of a conserved set of one glutamate and three histidine residues (5, 9, 10). Each of these manganese centers is enveloped in a β -barrel motif, referred to as a cupin fold (5, 11-13) giving rise to an N- and C-terminal manganese site in every bicupin monomer. Various work in literature involving site-directed mutagenesis and electron paramagnetic resonance (EPR) have suggested the N-terminal Mn(II) site to be the solvent accessible and main catalytic site in the enzyme (14-18).

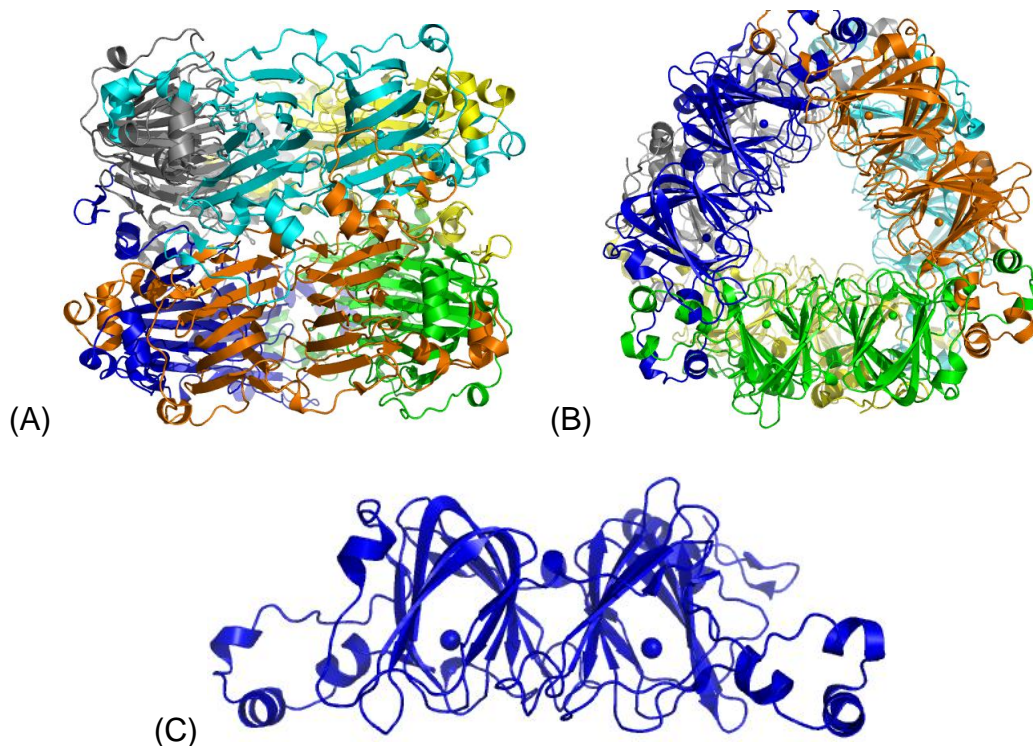


Figure 1-3. Ribbon structure of *B. subtilis* oxalate decarboxylase hexamer, trimer, and monomeric unit. (A) Side-view of the BsOxDC hexamer revealing a dimer of trimeric units (B) stacked in a back-to-back fashion. (C) Monomeric unit comprised of a symmetric set of two β -barrel folds, which define two domains within each holds a Mn(II) atom. PDB: IJ58. Structures were generated using PyMol v0.99 DeLano Scientific (San Francisco, CA).

The structural similarities shared between the active sites of oxalate decarboxylases and its close relative - oxalate oxidases, have not only implied the evolutionary relationship between them (11, 19, 20); but also facilitated the discovery of a five-residue N-terminal “active site lid” in *B. subtilis* oxalate decarboxylases(14). On this “lid” was found a vital protonating glutamate residue – Glu162 (Figure 1-4), which did not exist in the structurally similar oxalate oxidase(12, 14, 21).

<i>B. subtilis</i> OxDC	160	F SEN STF
<i>B. amyloliquofasciens</i> OxDC	166	F SEN STF
<i>A. niger</i> OxDC	228	F SE EESTF
<i>C. subvermispora</i> OxOx	240	F DAS NQF
<i>H. vulgare</i> OxOx	54	-EAGDDF

Figure 1-4. Partial sequence alignment of bacterial and fungal OxDC with yeast and plant OxOx showing the conserved glutamate (blue) on a presumed lid sequence (red) in OxDC (14), which is absent in OxOx.

Models on the mobility of this five-residue lid suggested a set of “open” and “closed” conformational changes in this loop, which were believed to regulate solvent access to the active site, and the proper positioning of the conserved glutamate lid-residue for its role in catalysis (10) (Figure 1-5). Literature suggests that catalysis in oxalate decarboxylase takes place when this N-terminal active site lid is “closed”, further suggesting that substrate access to the active site and product release occur only in the “open” conformation (9, 10, 14, 15).

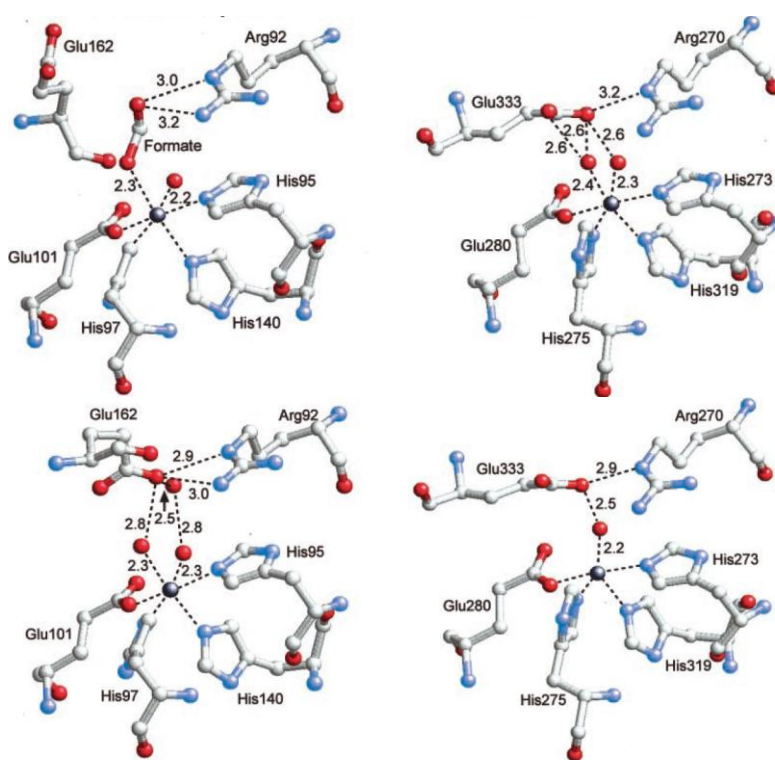


Figure 1-5. Mn(II) centers of the *B subtilis* OxDC monomer and the conserved set of one glutamate and three histidine ligand-binding residues. Research was originally published in (10) © American Society for Biochemistry and Molecular Biology. (Top left) N-terminal site in the “open lid” conformation showing the octahedral coordinated Mn(II), catalytic Glu-162 and what was interpreted to be formate from the electron density uniquely observed in this Mn(II) center. Independent red spheres are water molecules. (Top right) C-terminal Mn (II) with a symmetric set of residues around the similarly coordinated metal. PDB: IL3J. (Bottom left) N-terminal site in the “closed lid” conformation, where Glu-162 is now in closer proximity to serve as a proton-donor/acceptor to presumed oxalate bound to Mn(II) at one of the two available slots occupied in the model by water molecules (red spheres).

The mechanism of catalysis in this enzyme is not yet fully elucidated, but density functional theory (DFT) calculations and experiments employing kinetic isotope effects have led to the currently proposed mechanism of the catalyzed decarboxylation, which suggests a proton-coupled electron transfer (PCET) (5, 22, 23). In this mechanism, the dioxygen cofactor binds to manganese, which becomes the electron transfer hub between dioxygen and the bound substrate. The Mn-bound monoprotinated oxalate substrate is polarized by the interaction of one of its C=O bonds with a conserved arginine (21). This polarization facilitates the substrate's deprotonation by the proximal basic residue glutamate-162, which results in the heterolytic C-C cleavage (5, 18, 23) and departure of CO₂. This cleavage results in a Mn-bound formate radical. This bound formate radical intermediate is believed to be reprotontated by the same glutamate-162 residue (5, 21, 23), presumably in the "closed" position of the active site lid, where the Glu-162 is positioned closest to the hypothesized radical intermediate in the interior of the manganese active site (10, 15).

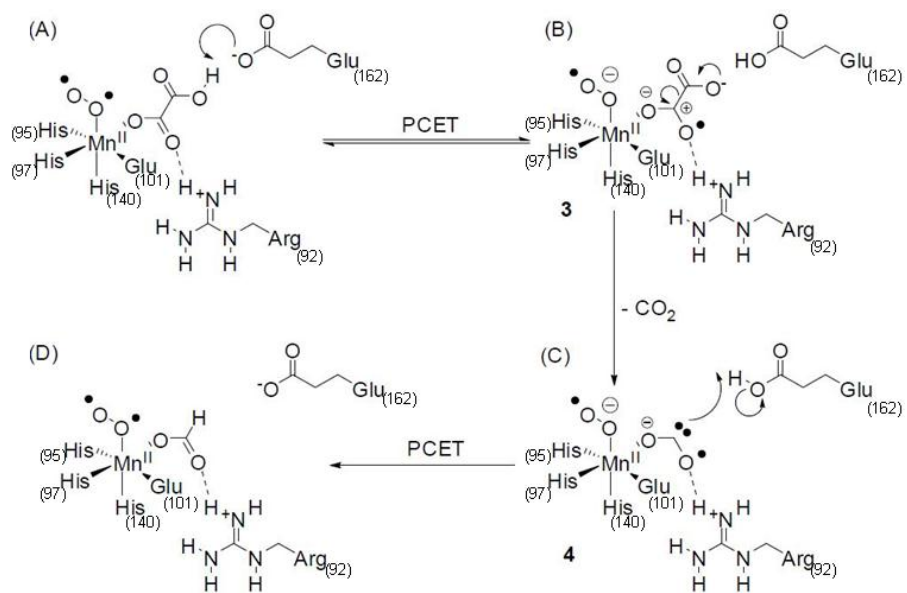


Figure 1-6. Proposed mechanism of the *B. subtilis* OxDC catalyzed decarboxylation of oxalate(23).

This hypothesis on glutamate-162 is consistent with site-directed mutagenesis work done on this residue and on other lid residues, where the replacement of Glu-162 abolished decarboxylase activity in the enzyme. Furthermore, three additional amino acid substitutions on the lid resulted in a “switch” in the chemistry of the enzyme towards promoting oxidase activity. This remarkable result supplemented the proposed catalytic mechanism in the enzyme, implicating Glu-162 to be the vital residue controlling the fate of the radical intermediate (24) in oxalate decarboxylase (Figure 1-6), towards being protonated and released in the form of formate, rather than oxidized into hydrogen peroxide and CO₂ (oxidase path) (14, 21, 23). The fact that four additional amino acid substitutions on the lid other than Glu-162 were required to promote the specificity switch from decarboxylase to oxidase further indicates that overall protein environment in the active site also has a vital role in influencing the chemistry of an enzyme’s catalysis (14).

Other site-directed mutagenesis work had established the dependence of decarboxylase activity on the amount of manganese incorporated in the enzyme. These studies not only supported earlier claims on the requirement of manganese in expressing the enzyme, but also suggested the possibility of the C-terminal manganese site contributing to the catalytic properties of the assumed main active site in the N-terminal domain (18).

Despite considerable progress in literature, other structural features of the enzyme, such as those responsible for accommodating the required dioxygen in the catalytic reaction, remain unknown. Continued efforts in studying this enzyme are largely guided by a close monitoring of enzymatic activity, which is often correlated with

controlled modifications on site-specific enzyme residues, or on catalytic reaction conditions.

Decarboxylase Activity Assays

Formate Dehydrogenase (FDH)-Coupled Assay

Decarboxylase activity has most often been measured by a traditional endpoint assay, which involves two main reactions: (I) the formate-generating OxDC catalytic reaction (Figure 1-1A), and (II) a coupling reaction which degrades formate with the concomitant reduction of nicotinamide adenosine dinucleotide (NAD⁺) to NADH (Figure 1-7) (21, 25, 26). The first reaction is usually conducted in a semi-micro vessel (e.g. eppendorf tube) containing enzyme-stabilizing components which are buffered with sodium acetate at catalytic optimum pH of 4.2 and 25°C. Catalysis is initiated by the addition of enzyme or substrate and then quenched after a predetermined amount of time by the addition of at least 100 mM sodium hydroxide base. Addition of the strong base raises the solution pH, resulting in the complete deprotonation of unreacted oxalate substrate in solution. Although unprotonated oxalate is no longer viable for further catalysis, the OxDC enzyme in solution remains active at this elevated pH.

Amount of catalytic formate formed in the abovementioned reaction is quantified in a separate “coupling reaction” where an aliquot of the earlier quenched reaction mixture is incubated overnight in a solution of nicotinamide adenosine dinucleotide (NAD⁺) and formate dehydrogenase, buffered at pH 7.6 with potassium phosphate. The quantity of reduced NAD⁺ (NADH) from the breakdown of formate is measured spectrophotometrically at 340 nM (21, 25, 26) and calibrated against absorbances of similarly treated solutions containing known amounts of pre-formed formate.

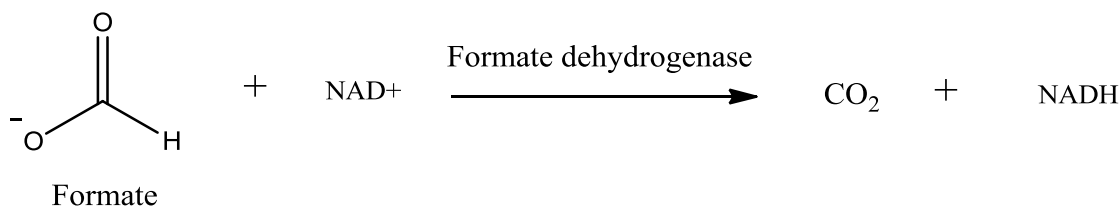


Figure 1-7. Coupling reaction of the FDH Assay for oxalate decarboxylases. Formate is converted to carbon dioxide with a concomitant reduction of adenosine nicotinamide dinucleotide to a form in solution which is detected by its measured absorbance at 340 nm.

Fourier Transform Infrared (FTIR) Spectrophotometric Assay

The first real-time monitoring of decarboxylase activity reported involved the use of fourier transform infrared spectrophotometry (27). This method took advantage of the infrared absorption of substrate and products, which were admittedly rare properties “exploited” for enzyme kinetics. Nonetheless the unique approach had the ability to simultaneously monitor the consumption of oxalate and the formation of carbon dioxide, carbonate, and formate. The method is based on time-dependent changes in absorbances associated with the C-O bond vibrations of substrate and product throughout a single catalytic reaction. These different C-O bond bend/stretch absorb at distinct regions on the 1000-4000 cm^{-1} scanning range, which is sampled in 25 millisecond intervals over a period of 5 minutes.

Ability of this method to monitor both oxalate and product formate has enabled this approach to also monitor oxidase activity in OxDC and mutant enzyme constructs. Since decarboxylase activity is indicated by the loss of oxalate (1308 cm^{-1}) concomitant to the emergence of formate (1385 and 1352 cm^{-1}), any loss of oxalate which is not accompanied by the emergence of peaks associated with formate product would indicate the alternative route in catalysis most coherent with oxidase activity. The method has also been employed in investigating solvent interactions with catalysis and

the fate of substrate atoms by the use of isotope-labeled reagents. These were accomplished by monitoring expected shifts in FTIR absorbances associated with modified bond stretches from heavier isotopes incorporated in catalytic products.

Limitations of Current Decarboxylase Activity Assays

Under optimum conditions, specific activity and kinetic measurements on wild-type OxDC may conveniently be accomplished using the FDH-coupled endpoint assay. The same can be said for mutant constructs with “near” wild-type behavior. This is because timecourses (0.5 – 1 minute) for the first catalytic reaction have previously been optimized to reliably sample the initial rates of product formation prior to the FDH coupled reaction step when these are quantified. The inability to acquire catalytic progress curves from a single experiment presents a problem, especially when reaction conditions change the timeframe when initial rates of the enzyme (or mutant) are best measured. Separate timecourse experiments may be designed to survey the best timeframe to run the first catalytic reaction, but this preliminary step entails a long turnaround time and numerous sample preparations. Furthermore, any experimental conditions which affect the FDH coupling reaction instantly renders this assay useless in studying OxDC.

Real-time monitoring of catalysis by FTIR spectrophotometry not only provides the first continuous assay for OxDC, but also the versatility of monitoring decarboxylase and oxidase activity. However, data processing involves the deconvolution of accumulated spectra which can both be tedious and time consuming. Ability to do experiments involving isotope-labeled compounds is a great advantage in this method. However, shifts in absorbances may not always be simple to track down, especially for reaction

conditions involving substances which may also have absorbances in the same region of detection.

In both assays, detection limits are an issue. Reported UV absorbances for example, are only reliable when they are at a magnitude within the instrument's linear region of detection. This often translates to the need for experimental conditions where considerable amounts of product have to be generated. These conditions are difficult to attain when working with weakly active mutant enzyme constructs, or when studying inhibitors.

Membrane Inlet Mass Spectrometry (MIMS)

Biochemical applications of mass spectrometry have been emerging in fields of proteomics, metabolomics, and medical research. Interfaced analytical devices such as high performance liquid chromatographs (HPLC), as inlets to a mass spectrometer (28), have provided the ability to isolate and quantify components of mixtures while subsequently identifying them through precise mass measurements (29, 30).

A much simpler inlet utilizing a semipermeable membrane to select species from a solution or suspension to enter a mass spectrometer was first demonstrated by Hoch and Kok (31). The usefulness of the method in measuring gases in physiological studies of algae and plants had set the precedent for diversified applications of membrane inlets in many studies employing mass spectrometry. Biological applications of membrane inlet mass spectrometry (MIMS) is well described in the measurement of CO₂ in physiological samples (32, 33), volatile organic compounds (34), and in understanding enzymatic mechanisms (35). Membrane inlets in these studies were made of materials which were permeable to non-polar and low molecular weight molecules. Because these membrane inlets can be immersed in a solution for direct measurement of

dissolved gases in solution, they are feasible for use in gas-evolving enzymatic reaction mixtures. Though MIMS has been employed in the study of certain enzymes, it has not been applied to the study of production of CO₂ in catalysis by the decarboxylases.

Research Objectives

Measurement of catalytic activity is vital to the study of any enzyme. Current assays for oxalate decarboxylase activity may provide dependable routine kinetic measurements for protein preparations, but they lack the versatility to further experiments in studying OxDC. A quick, yet sensitive continuous assay which can support a broader range of reaction conditions may provide more information to validate long standing hypotheses on the OxDC enzyme, its mechanism, and its potential applications.

The main objectives of the presented research were: 1) to develop an alternatively quick, direct, and continuous assay employing MIMS on catalysis by OxDC; 2) to utilize MIMS to further investigate the OxDC catalytic reaction; and, 3) to survey and characterize inhibitors of OxDC by MIMS to gather more information for future experiments exploring medical applications of the enzyme and its catalytic forms in its reaction mechanism.

CHAPTER 2 CHARACTERIZATION OF OXDC BY MEMBRANE INLET MASS SPECTROMETRY

Introduction

MIMS uses diffusion across a membrane as an inlet to a mass spectrometer (Figure 2-1). Because the method is based on the permeability of the membrane inlet to dissolved gases while being mostly impermeable to water and charged solutes, catalytic generation of carbon dioxide in solution by OxDC can provide a good basis for measuring decarboxylase activity through MIMS.

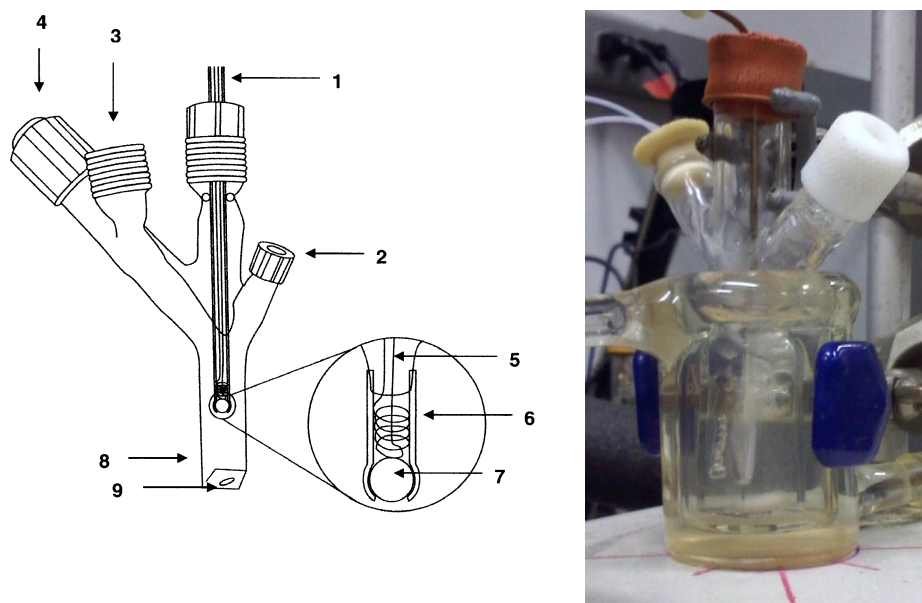


Figure 2-1. The membrane inlet inserted in an air-tight cell for mass spectrometric measurements: 1) tubing leads to mass spectrometer; 2) sample introduction port with septum; 3) threaded glass port for connecting to vacuum or for introduction of inert gas; 4) vacuum needle valve stopcock; 5) wire helix for support of the Silastic tubing; 6) Silastic tubing of length 1 cm (1.5 mm i.d. and 2.0 mm o.d.); 7) glass bead to seal the Silastic tubing; 8) glass optical cuvette; 9) magnetic stirring bar(35). Reprinted from (36) with permission.

Reaction Vessel

Reaction mixtures (2-mLs) are placed in a fabricated quartz cuvette which is jacketed in a circulating water bath, whose temperature may be regulated for desired constant temperature conditions. The vessel contains a magnetic stirring bar which

constantly stirs the reaction mixture on a supporting magnetic stirplate. The reaction chamber has a minimum of three gas-tight inlets/caps: one for the membrane inlet probe (interfaced to the mass spec); one for the (air/helium) gas inlet and outlet for equilibrating reaction mixtures, and one for the addition of sample or buffer components.

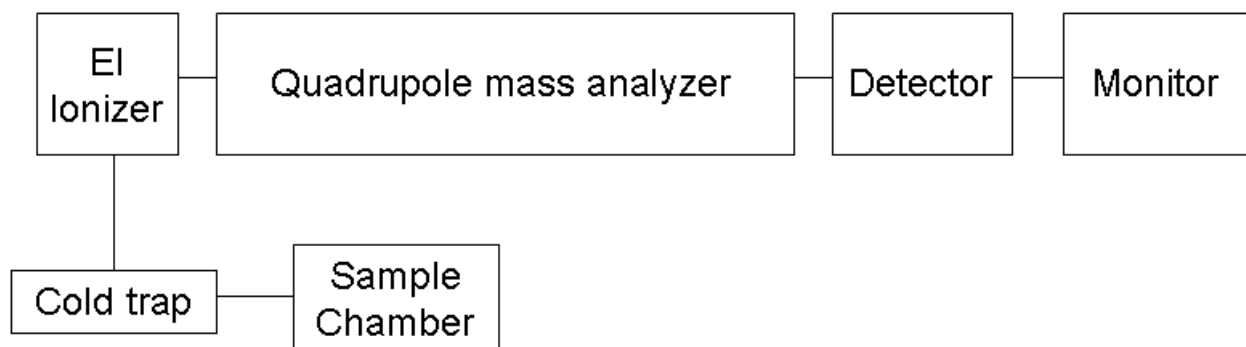
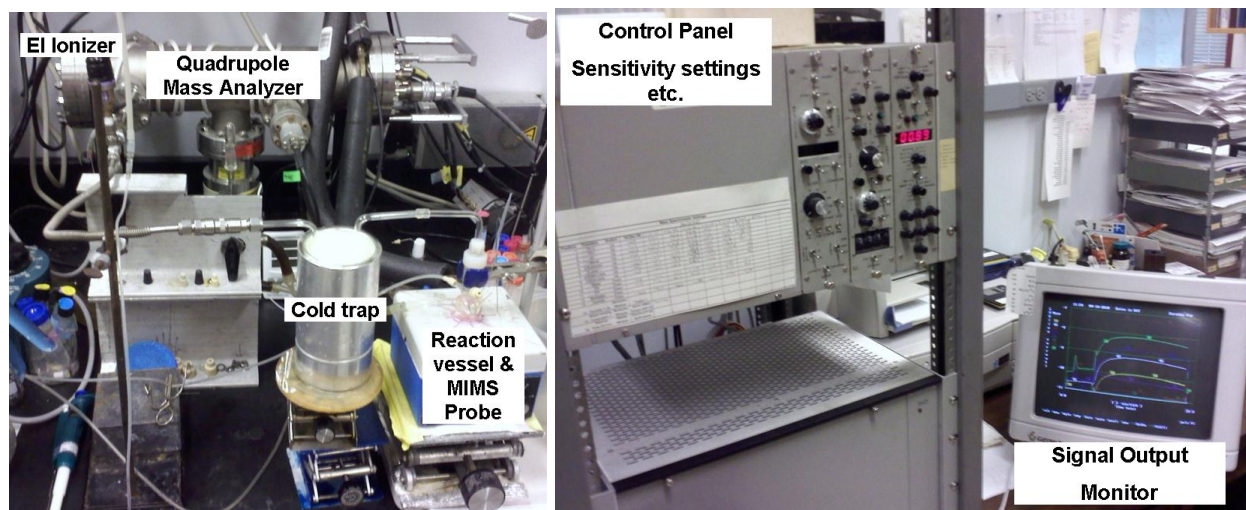


Figure 2-2. Picture of the modified MIMS instrument. (Bottom) Block diagram illustrating the main components and schematic of the system.

Membrane Inlet Probe and (Electron Impact) Ionization

The reaction chamber is interfaced with the instrument through a membrane inlet probe immersed in the reaction solution. The tip of the immersed membrane inlet probe is equipped with a piece of inert silicone tubing (Dow Corning), which is permeable to small uncharged/hydrophobic species. The open end of the tube is plugged with a glass bead and the length of the tubing is supported by an inner coil, which serves as an inner

scaffold preventing the flexible tubing from collapsing under partial vacuum on the tip of the probe. The resulting cavity within the cylindrical tubing allows membrane-selected species into the probe and into the ionization chamber of the instrument. The path between the membrane and the instrument is routed through a cold trap of dry ice and acetone. This cold trap freezes out any water vapor in the lines, preventing water molecules from entering the mass spec instrument. Since detection of species are dependent on the successful flight of molecules through the instrument, rationalizing the need to maintain the lines under a certain vacuum, unwanted water molecules in the instrument may interfere in the flight path of the species and thus adversely affect overall signal detection.

Gaseous molecules passing through the inlet travel to the ionizer where a beam of electrons collide with the influx of sample molecules. Electrons in the beam collide with these entering molecules, resulting in their ionization by “knocking off” an electron from each molecule. This process results in a population of positive ionic species which proceed into the linear quadrupole, where they are differentiated by their relative masses.

Mass Analyzer

The mass analyzer in this instrument is a single quadrupole comprised of four rod electrodes in a square configuration (28) with a small central gap serving as the inner “tunnel” through which the population of ions travel. Each rod electrode has an alternating polarity assignment resulting from a potential composed of a DC and AC component (28). Since the ionized specie would be attracted to a rod of opposite charge, it is conceivable that the ion will crash against one of the four rods it is attracted to. However, the polarity assignments of each rod periodically toggle at a certain

frequency, allowing the successful passage of the ion through the central cavity of the quadrupole in a “twirled” path. The quadrupole frequency at which an ion successfully travels through the mass analyzer is directly associated with its ionic mass, which is programmed into the instrument’s detector. Thus, the quadrupole varies the frequency at which it toggles the polarity assignments, resulting in a frequency sweep that continuously scans for ionic species from larger masses to lower masses throughout the experiment.

Ionic species which successfully travel through the quadrupole are detected upon their contact to a detector plate which results in an ion current that is recorded by the instrument. These mass-differentiated populations of detected ions are recorded and traditionally reported as peaks on a computer monitor. This instrument has an additional software which periodically samples a point from a defined vertical coordinate at each selected m/z peak and simultaneously plots these points on a time course. These time course plots result in progress curves (for each selected signal) describing the reaction profile occurring in the vessel throughout a catalytic experiment. Figure 2-3 illustrates the real-time representation of a single m/z signal on a time course plot.

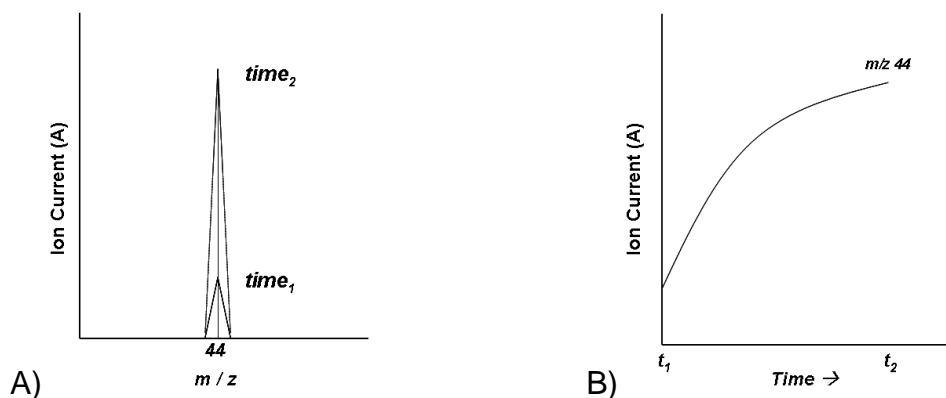


Figure 2-3. Cartoon showing how the (A) time-dependent growth in peak height of a selected signal is reillustrated as a (B) progress curve on the monitor of the MIMS instrument.

In demonstrating the application of MIMS to kinetic studies of decarboxylases, decarboxylation of ^{12}C - and $^{13}\text{C}_2$ -labeled oxalate was measured to yield $^{12}\text{CO}_2$, $^{13}\text{CO}_2$ and formate catalyzed by OxDC from *B. subtilis*. Dissolved gases were detected by immersing the membrane inlet into the air-equilibrated reaction solution and monitoring different masses using the ion current at peak heights. Reactions were carried out in an air-tight vessel such as shown in Figure 2-1. The immersed membrane inlet, which was permeable only to small uncharged species, was interfaced to a mass spectrometer through a cold trap of dry ice and acetone.

Gaseous molecules entering the probe were ionized in the mass spectrometer by electron impact (EI), and analyzed through a standard linear quadrupole (Figure 2-2). Detected ions were recorded by their mass-to-charge (m/z) ion currents, which numerically corresponded to their respective molecular weights. Time-dependent changes in m/z peak heights were plotted onscreen in real-time, giving rise to progress curves illustrating the profile of the reaction taking place in the vessel.

Results and Discussion

Real-time Monitoring of catalysis

In order to start every experiment with a set of stable baseline signals for each detected gas, the buffered pre-reaction mixture was bubbled for at least 3 minutes either with air (for air-equilibrated experiments) or helium (for deoxygenated or oxygen-depleted reaction conditions). Upon achievement of “pre-reaction” equilibrium, as indicated by a stable flat line (~ 0 slope) for each gas signal on the monitor, data acquisition begins ($t = 0$) and the reaction is often initiated with the addition of enzyme after two minutes (Figure 2-4). Time at which reaction is initiated by the addition of enzyme may vary depending on the nature of the experiment, but a consistent starting

point is highly preferred in order to more conveniently overlay progress curves whenever necessary during data processing.

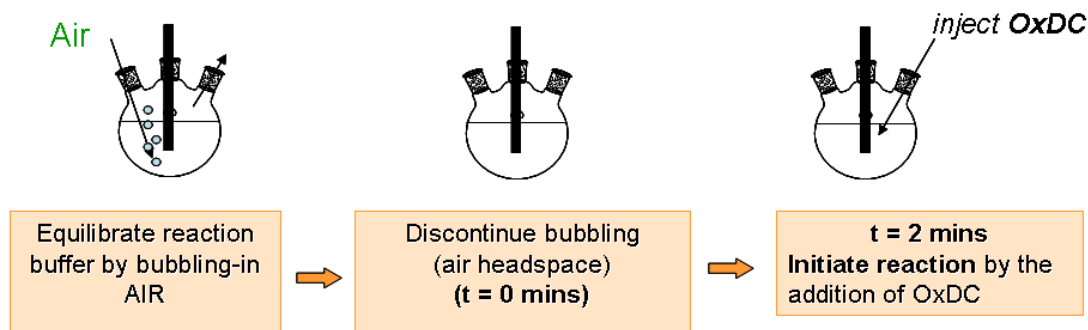


Figure 2-4. Experimental scheme for air-equilibrated catalytic experiments. Buffered pre-reaction mixtures containing oxalate substrate are pre-equilibrated by the bubbling in of CO₂-scrubbed air. Data acquisition (t = 0) begins when the air inlet is removed. Reaction is initiated upon addition of OxDC enzyme at 2 minutes.

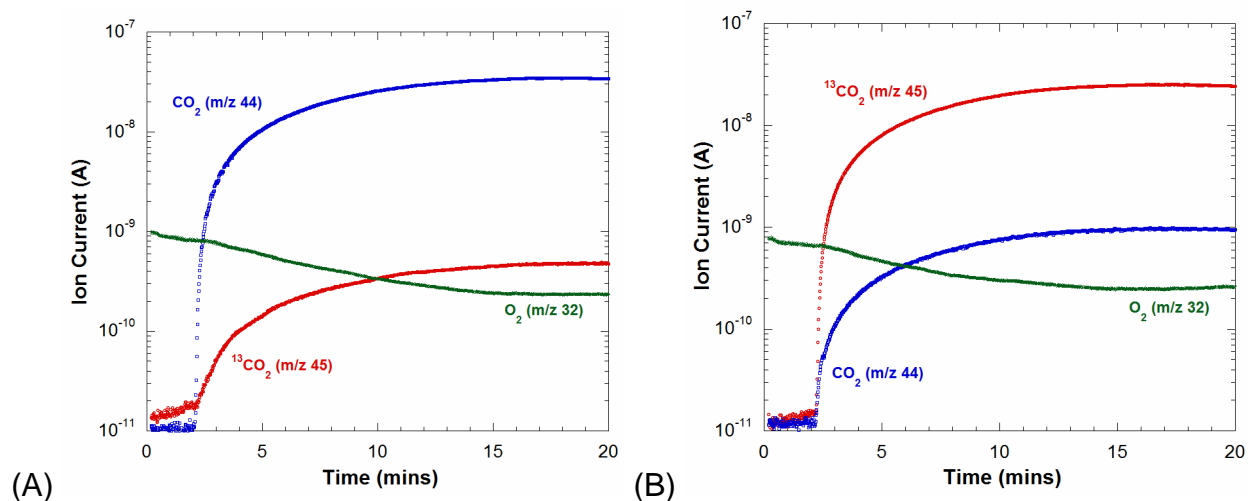


Figure 2-5. Ion currents (arbitrary scale) in the production of carbon dioxide from (A) ¹²C oxalate and (B) ¹³C₂-labeled oxalate catalyzed by OxDC in air equilibrated buffer. Dissolved gases were monitored from the ion currents at their respective peak heights: (red) ¹³CO₂ at m/z 45; (blue) CO₂ at m/z 44; and (green) O₂ at m/z 32. The solution contained 50 mM potassium ¹²C oxalate (A) and ¹³C₂-oxalate (B), 0.2% Triton X-100, 50 mM sodium acetate buffer at pH 4.2 and 25°C. Reaction was initiated at 2 minutes by the addition of (His₆-tagged) wild-type OxDC to a final concentration of 1.4 μM in a total reaction volume of 2 mL.

Examples of real-time monitoring of catalysis by MIMS are illustrated in Figure 2-5.

Here, OxDC catalysis was initiated by addition of enzyme at 2 minutes to solutions

containing 50 mM potassium oxalate substrate. Real-time data are reported onscreen from the instrument as relative ion currents on a logarithmic scale. Logarithmic plotting of detected currents allow for the simultaneous monitoring of small and large changes in the m/z signals in a single frame/screen. Optimization of sample/reaction conditions is largely dependent on aiming to have the monitored signals stay within the limits of the scale on the screen throughout the catalytic reaction. In Figure 2-5A, the progress curve for the accumulation of product CO_2 was observed through the rise of the m/z 44 peak (CO_2). A proportional rise in the m/z 45 peak ($^{13}\text{CO}_2$) was also observed reflecting the 1% relative natural abundance of ^{13}C to ^{12}C in the generation of CO_2 product in solution. Alternatively, catalytic product was observed through the rise in the m/z 45 peak ($^{13}\text{CO}_2$) when 50 mM of (99% enriched) $^{13}\text{C}_2$ -labeled oxalate was used in a separate experiment (Figure 2-5B) confirming the assumption that observed rise in CO_2 was indeed a catalytic product of OxDC from supplied oxalate substrate. Unlike the previous experiment using unlabeled oxalate, the ratio between m/z 45 and m/z 44 signals in (B) using 99% enriched $^{13}\text{C}_2$ -oxalate did not amount to 1 or 2%, but an elevated 4%. Although this difference is minimal, the consistently observed additional 3% in m/z 44 signal was later confirmed to be an artifact coming from a small fraction of $^{13}\text{CO}_2$ ions being detected by the instrument as $^{12}\text{CO}_2$. Because the scanning in the linear quadrupole allows for a sweep of detected ions from high to low m/z , the overlap of frequencies between two adjacent m/z signals result in a small fraction of the m/z 45 ions traveling through the quadrupole to be caught by the detector as part of the detected m/z 44 population of ions. This was confirmed when 99% ^{13}C -labeled potassium bicarbonate was injected in acidic buffer, which gave rise to the same 4%

relative intensity of m/z 44 (vs. m/z 45), instead of the expected 1%. Due to the nature of the frequency sweep (m/z sweep of detection) this phenomenon is limited to adjacent m/z signals and is “unidirectional” (ie. from higher m/z to lower m/z unit). This would explain why no artifact signal is observed on m/z 45 when unlabeled oxalate resulting in an abundance of catalytic m/z 44 signal is used in an experiment.

In both cases, an apparent consumption of dissolved oxygen was observed in catalysis from the decrease in the (green) m/z 32 signal. In order to confirm this, the experiment utilizing $^{13}\text{C}_2$ -labeled oxalate was observed with the simultaneous monitoring of an additional gas in solution. Dinitrogen, also shown in Figure 2-6, originated from the air equilibration of this sample and is not generated or consumed in the catalysis; hence, its peak at m/z 28 is a control for the stability of the method. A very slight decrease in the m/z 28 peak over the course of the experiment (Figure 2-6) is a measure of the rate of loss of N_2 from solution by passage across the membrane inlet into the mass spectrometer or into the headspace. This was negligible compared with changes in $^{13}\text{CO}_2$ levels.

A small component of total catalysis by OxDC is an oxidase that consumes oxygen and yields two molecules of CO_2 in each catalytic cycle (Figure 1-1B). Consumption of oxygen in Figure 2-6 is observed by the rate of decrease in the m/z 32 peak which is greater than the rate of decrease in the control peak for m/z 28. A further control was performed in a separate experiment in which dioxygen was introduced into the reaction buffer containing oxalate but in the absence of OxDC. The observed rate of signal decay for m/z 32 was negligible. From the data of Figure 2-6, and similar repeated experiments, the ratio between the calibrated rates of decrease in m/z 32

(apparent O₂ consumption) and the rate of increase in m/z 45 (catalytic ¹³CO₂) amounted to 0.3 – 0.5%. This led to the estimate that approximately 0.3% to 0.5% of the overall rate of catalytic degradation of oxalate is due to the oxidase pathway of catalysis by OxDC rather than the decarboxylase pathway, which is consistent with literature values (7, 37). Hence the MIMS method has the capability to measure the oxidase function of OxDC in the same experiment as the decarboxylase activity.

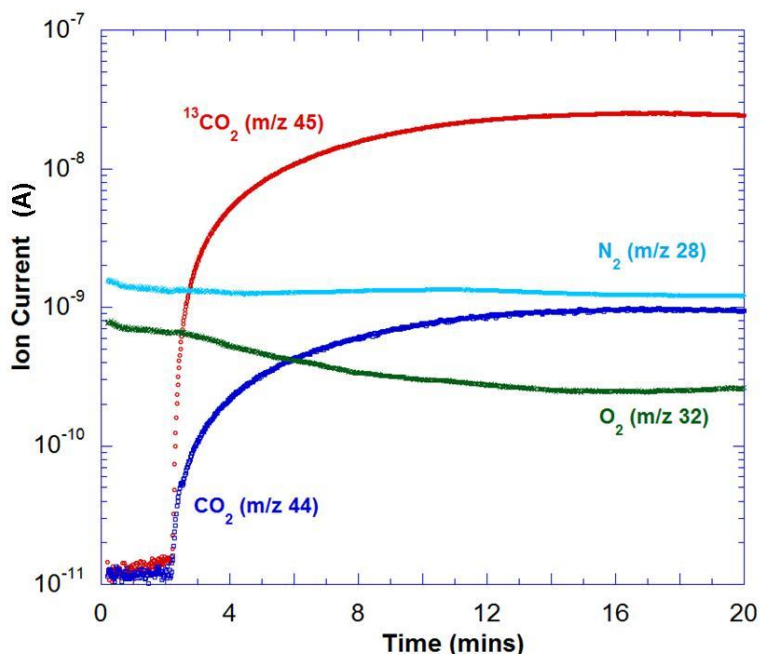


Figure 2-6. Ion current in the production of ¹³CO₂ from ¹³C₂-oxalate catalyzed by OxDC. Dissolved gases were monitored from the ion currents at their respective peak heights: (red) ¹³CO₂ at m/z 45; (green) O₂ at m/z 32; and (cyan) N₂ at m/z 28. The solution contained 50 mM potassium ¹³C₂-oxalate, 0.2% Triton X-100, 50 mM sodium acetate buffer at pH 4.2 and 25°C. Reaction was initiated at 2 minutes by the addition of (His₆-tagged) wild-type OxDC to a final concentration of 1.4 μM in a total reaction volume of 2 mL. Reprinted from (36) with permission by Elsevier.

Reproducibility

In order to assess the reproducibility of observed catalysis using MIMS, data from three separate experiments of identical conditions to those described in Figure 2-6 were compared (Figure 2-7). The experiments in red and blue were separated by 20 minutes.

The experiment in black was performed on a separate day. The standard deviation in the initial rates (5% product conversion) in these three measurements was 6%.

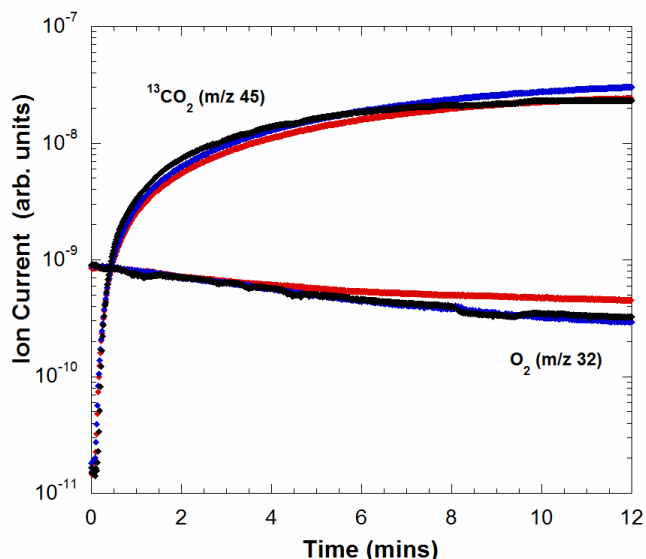


Figure 2-7. Superimposed ion currents (arbitrary scale) of three separate experiments involving the production of $^{13}\text{CO}_2$ from $^{13}\text{C}_2$ -oxalate catalyzed by OxDC. Dissolved gases were monitored from the ion currents at their respective peak heights for $^{13}\text{CO}_2$ at m/z 45 and O_2 at m/z 32. The solution contained 50 mM potassium $^{13}\text{C}_2$ -oxalate, 0.2% Triton X-100, 50 mM sodium acetate buffer at pH 4.2 and 25°C. Reactions were initiated at time 0 by the addition of (polyhistidine-tagged) wild-type OxDC to a final concentration of 1.4 μM in a total reaction volume of 2 mL. Reprinted from Supplementary Material of (36) with permission by Elsevier.

Response time

The response time of the apparatus was measured by rapid injection into the reaction vessel of a solution containing CO_2 and measuring the time to reach a plateau of ion current at m/z 44. The final concentration of CO_2 was approximately 2 mM and the time to reach plateau was adequately fit to a first-order process with a half-time of 4 seconds.

Buffer conditions: Air equilibrated vs. O_2 -depleted (He-bubbled)

Air equilibrated buffers were selected in this chapter to best parallel the experimental conditions of the traditional FDH-coupled endpoint assay. However, it was

observed that catalysis was not significantly different when buffers were considerably depleted of dissolved dioxygen. In these experiments buffers were alternatively bubbled in with helium gas minutes prior to catalysis as described in Figure 2-8.

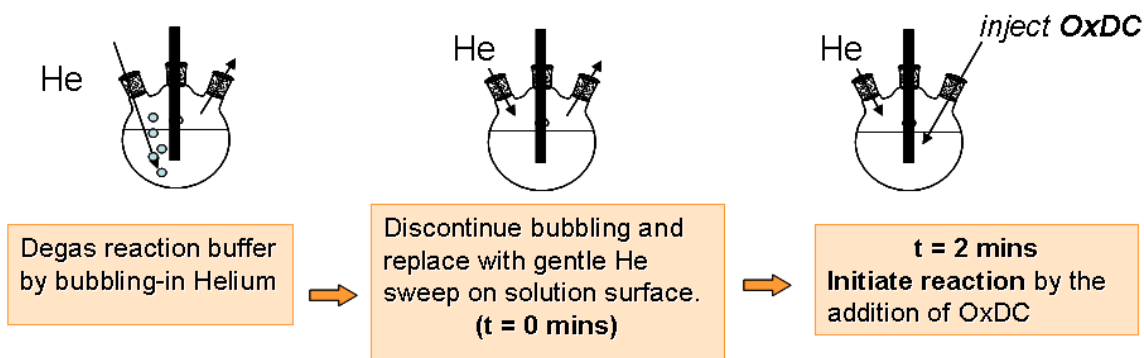


Figure 2-8. Experimental scheme for oxygen depleted catalytic experiments. Buffered pre-reaction mixtures containing oxalate substrate are pre-equilibrated by the bubbling in of helium gas. Data acquisition ($t = 0$) begins when helium inlet is removed. A gentle sweep of helium is placed on the solution surface to prevent air from the headspace to re-enter the solution. Reaction is initiated upon addition of air-equilibrated OxDC enzyme at 2 minutes.

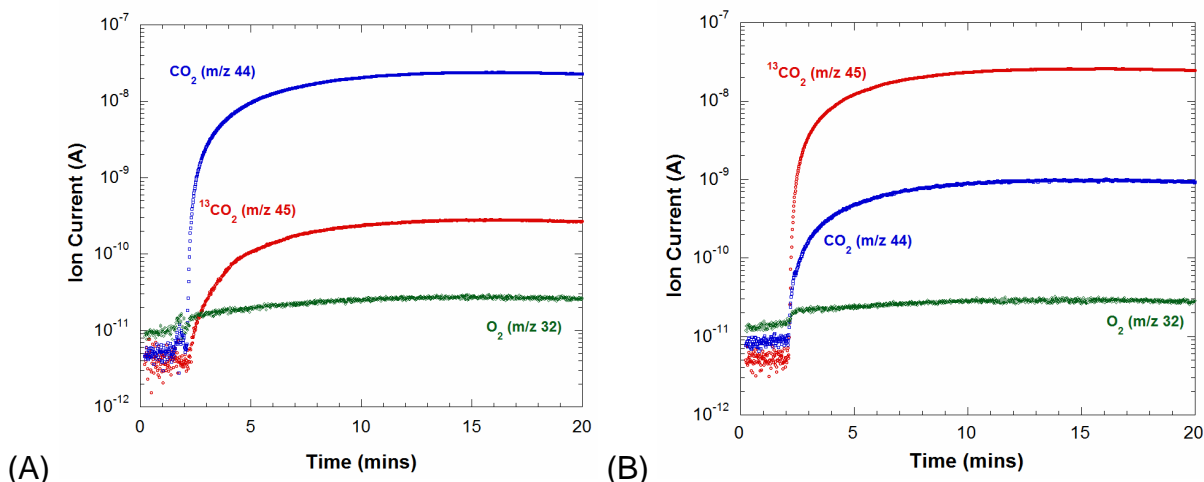


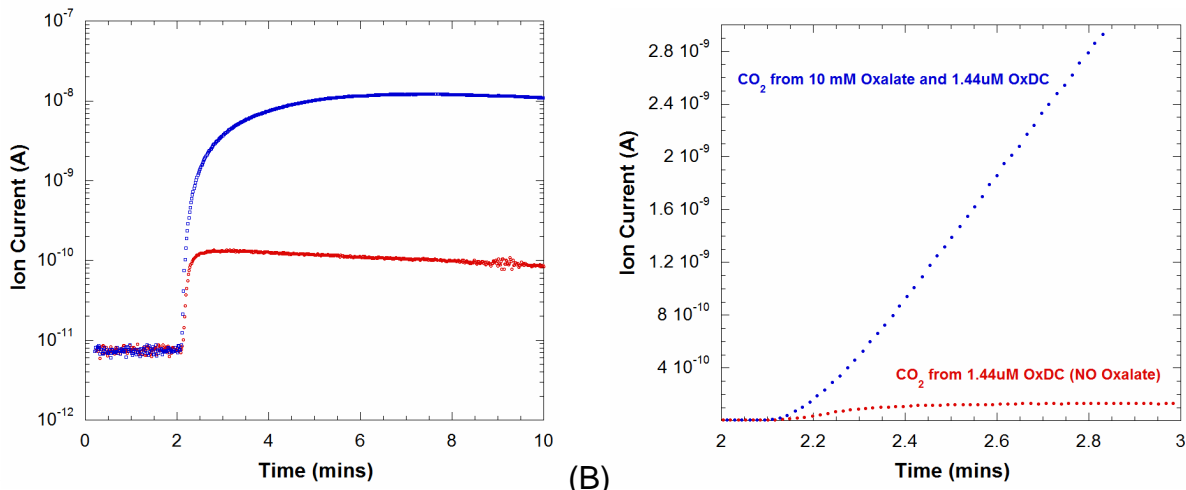
Figure 2-9. Ion currents in the production of carbon dioxide from (A) ^{12}C and (B) $^{13}\text{C}_2$ -labeled oxalate potassium oxalate catalyzed by OxDC in deoxygenated buffer. Dissolved gases were monitored from the ion currents at their respective peak heights: (*red*) $^{13}\text{CO}_2$ at m/z 45; and (*green*) O_2 at m/z 32. The solution contained 50 mM potassium ^{12}C oxalate (A) and $^{13}\text{C}_2$ -oxalate (B), 0.2% Triton X-100, 50 mM sodium acetate buffer at pH 4.2 and 25°C . Reaction was initiated at 2 minutes by the addition of (His_6 -tagged) wild-type OxDC to a final concentration of 1.4 μM in a total reaction volume of 2 mL.

Addition of 5 – 20 μL s of air-equilibrated enzyme stocks (0.6 – 2.5 μM delivered oxygen) still resulted in observed decarboxylase activity albeit without any drop in the m/z 32 signal earlier associated with oxygen-consuming oxidase activity. Thus, O_2 -depleted buffer conditions were subsequently used (in Chapters 3 and 4) especially in experiments involving agents that are easily oxidized; and catalytic measurements requiring selectivity for decarboxylase activity.

Background CO_2 and Isotope-labeled substrate ($^{13}\text{C}_2$ -oxalate)

Because catalysis is initiated by addition of air-equilibrated enzyme stocks, carryover of CO_2 from enzyme aliquots often result in a small non-catalytic rise in detected m/z 44. Magnitude of this non-catalytic signal is recorded from a separate control experiment in the absence of substrate, where the maximum ion current from this “background” CO_2 is noted together with the time the signal reaches its maximum (Figure 2-10). In most cases when considerable catalytic activity is observed, effects of this background CO_2 on observed initial rates are negligible (Figure 2-10B). Nonetheless, this background signal is either subtracted at the end of the experiment, or neglected by measuring initial rates from a time-coordinate when this artifact has completely passed through the detector.

In cases where low catalytic rates are anticipated, or measured in the presence of elevated amounts of dissolved CO_2 , the use of $^{13}\text{C}_2$ -isotope-labeled oxalate is often preferred. This allows the convenient detection of catalytic carbon dioxide by the alternative monitoring of increasing m/z 45 ($^{13}\text{CO}_2$), which can only be observed in solution by the presence of OxDC and unaffected by carried over CO_2 from the enzyme aliquot.



(A) (B)
 Figure 2-10. Overlay of m/z 44 ion currents illustrating background (red) CO₂ detected from the air-equilibrated OxDC enzyme aliquot in the absence of substrate. (Blue) is the ion current from the catalysis of 10 mM oxalate by the same amount of OxDC enzyme. (A) presents the overlay of m/z 44 ion currents on a logarithmic scale. (B) is the same data showing the first minute of detected m/z 44 ion currents on a linear scale to illustrate differences in magnitude.

o-Phenylenediamine (o-PDA)

Emiliani et al. documented the favorable effect of reducing substances such as o-phenylenediamine (o-PDA) on catalysis by OxDC from *A. niger* (37). O-PDA had been a constant component of the endpoint assay reaction mix, presumably contributing to the stability of the enzyme for adequate detection of its activity throughout the coupled assay protocol. For the MIMS approach, o-PDA was no longer included in the buffer mix for two reasons: i) no significant difference was observed in MIMS detected catalysis in the absence of it; and ii) unnecessary reactive buffer components may contribute to signal artifacts from non-enzymatic side reactions.

Calibration

In order to convert raw ion currents to millimolar (mM) or micromolar (μ M) concentrations of detected gases, the membrane inlet mass spectrometer was calibrated by rapid injection into the reaction vessel of solutions of known CO₂

concentration. The most accurate procedure was to prepare solutions of K_2CO_3 at pH 10.2 and inject known volumes into the reaction vessel containing a concentrated solution of acetic acid (pH \sim 2). At this pH, 99.9% of all carbonate species exist as CO_2 . The ion current at m/z 44 was recorded when it reached a maximum. A plot of ion current versus CO_2 concentration was linear (Figure 2-11). We did not test the upper or lower limits of detectability of CO_2 , since these were not pertinent to the measurement of catalytic activity of OxDC. The instrument was similarly calibrated for O_2 by recording the average ion currents at m/z 32 in solutions of different O_2 concentration prepared by dilution of air-saturated reaction buffer at 25°C ($[O_2]$ is 256 μ M) (38). The resulting plot of ion current versus O_2 concentration was linear. The baseline signal corresponding to 0 μ M O_2 was verified using degassed reaction buffer containing 1 mg glucose oxidase which was deoxygenated by the addition of 7 mM glucose (7, 39).

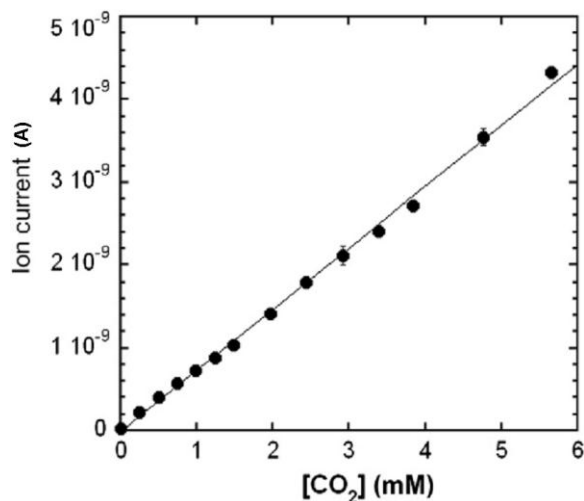


Figure 2-11. Ion current (arbitrary scale) at m/z 44 using the membrane inlet mass spectrometer observed using solutions of known CO_2 content. Solutions containing CO_2 were prepared from step additions resulting in 0.25-mM increments of K_2CO_3 into concentrated acetic acid (pH 2.0) and 25°C. Peak heights were recorded when equilibrium was reached. Shown are the averages of three repetitions with relative standard deviations of 3% at 4.8 mM CO_2 , 8% at 3.0 mM CO_2 , and 10% at 0.4 mM CO_2 . The solid line is a least-squares fit with a correlation coefficient of 0.999. Reprinted from (36) with permission.

Derived slopes from these linear-fitted calibration plots are used as factors to convert raw ion currents to millimolar or micromolar amounts of CO₂, or O₂. Whenever necessary, ion currents of other gases may similarly be calibrated. However, because different gases may interact and pass through the membrane differently, separate calibration experiments for those gases are required. Derived slopes are often good throughout a batch of experiments when the sensitivity (photomultiplier) settings and installed membrane remained unchanged. New calibration data is often required in situations when a new sensitivity setting is used, or when a new membrane (or any component of the instrument) is installed, as such would change the response of the instrument for the subsequent sets of experiments.

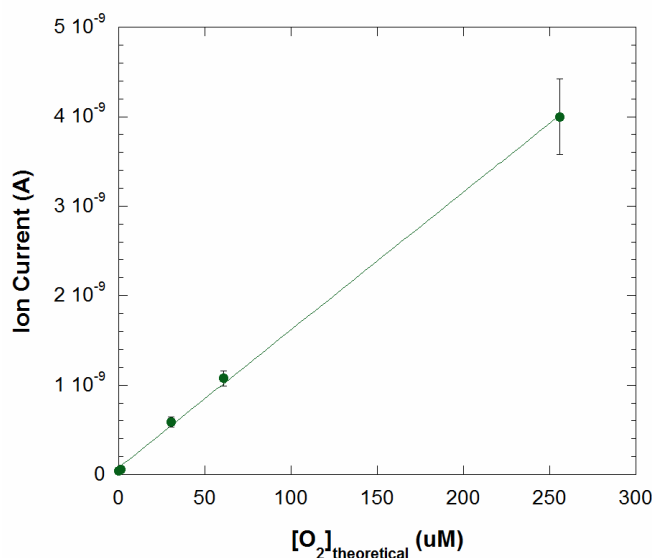


Figure 2-12. Ion current (arbitrary scale) at m/z 32 using the membrane inlet mass spectrometer observed using solutions of calculated O₂ content. Amounts of dissolved O₂ in solution were varied by diluting deoxygenated buffer with known volumes of air-equilibrated water to a final volume of 2 mL. Air equilibrated buffer at 25°C was assigned a concentration of 256 μM according to the solubility of O₂ in water at 25°C (38). Corresponding m/z 32 signal for 0 μM O₂ was taken from buffers deoxygenated by the prior bubbling-in of helium gas. Shown are the averages of duplicate runs with standard deviations of 10% at 256 μM O₂ and 8% at 61 μM O₂. The solid line is a least squares fit with a correlation coefficient of 0.999.

Data Analysis: Michaelis-Menten Kinetics

Steady state

Briggs and Haldane introduced the assumption of steady state as the point in enzymatic catalysis where reaction intermediates reach a constant level, resulting in a stable unchanged reaction rate as a function of time. The Michaelis-Menten equation expresses this concept through a hyperbolic function relating reaction rate (v) with substrate concentration $[S]$, where V_{\max} is the hypothetical maximum rate achieved, which is no longer affected by increasing substrate concentration. The turnover number k_{cat} is related to V_{\max} in Eqn 2-2 where $[E]$ is the total enzyme concentration. Michaelis constant (K_m) is an experimental term describing the concentration of substrate at half the maximum rate (V_{\max}) (40).

$$v = \frac{V_{\max} [S]}{K_m + [S]} \quad (2-1)$$

$$V_{\max} = k_{\text{cat}} [E] \quad (2-2)$$

The hyperbolic shape of this function is a result of two possible scenarios covered by this equation across various levels of substrate concentration $[S]$. At very low substrate concentrations where $[S] \ll K_m$, v can be described by Eqn 2-3. (40)

$$v = \frac{V_{\max} [S]}{K_m} \quad (2-3)$$

As substrate concentrations increase where $[S] \gg K_m$, the quantity K_m becomes negligible compared to $[S]$ and thus v alternatively becomes determined by V_{\max} , which ideally becomes unaffected by further increases in $[S]$. In these conditions the enzyme is said to be “saturated” where further catalysis becomes fully dependent on the ability for free enzyme to be regenerated or “turnover” (40).

$$v = \frac{V_{\max} [S]}{[S]} = V_{\max} \quad (2-4)$$

Because these two scenarios are distinguished by the experimental quantity K_m , catalytic rates (v) at varying substrate concentration $[S]$ are measured with the aim for deriving kinetic constants through the fitting of $[S]$ vs. v -plotted data to the Michaelis-Menten equation (Eqn 2-1).

In order to experimentally accomplish this, earlier assumptions are maintained in the experiment. Because steady state implies overwhelming amounts of substrate versus enzyme, enzyme concentrations are ideally at least three orders of magnitude less than total substrate concentration (40, 41). Under these conditions, when total enzyme concentration is occupied with bound substrate, the change in remaining $[S]$ is negligible. Furthermore, the highest attainable rate at any given substrate concentration would conceptually be at the early stage of catalysis when the putative enzyme substrate complex is formed and changes on $[S]$ is still negligible. This rate is often referred to as the “initial velocity” which often translates to ~5% - 10% product conversion (41), and is thus the main quantity of interest whenever a catalytic rate is reported.

Initial velocities

Initial velocities in catalytic experiments are often manifested through the early linear increase in the progress curve of product formation. These velocities are maximum rates achieved in those conditions before the progress curve plateaus either by significant depletion of available substrate to be converted or by reaching the limit of enzymatic turnover. Because the progress curves for CO_2 formation through MIMS are preceded by a lag-time due to the response time of the instrument, linear points

immediately after this lag time are sampled and fitted to a linear function whose slope is representative of the catalytic rate for a given substrate concentration (Figure 2-13).

Sources of error

Sources of experimental error in this method may include pipetting and the heterogeneity of stock solutions used throughout each set of measurements. These sources of error can be minimized by the use of the same pipets and stock solutions throughout each experiment and by having a standard way of mixing and delivering the buffer components with care into the reaction vessel.

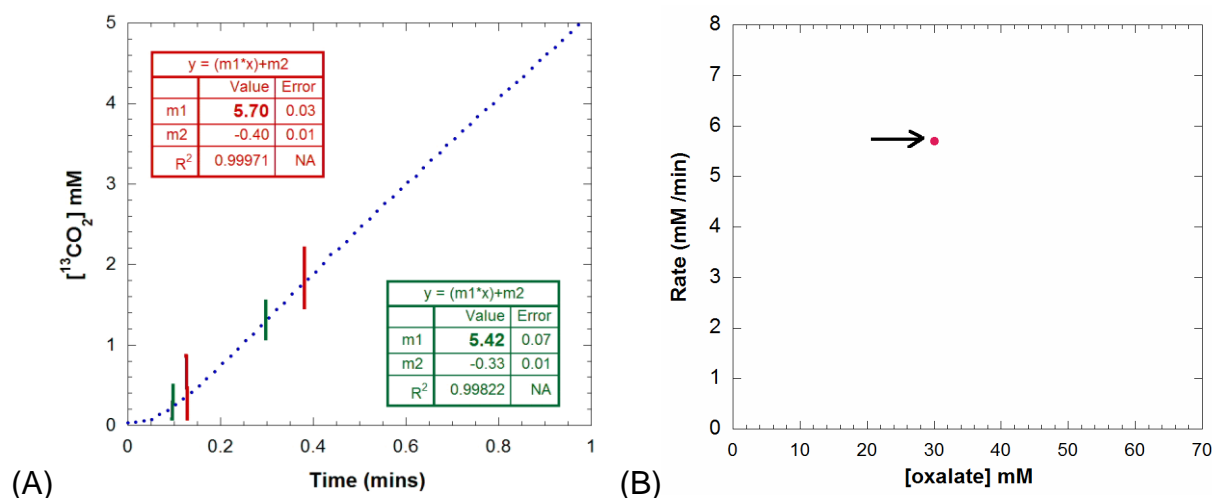


Figure 2-13. Example of deriving initial velocity from a progress curve of CO_2 formation. (A) Progress curve of calibrated ion currents showing $^{13}\text{CO}_2$ formation from the catalysis of 30 mM $^{13}\text{C}_2$ -labeled oxalate by 1.44 μM OxDC at pH 4.2. Inset are linear fits of two sets of sampled points bracketed in red and green for deriving the initial rate from the linear slope “m1”. Emboldened linear slopes “m1” show a 5% error in the derived initial rate, which is plotted on a separate plot (B) of reaction rate vs. oxalate concentration. Unless otherwise stated, each point represents a single measurement from the fitting of at least 10 data points in a single progress curve. Reported standard errors are from the variations of the slopes derived from the single progress curve.

Because of the reproducibility of observed ion currents, the major source of errors is associated with how the data is fitted and processed. These include the fitting of calibration points to derive a factor to convert ion currents to mM concentrations, and

further fitting to derive reaction velocities from sigmoidal progress curves (Figure 2-13), which may give rise to an error of 1% - 8% in the derived slopes (initial velocities). Hence, errors presented in the catalytic rates are errors inherent to deriving the reaction velocities from the progress curves. In the following sections on Michaelis Menten kinetics, single measurements of catalytic rates were made over more points of oxalate concentration to construct the Michaelis-Menten curve of this enzyme, instead of doing replicate runs over fewer substrate concentrations. Data are presented in the following sections.

Kinetic constants (MIMS vs FDH)

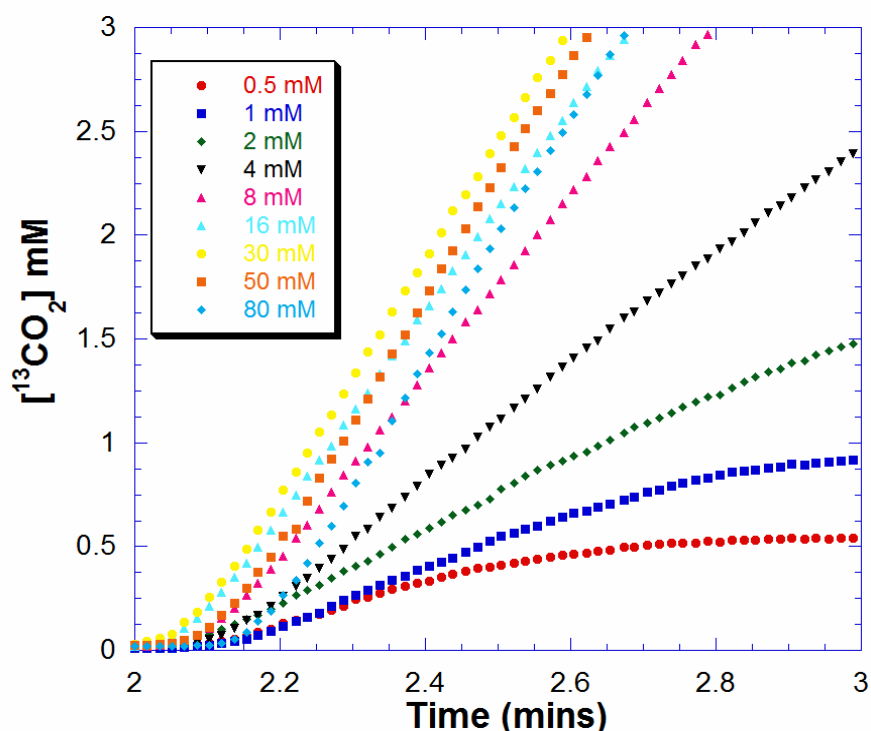


Figure 2-14. Accumulation of $^{13}\text{CO}_2$ in solution resulting from the catalysis by OxDC.. Initial concentrations of $^{13}\text{C}_2$ -labeled (99%) oxalate were as follows: red, 0.5 mM; dark blue, 1 mM; green, 2 mM; black, 4 mM; purple, 8 mM; cyan, 16 mM; yellow, 30 mM; orange, 50 mM; light blue, 80 mM. Each curve for different concentrations of oxalate represents a single experiment. Other components of the solutions were as described in Figure 2-5. Reprinted from (36) with permission by Elsevier.

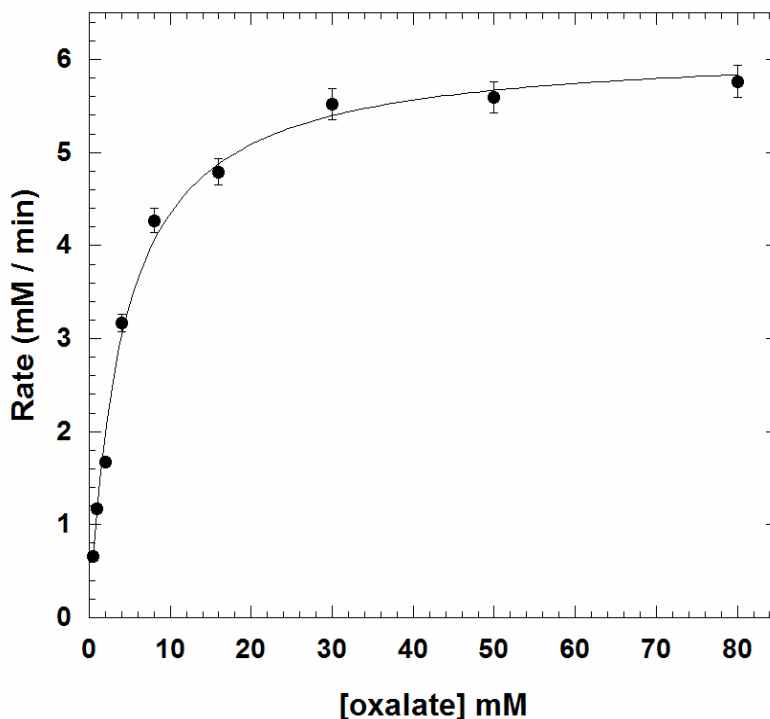


Figure 2-15. Initial rates of the appearance of $^{13}\text{CO}_2$ in solutions resulting from catalysis of the decarboxylation of oxalate by OxDC. Each data point represents a single measurement of initial velocity from the data of Figure 2-14. The solid line is a fit to the Michaelis-Menten equation (Eqn 2-1), with constants for catalysis given in Table 2-1. Reprinted from (36) with permission by Elsevier.

Oxalate containing two ^{13}C labels (99% ^{13}C) was used as substrate to distinguish catalytically generated $^{13}\text{CO}_2$ (m/z 45) from pre-existing $^{12}\text{CO}_2$ (m/z 44) in reaction samples. Progress curves were measured to show catalytically generated $^{13}\text{CO}_2$ at various initial concentrations of oxalate; the initial segments of such curves are shown in Figure 2-14. The slow phase in the beginning 8 – 12 sec is the response time. The initial velocities of the catalytic production of CO_2 were determined from the linear slopes of Figure 2-14 at times 5% to 10% of approximate product conversion. The rate of the uncatalyzed reaction is negligible as is the loss of CO_2 into the instrument and headspace. The initial rates of catalysis were adequately fit to a simple Michaelis-Menten curve (Figure 2-15) with catalytic constants given in Table 2-1. These constants

are in reasonable agreement with those determined by coupled assay using NAD-requiring formate dehydrogenase (Table 2-1). The Michaelis-Menten plot for the formate dehydrogenase assay is shown in Figure 2-16. From a concomitant decrease in the m/z 32 peak, such as shown in Figure 2-2, the measured rate of O_2 consumption which was determined to be 0.3% to 0.5% of the rate of overall catalysis by OxDC at saturating substrate (50 mM oxalate) and air equilibration, was due to the inherent catalysis of the oxidase reaction (Figure 1-1B). Under similar conditions Tanner et al. estimated this value to be 0.2% (7). This is too small a rate to affect significantly the constants for the decarboxylase activity given in Table 2-1.

MIMS measurement of product CO_2 in catalysis by OxDC from *B. subtilis* has obtained steady-state constants in reasonable agreement with those by an endpoint assay using formate dehydrogenase (Table 2-1). The values of k_{cat} and k_{cat}/K_m were somewhat larger when measured by MIMS, perhaps related to the advantages of MIMS in being able to provide a sensitive, continuous, and real-time measure of CO_2 in solution.

Table 2-1. Steady state constants for decarboxylation of oxalate catalyzed by polyhistidine-tagged OxDC measured by MIMS and by formate dehydrogenase coupled assay. Uncertainties are standard errors in the fit to the Michaelis-Menten expression (Equation 2-1). Reprinted from (36) with permission by Elsevier.

Assay	K_m (mM)	k_{cat} (s^{-1})	k_{cat}/K_m ($mM^{-1}s^{-1}$)
MIMS	4.0 ± 0.5	71 ± 2	18 ± 1
FDH-coupled Endpoint Assay	3.9 ± 0.4	44 ± 1	11 ± 1

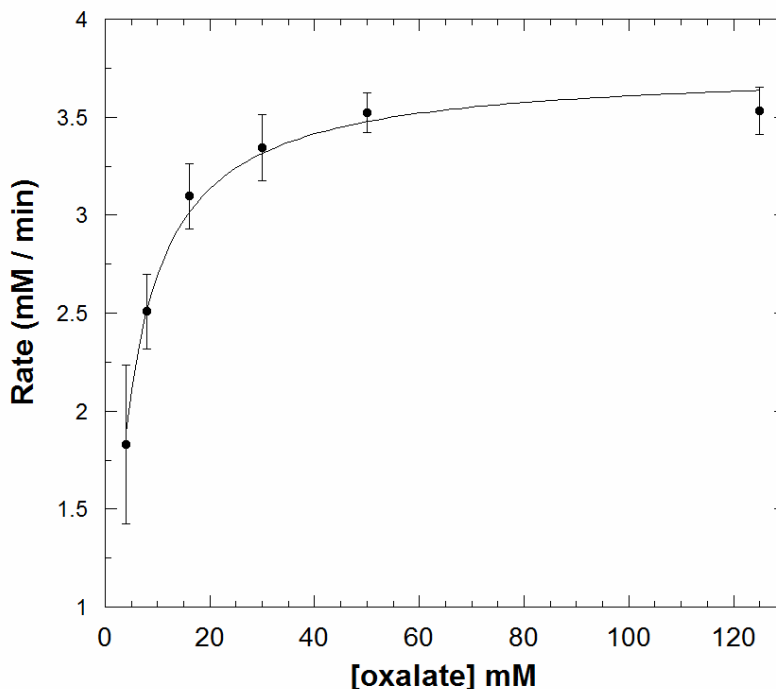


Figure 2-16. Initial rates of catalysis by polyhistidine-tagged *B. subtilis* oxalate decarboxylase determined by the formate dehydrogenase-coupled endpoint assay described in the Experimental section. One-minute experiments for the rate of formate production (mM/min) at each oxalate concentration were done in triplicate and fitted to the Michaelis-Menten expression (Eqn 2-1) resulting in an R^2 of 0.92334. The solid line is a fit to the Michaelis-Menten expression with derived steady-state constants given in Table 2-1. Reprinted from Supplementary Material (36) with permission by Elsevier.

Experimental Section

Materials

Protein concentrations were determined using the Coomassie Protein Plus Kit (Pierce, Rockford, IL) with calibration curves generated utilizing bovine serum albumin as standard. DNA sequencing services were done by the core facility of the Interdisciplinary Center for Biotechnology Research (ICBR) at the University of Florida. Solutions of carbon-13 oxalate ($^{13}\text{C}_2$ -labeled oxalic acid; 99% ^{13}C ; Cambridge Isotope Laboratories - Andover, MA) were prepared by adjusting pH to 4.2 with minimum amounts of potassium hydroxide.

His₆-tagged Oxalate Decarboxylase Expression and Purification

The OxDC:pET-32a plasmid construct for the polyhistidine-tagged wild-type *B. subtilis* OxDC was acquired from the research group of Dr. Stephen Bornemann of the John Innes Centre in Norwich, UK. This plasmid was cloned into BL-21/DE3 *E. coli* cells in which the polyhistidine-tagged wild-type OxDC was expressed and later purified using previously established methods (14, 15), except that grown cells were lysed via sonication. Pooled elution fractions from Ni-NTA agarose (Quiagen) affinity chromatography were eluted through a 100-mL G-25 Sephadex Desalting column equilibrated with 50 mM Tris-Cl (pH 8.5) and 0.5 M NaCl storage buffer.

Enzyme samples were treated with Chelex-100 resin (BioRad) for at least 1 hour with gentle swirling to remove trace metals. Final samples were buffer exchanged into Chelex-treated storage buffer and further concentrated to within 6 – 10 mg/mL using YM-30 Centriprep concentrators (Millipore). Purity was assessed from the 44 kDa protein band on a 12% resolving SDS-PAGE (sodium dodecyl sulfate-polyacrylamide gel electrophoresis) gel, from protein fractions taken at different stages of the purification.

Metal incorporation of purified protein (2.25 mgs) was quantified in 1% nitric acid protein solutions (18) by the ICP-MS (inductively coupled plasma mass spectrometry) (42) services of the University of Wisconsin Soil and Plant Analysis Laboratory. Our samples of OxDC contained 1.4 Mn/monomer. Each monomer contains two manganese binding sites, one of which is catalytic (1, 3, 43). We do not know the distribution of metal ions between these two sites. In the kinetic results reported here, the concentration of enzyme has been set equal to the protein content of solution.

Formate Dehydrogenase (FDH)-Coupled Activity Assay

OxDC activity was measured through an endpoint assay coupled with NAD⁺-requiring formate dehydrogenase enzyme (14, 18). Assay reaction mixtures were composed of 50 mM sodium acetate buffered at pH 4.2, 0.2% Triton X-100, 0.5 mM *o*-phenylenediamine, and 4 – 125 mM potassium oxalate. Reactions were initiated with the addition of 1.4 μM wild-type enzyme in a total reaction volume of 100 μL incubated at ambient temperature of 23 -25°C. The reaction was quenched after a predetermined amount of time with the addition of 1M sodium hydroxide (10 μL) and the amount of formate product was quantified by a coupled assay reaction using 50 mM potassium phosphate buffered at pH 7.8, 1.4 mM NAD⁺, and 0.4-1.0 U/mg of formate dehydrogenase at a final volume of 1 mL. The amount of NADH was measured by absorbance of assay mixtures at 340 nm after overnight incubation at 37°C. Corresponding production of formate was quantified against a calibration curve generated from the relative absorbances A_{340} of pre-quenched OxDC assay mixtures containing known amounts of formate (18).

Membrane Inlet Mass Spectrometry (MIMS)

The inlet probe to the mass spectrometer (Figure 2-1) comprised a 1 cm length of silicon rubber tube (1.5 mm i.d. and 2.0 mm o.d., Silastic a Dow Corning product), which was sealed by a glass bead at one end and interfaced to an Extrel EXM-200 quadrupole mass spectrometer (35). The inlet probe was immersed in a 2 mL reaction solution contained in a gas-tight quartz cuvette (1 cm pathlength). The reaction vessel was jacketed at a temperature of 25°C, and sealed with injection septa and Teflon screws for the introduction of samples and inert gas. This apparatus is previously described (44)

Experiments were initiated by the addition of enzyme or substrate, and masses were recorded continuously using an Extrel EXM-200 mass spectrometer at an electron impact ionization of 70 eV using an emission current close to 1 mA. Source pressures were approximately 1×10^{-6} torr. The reaction vessel was washed between experiments with a solution of 2.5 M KOH and 2.5 M EDTA, and thoroughly rinsed with deionized water in order to prevent any carry over of residual enzyme or unreacted material.

Reaction Mixtures

Reaction solutions for MIMS measurement contained the same components (except o-phenylenediamine) as those described in the FDH Coupled Activity Assay section, but scaled up to a final volume of 2-mLs. In order to more carefully assay initial rates of enzymatic CO₂ production and from detected non-enzymatic CO₂ in solution, either unlabeled or ¹³C₂-labeled oxalate (99%) was used as substrate. A trace amount of Antifoam A was added to prevent any loss of solution due to frothing when pre-reaction buffers were equilibrated by the bubbling of either air or helium gas (deoxygenated reaction conditions).

Depending on the desired buffer conditions, pre-reaction buffers were either air-equilibrated or deoxygenated (helium gas bubbling) until MIMS analysis showed baseline levels. To minimize any interfering signals from detected gases entering the reaction solution, a slow but continuous flow of air or helium gas was maintained on the headspace throughout the acquisition of data. Reactions were initiated by the addition of the required wild type, His₆-tagged OxDC so that the final enzyme concentrations were 1.4 μM, which was comparable to the amount of enzyme earlier used in the kinetic experiments employing the FDH endpoint assay. In later experiments (Chapter 4) enzyme aliquots used to initiate catalytic reaction were reduced to about 30-40% of the

original enzyme aliquot described above. Although the original recipe worked just fine, reducing the amount of wild-type enzyme not only extended the stock of purified enzyme, but also reduced the rate of catalytic generation of CO₂ enough for the instrument to report more points in the linear increase of the catalytic progress curves, where initial velocities were best sampled.

CHAPTER 3 NITRIC OXIDE INHIBITION OF CATALYSIS BY OXDC

Introduction

It is presently believed that decarboxylation proceeds from an oxalate radical anion intermediate, which is generated in a proton-coupled electron transfer step mediated by the Mn(II) ion (23). In addition, the reported dependence of the enzyme-catalyzed chemistry on the presence of dioxygen (7) has led to the proposal that formation of the oxalate radical anion takes place via a Michaelis complex in which both oxalate and dioxygen are bound to the catalytically active manganese center (10, 18, 22). Direct support for this hypothesis has yet to be obtained, however, and there is an absence of an unambiguous chemical precedent for the interaction of dioxygen with high-spin Mn(II) inorganic complexes. Efforts to observe the proposed interaction of dioxygen with the metal in OxDC have also been complicated by the fact that the two Mn(II) centers in the enzyme exhibit similar EPR properties (16, 17).

Nitric Oxide as Dioxygen Mimic

In an effort to assess the existence of the putative dioxygen binding site in OxDC, the interaction of nitric oxide (NO) with the enzyme was examined using the new continuous assay based on membrane inlet mass spectrometry (MIMS) mentioned in Chapter 2 (44, 45). Nitric oxide is similar to dioxygen in that it is a linear uncharged molecule which can also enter the membrane inlet of the instrument and be simultaneously detected with other gases in the solution throughout catalysis.

Nitric Oxide from NONOates

Nitric Oxide (NO) was generated in situ with the use of NONOates, which are stable organic compounds at basic pH 8.5. At pH 7.0 these compounds decompose,

generating known amounts of nitric oxide in solution (46-48). In acidic conditions (pH 4.2) these NO-generating reactions are instantaneous making NONOates a non-invasive and efficient source of NO for the OxDC catalytic reaction mixtures in this chapter.

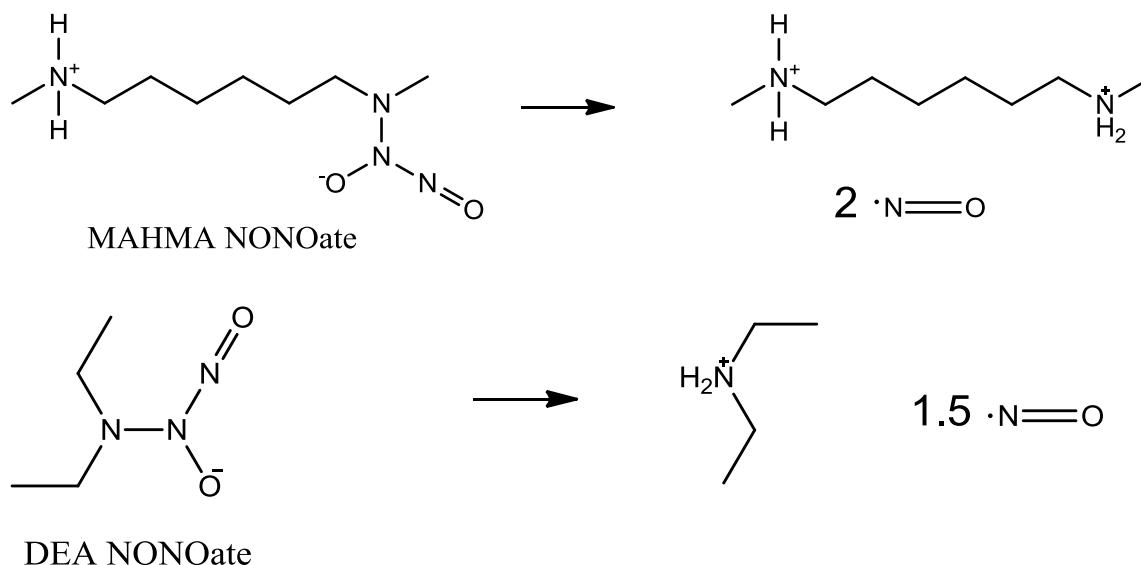


Figure 3-1. Structures of MAHMA / DEA NONOates at pH 8.5, and their respective reaction byproducts at pH ≤ 7 .(46-48)

Because nitric oxide rapidly oxidizes in the presence of oxygen, especially in acidic conditions (49), experiments in this chapter were conducted under deoxygenated buffer conditions (ie. equilibrated by the bubbling of helium). In order to test for the effects of nitric oxide on catalysis by OxDC, the overall pre-reaction scheme had to be slightly modified (Figure 3-2). In the modified scheme, reaction buffers were deoxygenated and equilibrated as previously described prior to data collection ($t = 0$ mins). In contrast to previous runs, the reaction buffer containing substrate was then injected with a known amount of NONOate in order to populate the reaction mixture with known amounts of nitric oxide (Figure 3-2 blue path) prior to initiating the reaction by the addition of OxDC enzyme.

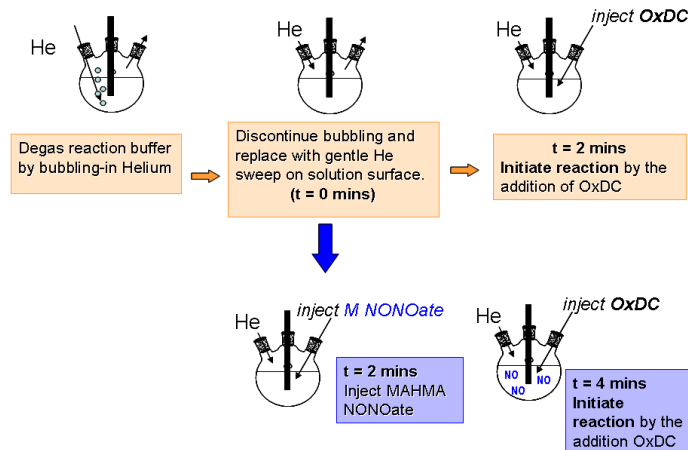


Figure 3-2. Modified experimental scheme for testing the effects of NO on catalysis by OxDC. Reactions were performed under deoxygenated conditions (orange path) similar to previously described wild-type experiments in Chapter 2. Modified scheme is illustrated by the divergence in the scheme (blue path), where the reaction buffer is first populated with NO, prior to the initiation of catalysis by the addition of OxDC enzyme.

Data Analysis: Inhibition

The hyperbolic Michaelis Menten function (Eqn 2-1) can be linearized by taking its inverse (Eqn 3-1) and plotting catalytic rates (v) at varying substrate concentration $[S]$ on a double reciprocal (Lineweaver-Burk) plot $1/[S]$ vs. $1/v$ (50). This approach facilitates a good preliminary estimate of the kinetic parameters of the catalytic experiment through a least squares fitting of the data points to these reciprocal equations.

$$\frac{1}{v} = \left(\frac{K_m}{V_{\max}} \right) \frac{1}{[S]} + \frac{1}{V_{\max}} \quad (3-1)$$

Although lesser points are required to derive a good fit to a linear function than to a highly resolved hyperbolic curve, a disadvantage of the reciprocal approach is the inherent error on derived catalytic constants contributed by the lower catalytic rates at low substrate concentrations (farthest points from the axes). Because these lower catalytic rates are experimentally harder to measure and thus prone to the most error,

variances in these measurements graphically have a considerable effect on the slope (K_m/V_{max}) and extrapolated y-intercept (V_{max}) of the fitted linear equation. This effect becomes a greater concern in inhibition experiments where diminished catalytic rates (compared to wild-type controls) are expected and when estimates for the mode of inhibition are accomplished through global fits.

Modes of inhibition presented later in the chapter and in Chapter 4 were derived by globally fitting sets of catalytic rates at varying inhibitor and substrate concentration to kinetic models of simple competitive, uncompetitive, and mixed/noncompetitive. The program incorporates a v^4 weighting algorithm in this process, which will later be described.

Different kinetic models have qualitative implications on the inhibitor-enzyme interactions and can be expressed in modified rate equations on which the global-fitting program is based. Theoretical effects of inhibitors are expressed by the function α which relates inhibitor concentration $[I]$ with its corresponding dissociation constant K_i . By definition, K_i refers to the concentration of inhibitor required to occupy half the total available enzyme at steady state conditions. α' is defined in the same way, but distinguishes itself from α by the form of the enzyme it targets in catalysis, which will be later discussed.

$$\alpha = 1 + \frac{[I]}{K_i} \quad (3-2)$$

Although much of these concepts will be revisited in Chapters 3 and 4, it would be useful at this point to describe the main implications of the different modes of inhibition and how they relate to the kinetic parameters derived from the data.

Michaelis Menten kinetics is grounded on the basic enzymatic scheme where free enzyme [E] interacts with substrate [S] to form a hypothetical form/complex [ES]. This form undergoes catalysis to form product [P] which is then released, regenerating the free form enzyme [E] for another catalytic cycle (40):



Figure 3-3. Fundamental enzymatic reaction model.

The model is limited by the fact that it views the reaction from the perspective of reactants and products and thus gives no clear indication of mechanism, or individual steps within the scheme which may very well exist. Nonetheless inhibitors in theory, interfere with catalysis by targeting different hypothetical forms of the enzyme in the catalytic scheme, depending on their mode of inhibition (40, 41).

Competitive inhibitors are species which target the free form of the enzyme [E] (Figure 3-4), thus “competing” with substrate for the same enzymatic form required for it to bind to and undergo catalysis. Although many competitive inhibitors are structural analogues of the substrate, a competitive inhibitor may not always be assumed to bind to the exact same binding site of the substrate on the enzyme.

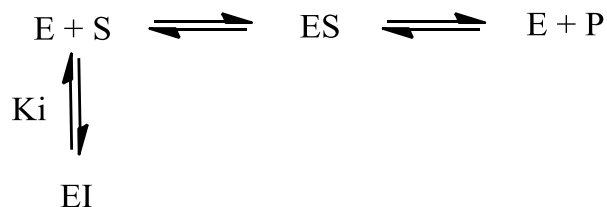


Figure 3-4. Enzymatic scheme for competitive inhibition.

Because they interfere with the interaction of substrate on the enzyme, more substrate is essentially required to achieve V_{max} . K_m is essentially affected even though V_{max} ideally remains unchanged. From the linearized Michaelis-Menten equation earlier

the two forms it can target, ie. $K_i \neq K_i'$ (mixed). For simplicity, mixed modes of inhibition will be considered similar to noncompetitive, which is distinct from previously described competitive and uncompetitive models. Because noncompetitive/mixed inhibitors inhibit regardless of the presence of the substrate, it is implied that these species interact with the enzyme at a location on the enzyme other than the substrate binding site.

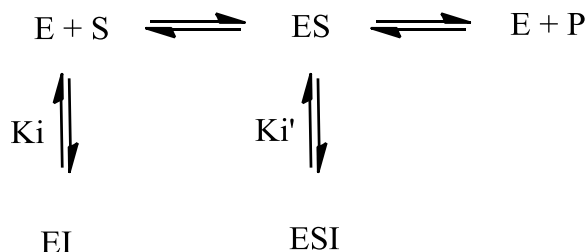


Figure 3-6. Enzymatic scheme for noncompetitive/mixed inhibition.

The rate equation associated with this mode of inhibition (Eqn 3-5) is described as a combination of the two previously described equations, where the respective effects of the two illustrated K_i s (Figure 3-6) are reflected by the corresponding α and α' denotations. These effects simply convey the unique feature of this mode, where the inhibitor targets both $[E]$ and $[ES]$ forms of the enzyme as indicated in Figure 3-6.

$$\frac{1}{v} = \left(\frac{\alpha K_m}{V_{\max}} \right) \frac{1}{[S]} + \frac{\alpha'}{V_{\max}} \tag{3-5}$$

Given these different models of inhibition, the fitting program uses a series of matrix elimination functions to find the kinetic parameters which best fit the spread of initial velocities (discussed in Chapter 2) measured at varying inhibitor and substrate concentrations. Kinetic parameters derived for each of the three possible modes of inhibition are assessed in this process with the best fit often indicated by an R^2 correlation value of no less than 0.9. Bad fits often reveal themselves with correlation values of 0.8 or less.

In order to compensate for the error described from the linearization of the Michaelis-Menten equation, weighting factor (w_i) was incorporated in the fitting program used on the catalytic rates (v_i) in our inhibition experiments (Eqn 3-6).

$$w_i = \frac{v_i^4}{\text{Variance}(v_i)} \quad (3-6)$$

This factor essentially biases the fitting towards putting more weight on the higher velocities measured, where errors are presumably not as high. When the variance of measured velocities are assumed to be constant, the weighting factor essentially becomes v^4 (51) – hence the name of the algorithm. This assumption holds true in many cases where “rates are measured at a constant enzyme concentration”(51, 52), which is the case in each of our mode of inhibition experiments. Furthermore, this assumption of constant variance assumes that the range of measured velocities across all substrate concentrations is no more than a factor of 5. In cases when this does not hold true and experimental velocities for example, range by a power of 10 or more, the assumption of constant variance no longer applies and results in the exclusion of the lower velocities in the v^4 weighted fitting process (50). This may explain why graphical representations of the fitted parameters of our data give a much poorer fit to the data sets of highest inhibitor concentrations and low substrate concentration.

In order to illustrate the results of the global fitting of the data, coordinates are manually calculated from the constants and model equation derived by the fitting software. Specific modes of inhibition are indicated by distinct patterns of lines resulting from the fitting of catalytic at varying inhibitor and substrate concentration (Table 3-2). Linearized catalytic rates are often plotted on a double reciprocal (Lineweaver-Burke) plot of $1/v$ vs. $1/[S]$. However an alternative known as the Hanes plot, is preferred on

account that the plot minimizes the effect of the errors from lower catalytic rates at low substrate concentrations (41). Hanes plots by contrast, plot substrate concentration [S] against the reciprocal of the corresponding initial velocity multiplied by the substrate concentration ($[S]/v$). Derived kinetic constants are illustrated through distinct graphical features of each plot as summarized in Table 3-1 (40, 41, 53).

Table 3-1. Table of comparison between graphical features of Lineweaver-Burke and Hanes plots.

Graphical Features	Lineweaver-Burke Plot	Hanes Plot
Linear rate equation	$\frac{1}{v} = \left(\frac{K_m}{V_{\max}} \right) \frac{1}{[S]} + \frac{1}{V_{\max}}$	$\frac{[S]}{v} = \frac{K_m}{V_{\max}} + \frac{[S]}{V_{\max}}$
Slope of the line	$\frac{K_m}{V_{\max}}$	$\frac{1}{V_{\max}}$
y-intercept	$\frac{1}{V_{\max}}$	$\frac{K_m}{V_{\max}}$
x-intercept	$-\frac{1}{K_m}$	$-K_m$

Table 3-2. Modes of Inhibition represented by Lineweaver Burke and Hanes Plots. Linear patterns in each plot resulting from the linear fits of initial reaction velocities at varying substrate and inhibitor concentrations.

Mode of Inhibition	Lineweaver-Burke Plot	Hanes Plot
Competitive Inhibition	Intersecting lines at y-axis	Parallel Lines
Uncompetitive Inhibition	Parallel Lines	Lines converging at y-axis
Noncompetitive Inhibition	Lines converging at negative x-axis	Lines converging at negative x-axis
Mixed Inhibition	Lines intersecting at a point in quadrant I (ie. where $x < 0$ and $y > 0$)	Lines intersecting at a point in quadrant I (ie. where $x < 0$ and $y > 0$)

Results and Discussion

Reversible Inhibition of NO

Figure 3-7 shows the decrease in initial activity of the enzyme by approximately two orders of magnitude in the presence of NO, as indicated by the reduction in the

observed ion current for $^{13}\text{CO}_2$ ($m/z = 45$). Here, an assay solution containing 50 mM $^{13}\text{C}_2$ -oxalate in 50 mM acetate buffer, pH 4.2, was degassed with He to deplete dioxygen. Air in the head space above the reaction mixture was then removed with He for 2 min prior to the addition of 25 μM MAHMA NONOate (46, 47). Under the acidic conditions, this reagent rapidly decomposed to yield 50 μM NO (Figure 3-7). OxDC (1.4 mM) was then added to the solution at 4 min to initiate the decarboxylation reaction (Figure 3-7). Under these conditions, the ion associated with NO ($m/z = 30$) was also detected.

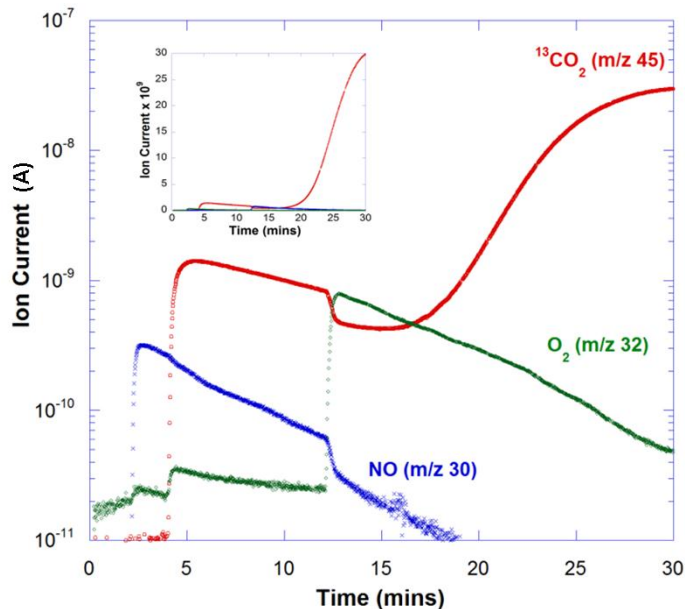


Figure 3-7. Effect of NO on catalysis by C-terminally His₆-tagged OxDC. Time course of changes in ion currents (arbitrary units), determined using MIMS for $^{13}\text{CO}_2$ (red), NO (blue) and O₂ (green). At 2 minutes, 25 μM MAHMA NONOate was injected into deoxygenated buffer containing 50 mM $^{13}\text{C}_2$ -oxalate, 0.2% Triton-X and 50 mM Acetate pH 4.2. Catalysis was initiated 2 minutes later by the addition of 1.44 μM His₆-tagged OxDC. CO₂-free air was bubbled in for 30 seconds at 12 minutes. (Inset) The same set of data plotted on a linear axis to emphasize the magnitude of the ion currents for $^{13}\text{CO}_2$ (red) and NO (blue). Reprinted from (54) with permission by the Royal Society of Chemistry.

Even in the presence of NO, the enzyme was capable of catalyzing the formation of a small amount of $^{13}\text{CO}_2$ immediately on addition, which likely results from the

presence of the bound dioxygen on the enzyme added to the reaction mixture. The time-dependent decrease in the ion current for both these species over the next 8 min was due at least in part, to the loss of CO₂ and NO from the reaction solution through the membrane inlet into the mass spectrometer. At 12 min, air was re-introduced, resulting in the restoration of full OxDC catalytic activity, albeit after a time lag of approximately 5 min (Figure 3-7). Upon introduction of air by bubbling, some CO₂ was lost from solution, giving rise to a decrease in the ion current of the m/z 45 peak.

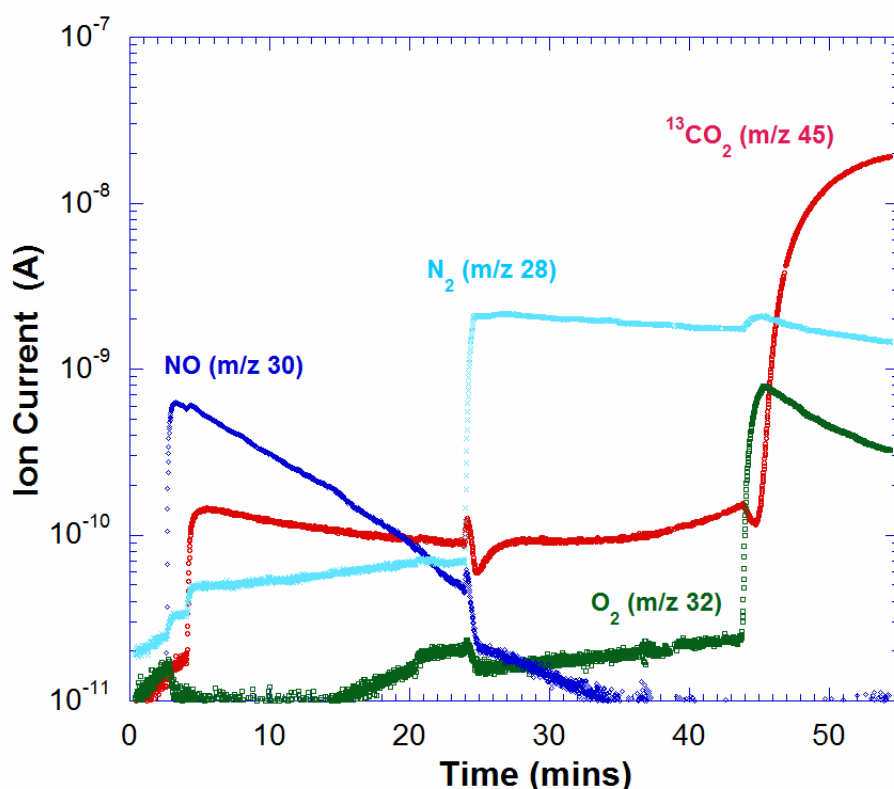


Figure 3-8. Effect of N₂ on catalytic inhibition by NO. Same reaction conditions as in Figure 3-7, except that reaction was initiated with M NONOate-treated enzyme stock and instead of air, N₂ (cyan) was bubbled in at t = 24 minutes, followed by CO₂-free air 20 minutes later.

To confirm that recovered activity was not simply due to the removal of NO from solution as a consequence of bubbling in air, a similar experiment was conducted where NO was deliberately removed from the inhibited reaction mix by the bubbling of nitrogen

gas instead of air (Figure 3-8). The fact that catalytic CO_2 was only recovered after the later bubbling in of air confirmed that inhibition was indeed reversed by dioxygen.

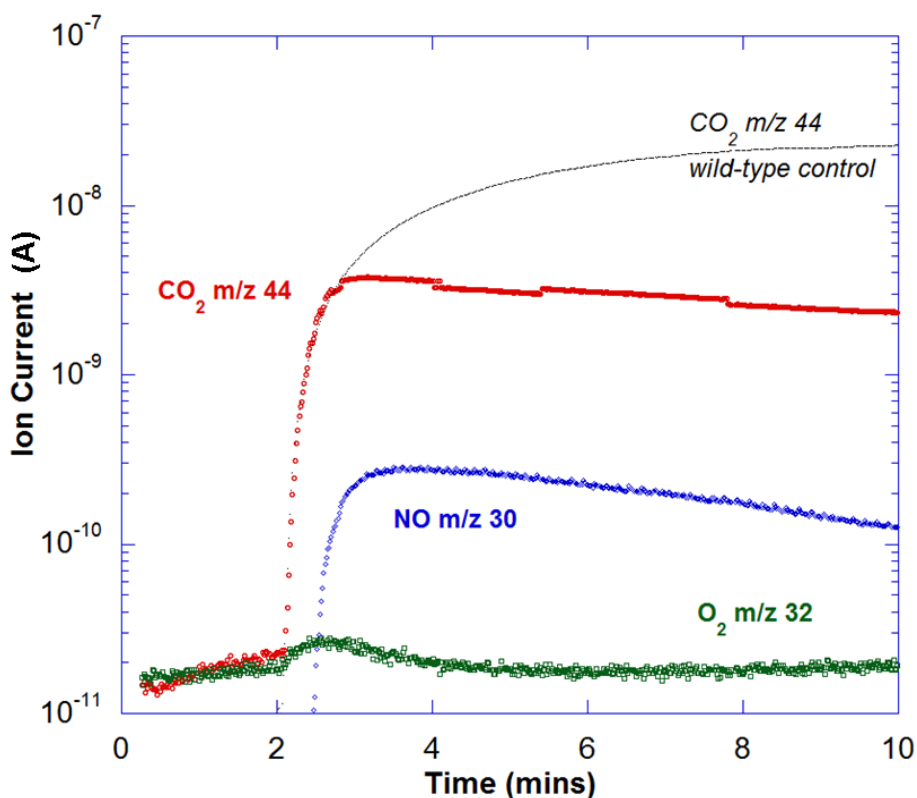


Figure 3-9. MIMS experiment showing the effect of adding MAHMA NONOate to OxDC during catalytic turnover. Pre-reaction buffers were deoxygenated as described in Figure 3-7. After 2 min, His₆-tagged, wild type OxDC (1.4 μM) was added to initiate reaction. CO_2 generation took place immediately (red). After an additional 20 seconds, a solution of 50 μM of MAHMA NONOate was injected into the reaction mixture and NO formation was observed (blue). The dioxygen concentration under these conditions was also monitored (green). OxDC activity under identical conditions in the absence of NO is also indicated on the MIMS plot (thin black line), showing that NO inhibition does not result merely from dioxygen depletion due to chemical reaction and NO_2^- formation. Reprinted from Supplementary Material of (54) with permission by the Royal Society of Chemistry.

In order to test the alternate hypothesis that decreased OxDC activity resulted merely from dioxygen depletion due to the reaction of the latter gas with NO under the acidic conditions, (55) rate of CO_2 formation at similarly low dioxygen levels in the absence of MAHMA NONOate was measured. Under these conditions the intrinsic

OxDC decarboxylase activity was higher than that seen when MAHMA NONOate was present, ruling out this possibility (Figure 3-9).

OxDC inhibition by DEA NONOate

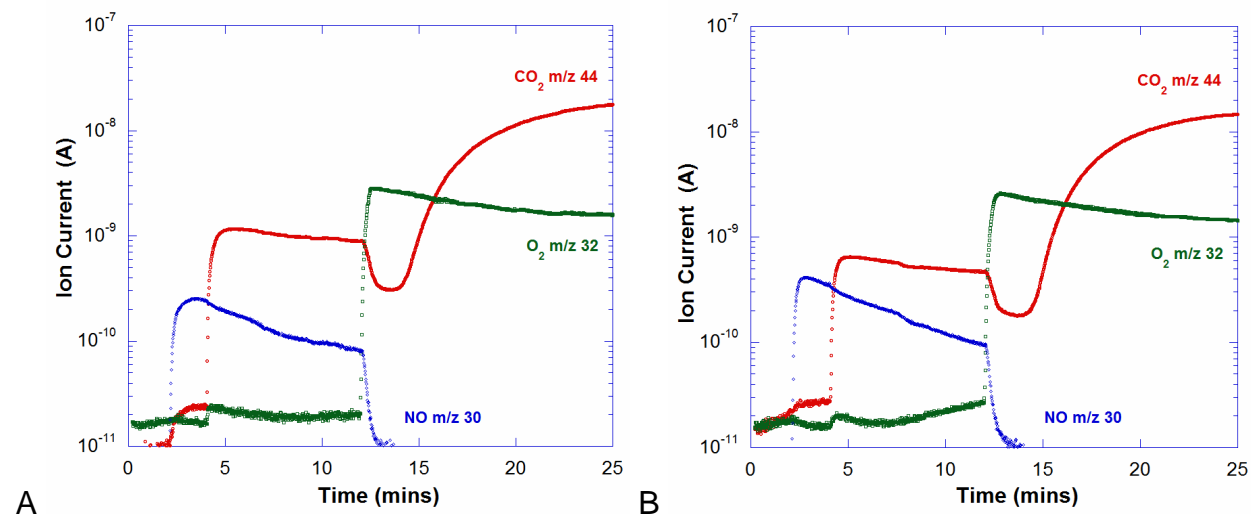


Figure 3-10. MIMS experiments showing that OxDC inhibition is not dependent on the source of NO. (A) Deoxygenated reaction buffer described in Figure 3-7. At 2 min (during which time He was used to remove gases from the “headspace” above the reaction solution), MAHMA NONOate was added to the solution mixture (final concentration $37.5\mu\text{M}$) and NO formation was observed (blue). After an additional 2 min, catalysis was initiated by the addition of $1.4\mu\text{M}$ His₆-tagged OxDC and CO₂ production was monitored (red). After a further 8 min, pure O₂ (green) was bubbled into solution for 30 seconds. (B) Identical experimental conditions except that NO was generated from diethylammonium (Z)-1-(N,N-diethylamino)diazene-1-ium-1,2-diolate (final concentration $50\mu\text{M}$). Reprinted from Supplementary Material of (54) with permission by the Royal Society of Chemistry.

Control assays using an alternate NO-releasing reagent – DEA NONOATE (diethylammonium (Z)-1-(N,N-diethylamino) diazene-1-ium-1,2-diolate) suggested that the by-product formed after NO release from MAHMA NONOate was not responsible for the observed inhibition (Figure 3-10). Here, equimolar amounts of NO were generated in solution based on the respective stoichiometries documented for each NONOate. The identical profile of reversible inhibition in the presence of O₂ supports the assumption that inhibition of catalysis by OxDC is due to NO.

Dependence of OxDC inhibition on NONOate concentration

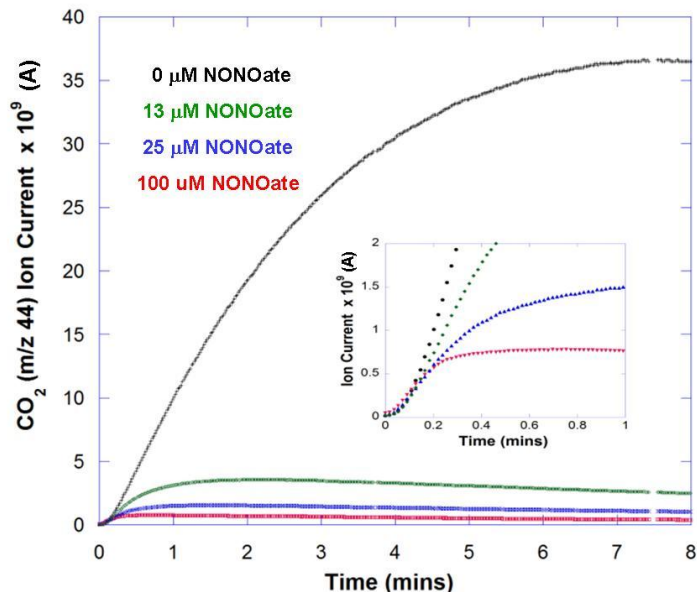


Figure 3-11. Dependence of OxDC inhibition on initial MAHMA NONOate concentration. Progress curves for the generation of $^{12}\text{CO}_2$ under anaerobic conditions, as measured by ion current in the MIMS procedure (arbitrary units), in the presence of MAHMA NONOate at an initial concentration of $0\ \mu\text{M}$ (black), $13\ \mu\text{M}$ (green), $25\ \mu\text{M}$ (blue) and $100\ \mu\text{M}$ (red). Catalysis was initiated at $t = 0$ by the addition of $1.4\ \mu\text{M}$ C-terminally His6-tagged OxDC. Other reaction conditions were those used to generate the data in Figure 3-7. (Inset) An expanded plot of the data generated during the first minute of reaction using a linear axis to emphasize differences in magnitude of $^{12}\text{CO}_2$ production. Reprinted from (54) with permission by the Royal Society of Chemistry.

Varying the initial amount of MAHMA NONOate under identical experimental conditions established that the extent of OxDC inhibition was dependent on NO concentration, consistent with an NO binding site on the enzyme (Figure 3-11). Initial plateau in the progress curves is the response time of the instrument as described in Chapter 2.

Mode of Inhibition of NO

A measure of initial velocities in reactions with varying concentrations of substrate and NO showed a distinct uncompetitive mode of inhibition by the convergence of lines on the ordinate (K_m/V_{max}) of Figure 3-12. The data at the largest concentration of NO did

not adhere well to the magnitude of values projected by the global fit in Figure 3-12. This was possibly due to the experimental limits of detecting lower initial rates, which may already be taking place within the response time of the instrument. Alternatively, higher concentrations of NO may result in hitherto undetected [ESI] forms of the enzyme, manifesting in a deviation of the fit to the standard uncompetitive inhibition equation. Regardless, the v^4 fitted data were consistent with an uncompetitive mode of inhibition with a derived K_i of $40 \pm 1 \mu\text{M}$, which is of a similar magnitude to the K_m for O_2 of $28 \pm 8 \text{ mM}$ (measured from the dependence of decarboxylase activity on dioxygen concentration) (14). This indicates that NO inhibits OxDC by targeting a form of the enzyme when substrate is present. It may further suggest that dioxygen either binds after binding of substrate, or that the putative O_2 pocket is more accessible after substrate binds to the enzyme.

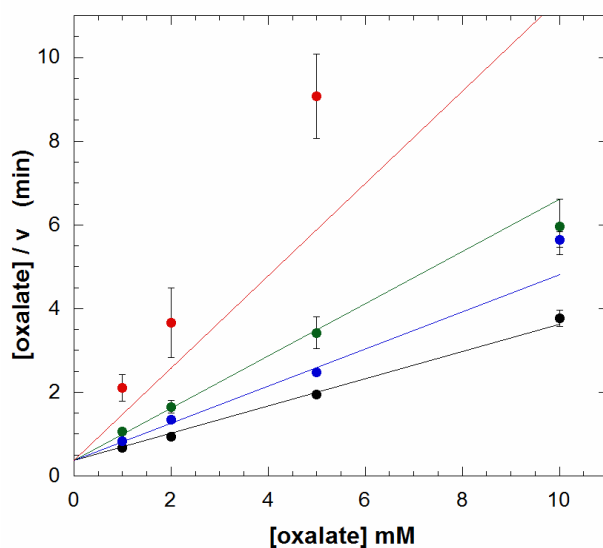


Figure 3-12. Mode of Inhibition of NO. Hanes-Woolf plot of single measurements in OxDC catalytic rates measured from changes in m/z 45 ion currents ($^{13}\text{CO}_2$) in oxygen depleted reactions containing 0.2% Triton-X, 1 – 10 mM of $^{13}\text{C}_2$ -oxalate, $1.44 \mu\text{M}$ C-terminally His₆-tagged OxDC in the presence of (black) 0, (blue) 10, (green) 25 and (red) 66 μM DEA NONOate, buffered at pH 4.3 with 50 mM sodium acetate. Solid lines are v^4 weighted global fits of all data, which fit best to an Uncompetitive mode of inhibition model.

Inhibition of NO on catalysis by site-specific mutants of OxDC

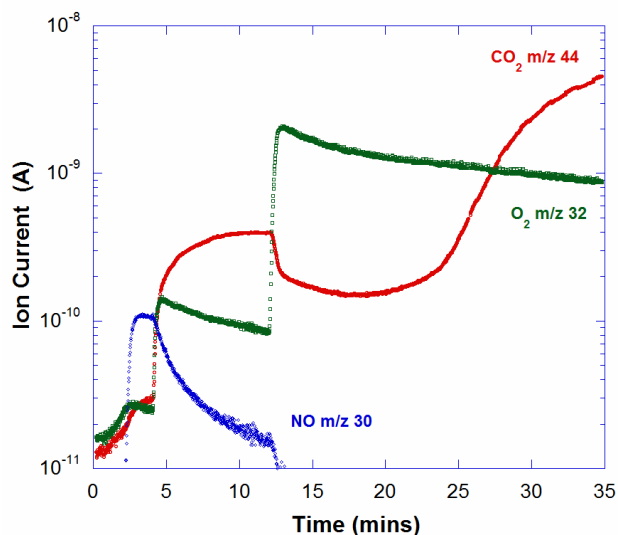


Figure 3-13. Effect of NO on catalysis by untagged C383S OxDC mutant. Time course of changes in ion currents (arbitrary units), determined using MIMS for ¹²CO₂ (red), NO (blue) and O₂ (green). Full experimental details are described in Figure 3-7 except that 0.43 μM C383S OxDC was used to initiate catalysis and pure O₂ was bubbled in for 30 seconds at t = 12 minutes. Reprinted from Supplementary Material of (54) with permission.

Given that NO-dependent OxDC inhibition could be reversed by the re-introduction of dioxygen, it was postulated that the NO inhibited decarboxylase activity by binding to the Mn(II) center, possibly at a coordination site occupied by dioxygen during catalytic turnover,(22) or by nitrosylating the side chain of Cys-383 in the protein, (56) which is located at the C-terminus distant from the putative catalytic site (9, 10). The latter proposal was ruled out, however, by the fact that the C383S OxDC mutant exhibited identical catalytic behavior to the wild type enzyme, including reversible inhibition by NO under the conditions of our earlier experiments (Figure 3-13). C383 is the only cysteine in the amino acid sequence of *B.subtilis* OxDC and is three residues away from the C-terminal end (Figure B-3A). Furthermore, the possibility that observed inhibition by NO is due to interactions with the C-terminal polyhistidine tag was likewise eliminated by the fact that the C383S OxDC mutant had no polyhistidine tag. This was confirmed by

identical results between native wild-type OxDC and C-terminally His₆ tagged OxDC in the presence of NO.

Inhibition caused by covalent modification of tyrosine residues, as observed in Mn-dependent superoxide dismutase, seemed unlikely since such modifications would be irreversible, even in the presence of abundant O₂. Regardless, similar experiments were conducted on the Y200F OxDC mutant, whose mutation replaces the only conserved tyrosine found to affect decarboxylase activity (Shukla, M. unpublished). Y200F only possessed 1/4th the activity of wild-type. Contrary to the hypothesis that this mutant would be unaffected by the presence of NO, reversible inhibition in the presence of O₂ was observed to be identical to that of wild-type (Figure 3-14).

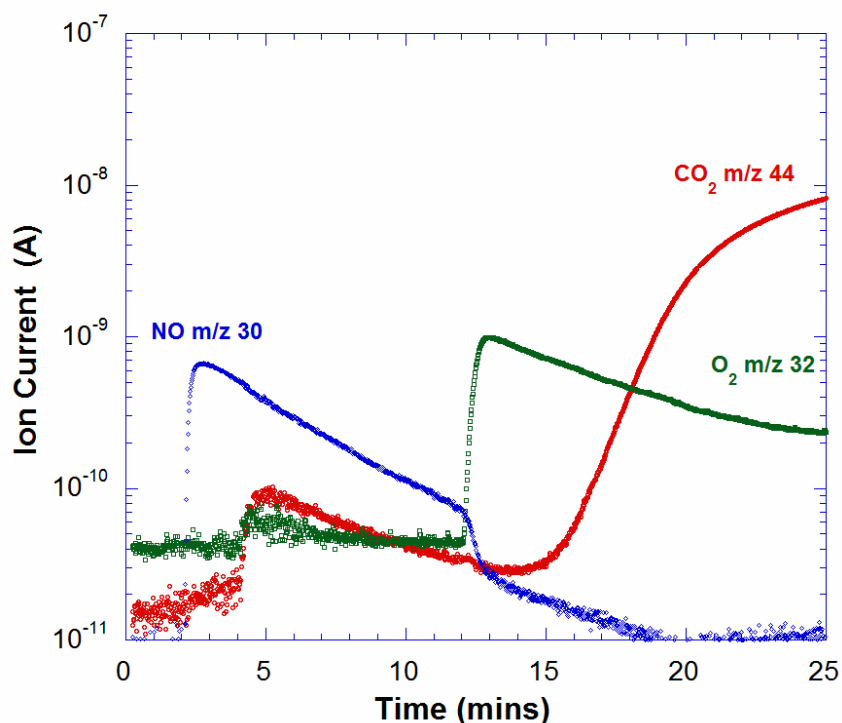


Figure 3-14. Effect of NO on catalysis by Y200F OxDC mutant. Time course of changes in ion currents (arbitrary units), determined using MIMS for ¹²CO₂ (red), NO (blue) and O₂ (green). Full experimental details are described in Figure 3-7 except that catalysis was initiated by 1.0 μM Y200F (Shukla, M. unpublished) OxDC mutant.

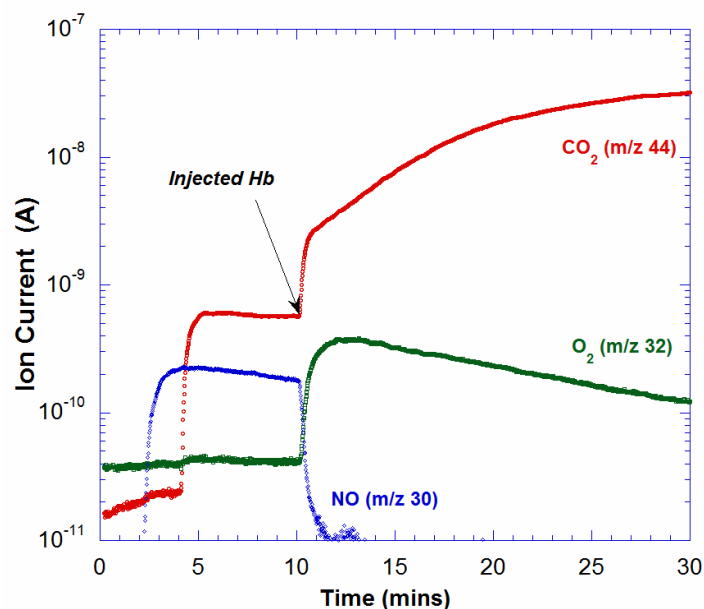


Figure 3-15. Effect of hemoglobin on catalytic inhibition by NO. Time course of changes in ion currents (arbitrary units), determined using MIMS for $^{12}\text{CO}_2$ (red), NO (blue) and O_2 (green). Full experimental details are described in Figure 3-7 except that NO was generated from $35\mu\text{M}$ DEA NONOate, $50\ \mu\text{L}$ s of hemoglobin was added at 12 minutes instead of air, and catalysis was initiated by $0.3\mu\text{M}$ C-terminally His₆-tagged OxDC. O_2 and CO_2 from the hemoglobin aliquot is indicated by the rise in these signals at $t = 12$ minutes. Detected catalytic CO_2 (red) recovered is concomitant to the plateau of exogenous O_2 (green).

Observed lag time preceding the reversal of inhibition was a consistent feature in these NO experiments and was further observed to be indirectly dependent on the amount of O_2 introduced into the inhibited system (ie. the more O_2 introduced, the shorter the time lag prior to the recovery of catalytic CO_2). Furthermore, the alternative addition of hemoglobin over air/oxygen to the NO-inhibited system, similarly resulted in the reversal of inhibition but without the time lag (Figure 3-15). The ability of hemoglobin to more rapidly recover catalytic CO_2 confirms a reversible non-covalent interaction of molecular NO within the enzyme, ruling out a suspected inhibitory NO-adduct which would otherwise be unaffected by the presence of hemoglobin. This further suggests that the observed time lag preceding the reversal of NO inhibition by O_2 is more likely

due to a chemical reaction with enzyme-bound NO rather than simple displacement of it. In order to more thoroughly verify the effect of hemoglobin on enzyme-bound NO, a similar experiment was repeated (Figure 3-16) where the NO-inhibited system was purged of remaining NO in solution by the bubbling-in of nitrogen gas (N_2). Similar to an earlier experiment (Figure 3-8) where OxDC remained inhibited after the removal of NO from solution, it was only in the addition of hemoglobin (at $t = 15$ minutes) where catalytic CO_2 was regenerated, as indicated by a noteworthy rise in the red signal starting from $\sim 3 \times 10^{-9}$ A. Initial spike in CO_2 upon injection of hemoglobin is due to the introduction of CO_2 from the hemoglobin aliquot. Nonetheless, catalytic recovery in this experiment was not preceded by the usual lag time observed when the inhibition was reversed by oxygen.

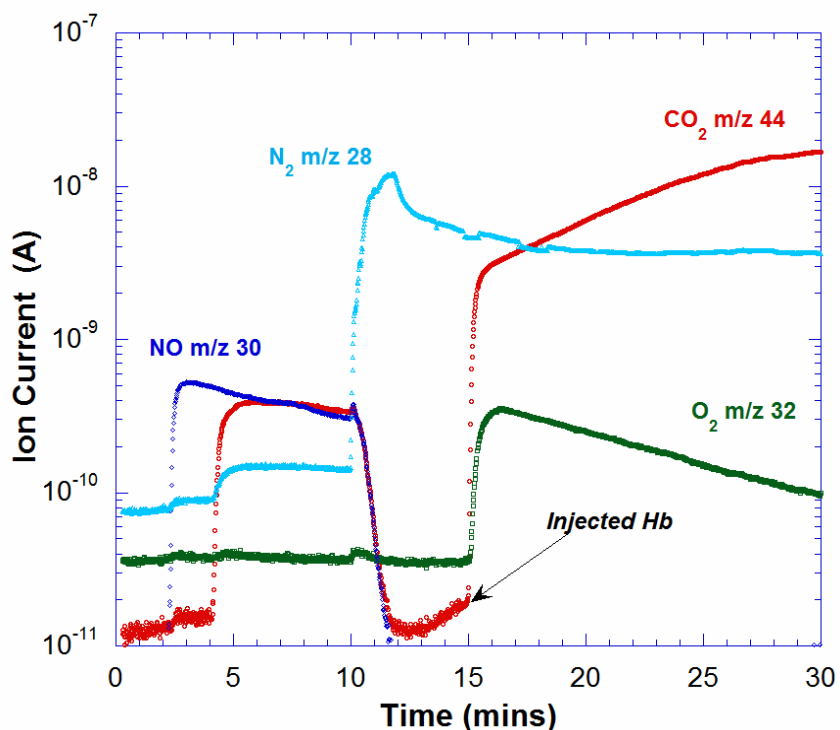


Figure 3-16. Effect of hemoglobin on catalytic inhibition by NO after bubbling with N_2 . Same experiment as in Figure 3-15, except that N_2 gas (cyan) was bubbled into the inhibited system at $t = 10$ minutes. Recovery of catalytic CO_2 was observed only after addition of hemoglobin at $t = 15$ minutes.

Constant Wave Electron Paramagnetic Resonance (CW-EPR) Experiments

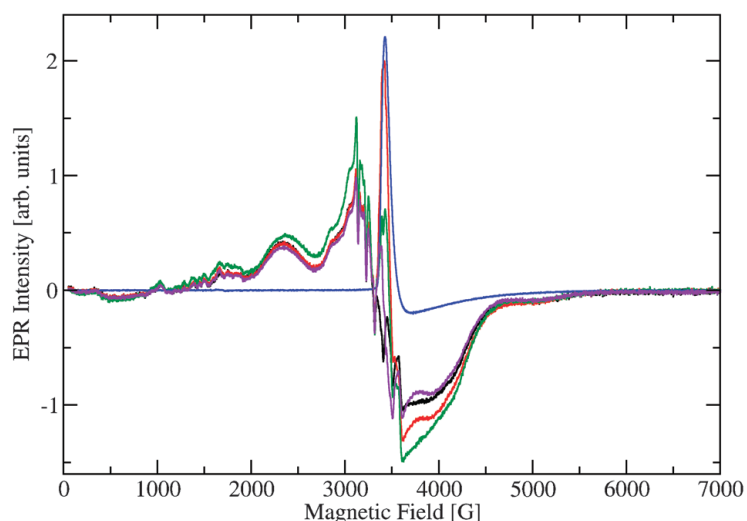


Figure 3-17. Overlaid CW-EPR spectra of the Mn (II) centers in OxDC in the presence and absence of NO released from MAHMA NONOate. (A) Degassed (Ar) sample of WT OxDC in 110 mM acetate buffer, pH 4.1 (black). (B) Same sample as in (A) to which MAHMA NONOate was added (red). (C) Degassed (Ar) sample of WT OxDC in 110 mM acetate buffer, pH 4.1, containing MAHMA NONOate and oxalate (green). (D) Metal-free 110 mM acetate buffer, pH 4.1, containing released NO (blue), and the difference spectrum (purple) generated by subtraction of (D) from (B). All spectra were recorded at 4.2 K. Reprinted from (54) with permission by the Royal Society of Chemistry.

A series of EPR measurements were performed on frozen solutions of OxDC containing NO with the expectation that NO might bind to one, or both, of the high-spin Mn(II) centers present in OxDC (17). As a result, it was anticipated that the intensity observed for the EPR signal(s) associated with the Mn(II) centers would decrease because the interaction of NO with the enzyme would yield a Mn(III) species possessing an integer spin, which would be “silent” in our EPR measurements. Briefly, wild type OxDC (0.12 mM) was dissolved in 110 mM KOAc buffer, pH 4.1, which had been carefully degassed by sparging with argon (120 mL total volume). After freezing in liquid isopentane pre-cooled in liquid N₂, CW-EPR spectra were taken at 4.2 K (Figure 3-17). The initial degassed OxDC sample showed the usual X-band spectrum for the bound Mn(II) ions, (10) i.e. six relatively sharp lines exhibiting the average hyperfine coupling

constant of 92 G typical of hexa-coordinated manganese (57). In addition, the spectrum shows a shoulder at 3050 G and a broad maximum centered at 2340 G. Using multi-frequency EPR measurements, we have interpreted this spectrum as arising from two different Mn(II) sites with fine structure parameters of $|D|=1200$ MHz and 2150 MHz (17).

Recent work has suggested that the X-band EPR spectrum of the enzyme is likely sensitive only to the Mn(II) site possessing the smallest fine structure constant D . This sample was then mixed with 0.5 mM MAHMA NONOate (full details are in the Experimental section) and we examined whether there was a change in the intensity of all, or parts of, the Mn(II) signal when OxDC was exposed to NO. Perhaps unexpectedly, the Mn(II) signal in the EPR spectrum of OxDC under these conditions was of approximately the same intensity as that observed in the absence of NO (Figure 3-17). Although there was some background signal from MAHMA NONOate (presumably arising from free NO), subtraction of the relevant spectra showed a reduction in Mn(II) signal intensity of only 10–20% in conditions under which NO completely inhibited the decarboxylase activity (Figure 3-17). Such a decrease is expected to be associated solely with OxDC sample dilution resulting from addition of the MAHMA NONOate solution. A sample of OxDC that contained both MAHMA NONOate and oxalate also gave similar results when analyzed using our standard EPR procedures (Figure 3-17). These observations seem to indicate that NO does not exert its inhibitory effect on decarboxylase activity by displacing dioxygen from the metal center or by forming a heptacoordinate Mn(II) species, at least for the site that is visible in the X-band EPR spectrum. High-frequency EPR analysis of OxDC by other workers

has also suggested that the Mn(II) site exhibiting the smaller fine structure value D is actually located in the N-terminal domain of the enzyme (16), this assignment being based on spectroscopic evidence for the presence of a pentacoordinate Mn(II) center in OxDC at high solution pH (10). If this interpretation is correct then our findings would seem to exclude NO binding at the solvent accessible catalytically active N-terminal site (9). These observations are also consistent with the remarkably small number of well characterized mononuclear {Mn–NO} complexes that have been reported (58-60). We also note that only circumstantial evidence for the formation of Mn(III) during catalytic turnover (a metal species that might bind NO) has been reported (61). On the other hand, it remains possible that any Mn(II)/NO interaction is masked by the complexity of the X-band EPR spectrum for OxDC. (16, 17).

Experimental Section

Materials

(Z)-1-(N-methyl-N-[6-(N-methylammoniohexyl)amino]diazen-1-ium-1,2-diolate (MAHMA NONOate) and diethylammonium (Z)-1-(N,N-diethylamino)diazen-1-ium-1,2-diolate (DEA NONOate) were obtained from Cayman Chemical (Ann Arbor, MI). and ¹³C₂-oxalic acid (99%) was purchased from Cambridge Isotope Laboratories (Andover, MA). DNA primers bearing the C383S point mutation, NdE, and BamHI restriction sites were designed and purchased from Integrated DNA Technologies, Inc. (Coraville, IA). DNA sequencing services were done by the core facility of the Interdisciplinary Center for Biotechnology Research (ICBR) at the University of Florida.

His6-tagged Oxalate Decarboxylase Expression and Purification

Protein samples were prepared as described in Chapter 2.

Untagged Recombinant Wild-type and C383S OxDC Mutant

The gene encoding the C383S OxDC mutant was obtained by PCR using the wild-type *B. subtilis* *Yvrk*/pET9a construct as template. A forward primer containing the the NdE1 restriction sequence (5'–GGA GGA AAC ATC ATA TGA AAA AAC AAA ATG–3') was used in tandem with a reverse primer (5'–GCA TCA GGA TCC TTA TTT ACT GCT TTT CTT TTT CAC TAC–3') bearing the cysteine to serine mutation and the BamHI restriction sequence. The resulting amplicon was digested with the NdE1 and BamHI restriction enzymes, giving a DNA fragment with “sticky ends” complementary to similarly digested kanamycin-resistant pET9a vector into which it was ligated using T4 ligase. The resulting C383S plasmid construct was cloned and purified from JM109 *E. coli* using the Promega plasmid purification kit and was submitted for DNA sequencing. Upon confirmation of the desired gene sequence, the C383S OxDC construct was used to transform BL21/DE3 *E. coli* for protein expression. Both of the untagged enzymes were then expressed and purified using a slight modification of published procedures (Appendix A) (18) in which fractions from hydrophobic interaction chromatography on phenyl sepharose were exhaustively dialyzed against a storage buffer of 50 mM Tris buffer, pH 8.5, or 20 mM Hexamethylenetetramine pH 6.0, containing 500 mM NaCl

Membrane Inlet Mass Spectrometry (MIMS)

Description of the instrument and settings are as described in Chapter 2.

Reaction Mixtures

Unless otherwise stated, reaction solutions initially contained either unlabeled 50 mM potassium oxalate or 50mM ¹³C₂-labeled oxalate (99%) dissolved in in 50 mM acetate buffer, pH 4.2, containing 0.2% Triton X-100 and a trace amount of Antifoam A (final volume 2 mL). Because generated NO rapidly gets oxidized in solution, dioxygen

was then depleted in these mixtures by purging with He until MIMS analysis showed baseline levels. In the absence of NO, reactions were initiated by the addition of wild type, His₆-tagged OxDC or the C383S OxDC mutant so that the final enzyme concentrations were 1.4 μ M and 0.43 μ M, respectively.

In experiments examining the ability of NO to inhibit OxDC activity, a solution of either 5 mM MAHMA NONOate (final concentration 50 μ M NO) (46), or 10 mM diethylammonium (*Z*)-1-(N,N-diethylamino) diazen-1-ium-1,2-diolate (final concentration 75 μ M NO) (47, 48), dissolved in 0.01 M aqueous NaOH was injected into the reaction vessel 2 min prior to initiation of the reaction by the addition of enzyme.

Reversibility of NO-dependent OxDC inhibition was investigated, by later addition 50 μ Ls hemoglobin extracted from human blood plasma, or bubbling of either CO₂-scrubbed air (15-30 sec) or pure O₂ (30 sec) into the NO-inhibited enzyme reaction solution.

Continuous Wave EPR Measurements

An aliquot of enzyme stock solution (300 μ L of approx. 0.14 mM enzyme in 50 mM Tris buffer, pH 8.5, containing 500 mM NaCl) was mixed with 2 M potassium acetate buffer, pH 4.1, (18 μ L) to give a final buffer concentration of approximately 110 mM. The small amount of enzyme that precipitated on lowering the solution pH was then removed by centrifugation (14,850 rpm, 5 min) and the resulting clear supernatant was collected (pH 4.5) and employed in subsequent EPR experiments after degassing with argon (care was taken to prevent excessive foaming) for 1 min in an anaerobic chamber (dry box flooded with N₂ gas) under a nitrogen atmosphere. This procedure reduced the solution volume to 240 μ L. An aliquot (120 μ L) of this “stock” enzyme solution was then

transferred to a quartz tube (3 mm internal diameter and 4 mm external diameter), which was capped and rapidly frozen in cold isopentane (pre-cooled to near its freezing point in liquid N₂). The cold sample tube was placed in a pre-cooled cryostat (Oxford ESR900) for CW EPR measurements (Figure 3-11, spectrum (A)). After subsequent thawing of the degassed sample (in the anaerobic chamber), the tube was opened under N₂(g) atmosphere prior to addition of the NO donor. 13 μL of 10 mM degassed MAHMA NONOate in 10 mM aq. NaOH was then added to the enzyme-containing solution in the EPR tube and allowed to react for 5 min before the sample tube was re-capped and rapidly frozen using pre-cooled isopentane. CW EPR measurements were then performed as before (Figure 3-17, spectrum (B)). After thawing, the solution pH of the sample was determined to be 4.6. The remaining degassed “stock” OxDC solution (approximately 120 μL) in 110 mM acetate buffer was then subject to a similar set of procedures as outlined above except that potassium oxalate (14 μL of a 100 mM oxalate solution in acetate buffer, pH 4.1) was added as well as 1 mM MAHMA NONOate prior to cooling and CW EPR measurements (Figure 3-17, spectrum (C)). A “blank” sample was also prepared using 20 mM metal-free Tris buffer, pH 8.5, which was subjected to identical treatment as the NO-exposed solution of OxDC (Figure 3-17, spectrum (D)). Additional control CW EPR spectra were obtained for the 20 mM metal-free Tris buffer, pH 4.1, and a solution of MAHMA NONOate in 10 mM aq. NaOH. These experiments were designed to reveal the potential binding of dissolved NO to those Mn sites which were accessible to X-band EPR analysis through changes in their fine structure values.

All EPR spectra were recorded at liquid helium temperature, using a commercial BrukerElexsys E580 spectrometer with the standard rectangular TE102 resonator. Instrumental parameters were: 90 kHz modulation frequency, 15 G modulation amplitude, 0.6 mW microwave power, 9.4347 GHz microwave frequency, 330 ms time constant, and 330 ms conversion time/point. Each spectrum consisted of a single scan of 5001 data points over a scan range of 50 to 7050 G.

CHAPTER 4 SMALL ANION INHIBITION OF CATALYSIS BY OXDC

Introduction

Discovery and study of enzyme inhibitors are important in elucidating key structures in the catalytic mechanism. For the purpose of exploring medical applications of OxDC, identification of inhibitors become critical in assessing enzymatic behavior outside of its native source or environment.

Reported inhibition of nitric oxide as measured by MIMS had opened a new realm of possibilities in the application of MIMS on the study of OxDC. To date nitric oxide is the only reported inhibitor for *BsOxDC*. Although earlier studies on the fungal OxDC have mentioned effects of compounds such as sodium azide, sulfite and dithionite (37) on catalytic activity, further characterizations on these compounds were limited by the methodologies then. Because of the direct and real-time nature of the MIMS assay, it was now important to employ the method to further investigate the OxDC reaction, in terms of possible product inhibition, and inhibitory effects of molecular analogs of substrate, product and co-factor O₂. Through this method and its ability to utilize isotope-labeled substrate to distinguish catalytic from non-catalytic carbon dioxide in solution, an array of small molecule inhibitors have been examined for *BsOxDC* to an extent that was difficult to achieve with previously published methods.

Results and Discussion

An example of the data provided by MIMS is given in Figure 4-1 for a series of CO₂ progress curves showing inhibition of OxDC by sodium azide at pH 4.2. Initial velocities were determined from the slopes at 5% to 10% of completion and plotted in Figure 4-1 for later discussion under the section on azide.

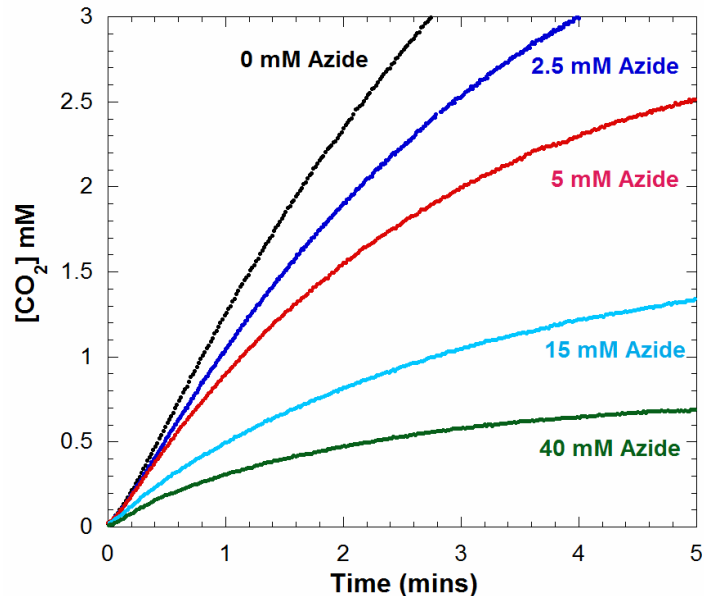


Figure 4-1. Inhibition by azide ions of catalysis by OxDC. Progress curves of accumulated CO₂ in solution from the catalysis of 10 mM oxalate by 0.3 μM OxDC in the presence of (black) 0 mM, (blue) 2.5 mM, (orange) 5 mM, (green) 15 mM, and (red) 40 mM sodium azide in a reaction buffer containing 0.2% Triton X-100 and 100 mM sodium citrate at pH 4.2 and maintained at 25°C.

Catalytic Products

In order to assess the inhibition of products carbon dioxide and formate on catalysis by OxDC, catalytic rates were monitored in reaction buffers pre-equilibrated with 25 - 200 mM sodium formate; or saturating levels of dissolved CO₂ bubbled into solutions containing ¹³C₂-labeled oxalate substrate. Experiments showed that CO₂ itself did not inhibit OxDC as indicated by unaffected rates of catalytic ¹³CO₂ formed in solutions containing saturating levels of dissolved CO₂. Rates of CO₂ formation in the presence of 200 mM formate were reduced by 40% compared with the absence of it, indicating that formate is not a significant inhibitor ($K_i > 200$ mM). These results show that catalysis is not significantly blocked by the buildup of either product in solution.

Utilizing a similar approach, an array of different anions were surveyed for effects on catalysis by monitoring the initial rates of catalytic CO₂ formation by wild type OxDC

in the presence of 10 mM oxalate (near K_m) and 0 - 200 mM anion. Any anion suppressing the rate of CO_2 formation by at least 50% were further surveyed by gathering initial rates at additional intermediate concentrations within the broad 0-100 mM range. A rough preliminary estimate for each K_i was derived by plotting initial rates of CO_2 formation vs. concentration of each anion. Data points were fitted to the equation $v = V_{\max} / (1 + ([I] / [K_i]))$, where “v” is the observed initial rate, “ V_{\max} ” is the initial rate in the absence of inhibitor/anion, and “[I]” is the concentration of surveyed anion.

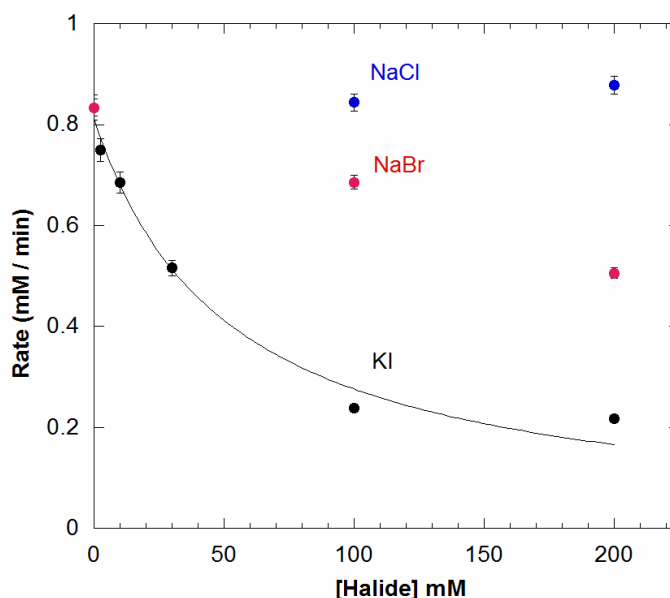


Figure 4-2. Effects of dissolved halides on catalysis by OxDC. Single measurements of initial velocities of generated CO_2 from OxDC catalysis conducted in the presence of 0 mM, 100 mM, 200 mM (blue) NaCl, (red) NaBr; or 2.5 mM, 10 mM, 30 mM, 100 mM, and 200 mM (black) KI dissolved in solution. Reaction mixture also contained 0.2% Triton X-100, 10 mM potassium oxalate, and 100 mM sodium citrate buffered at pH 4.2 and maintained at 25°C. Black curve for (●) represents data fitted to $f(x) = V_{\max} / [1 + ([I] / K_i)]$ with an R^2 value of 0.985. Derived estimated K_i for iodide was 51 ± 7 mM. Error bars indicate the 3% error in deriving the slopes from the linear fitting of the initial 5 - 10% of the respective progress curves of product formation.

A good inhibitor would ideally be one with an estimated K_i which is lower than the K_m of OxDC (4 mM). However, because no inhibitor has ever been characterized for this enzyme prior to nitric oxide, any anion resulting in an estimated K_i of less than 50 mM

were of interest. These anions were further characterized for their mode of inhibition as previously done with NO by varying inhibitor concentration around the estimated K_i and substrate concentrations around the previously observed K_m for oxalate which was at 4 mM.

Anionic Buffer Effects

In order to ensure that any buffer used in the reaction mix did not contribute to any effect observed on catalytic generation of CO_2 , each buffer was first surveyed by running control experiments with wild-type enzyme and 10 mM oxalate in varying buffer concentrations (50 – 200 mM). Among these buffers (acetate, citrate, piperazine) acetate was the only one to show any inhibitory effect at pH 4.2; however, very weak with an estimated $K_i > 100$ mM. Piperazine buffer which was used for reactions at pH 5.4 and pH 6.0 showed no effect on catalytic activity up to 200 mM.

Small anionic halides were also surveyed. Catalysis was not significantly affected by bromide ions up to 100 mM concentrations. Iodide demonstrated some inhibition with K_i near 50 mM (Figure 4-2). In the same figure, chloride ions which are inherent to the storage buffer of the enzyme showed no effect on catalytic activity. Counterions of the anionic salts used in this chapter had no effect on catalysis by OxDC. This was confirmed by unaffected catalytic rates in separate wild-type experiments performed in reaction buffers containing 200 mM sodium chloride, 200 mM potassium chloride, and 200 mM ammonium chloride. Different chloride anionic salts were used upon showing in earlier experiments that chloride had no effect on catalysis.

Phosphate measured at pH 6.0 had a small inhibitory effect on catalysis with K_i near 50 mM. By contrast, sulfate anions measured at pH 4.2 had no effect at all up to a concentration of 200 mM.

Nitrate and Nitrite

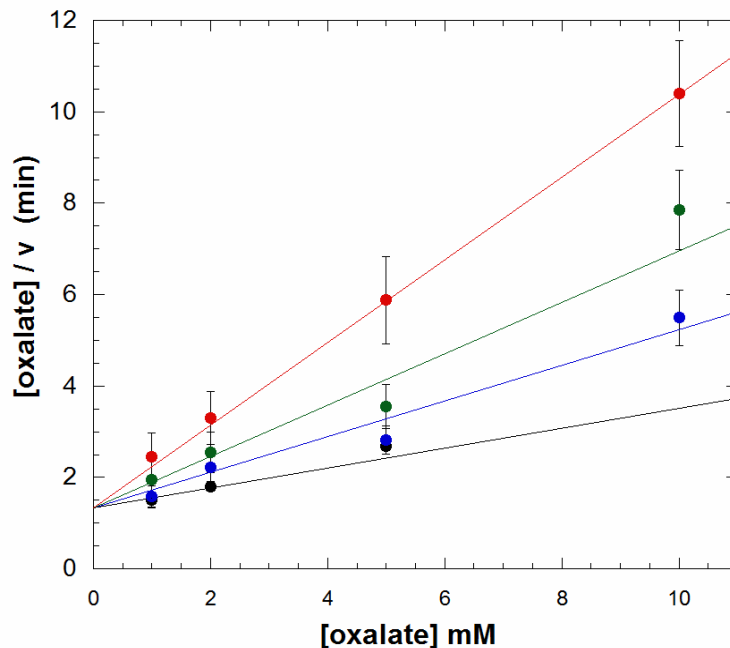


Figure 4-3. Inhibition by nitrite ion (NO_2^-) of catalysis by OxDC. Hanes plot of initial catalytic rates using $1.44 \mu\text{M}$ OxDC in the presence of (black) $0 \mu\text{M}$, (blue) 1 mM , (green) 2 mM , and (red) 4 mM sodium nitrite at pH 4.2. Lines represent data-fitting to an uncompetitive model ($R^2 = 0.967$) using v^4 algorithm with K_i for nitrite estimated at $1.3 \pm 0.2 \text{ mM}$.

Because of the reported dependence of catalysis on the presence of oxygen, effect of oxygen analog nitric oxide on OxDC catalysis was explored in Chapter 3. The reported reversal of NO inhibition by abundant oxygen was presumed to be due to a reaction between supplied O_2 and enzyme-bound NO. This idea was consistent with the reported oxidation of nitric oxide in acidic solution (49). Oxidation products nitrate (NO_3^-) and nitrite (NO_2^-) anions in solution, had different effects on catalysis. Nitrate (from either potassium or ammonium salts) showed no effect on the rate of CO_2 generated by OxDC catalysis up to a concentration of 200 mM . Nitrite by contrast, was inhibitory, with a similar uncompetitive mode of inhibition as NO, but at a weaker magnitude ($K_i \sim 1.3 \text{ mM}$). Nitrite forms very small amounts of NO at acidic pH (estimated to form NO at rates less than 1 nM/sec under the conditions of Figure 4-3 (62). However, levels of NO in

solution, measured by its m/z 30 peak, showed that NO was not involved in this inhibition.

Again, the uncompetitive mode suggests an interaction of nitrite with a species of the enzyme formed after the binding of substrate. From the proposed catalytic scheme in Chapter 1, the nonlinear nitrite anion may be an analog of the formate radical anion intermediate, binding at the formate site in the described structure (Figure 1-5).

Inhibition by nitrite prompted us to look into the surveyed anions not only from the perspective of size, but more importantly, from the perspective of geometry. Which anions were more structurally analogous to substrate, product, or cofactor? And what effects did they have on catalysis? These questions came from the fact that linear NO was significantly inhibitory though it was an uncharged molecule. Nitrite, however similarly anionic as oxalate (substrate) and formate (product), possessed a bent geometry.

Bicarbonate

We studied bicarbonate to estimate inhibition in a separate set of experiments buffered at pH 6.0 to enhance bicarbonate concentration. Experiments showed bicarbonate to be the only competitive inhibitor among the small molecules investigated here, as determined by the parallel lines of Figure 4-4. The entire data set was fit using a competitive model and v^4 weights, and again there was deviation from the competitive model for the largest concentration of bicarbonate (Figure 4-4). The equilibrium between dissolved carbon dioxide and bicarbonate (pKa is 6.35 for the equilibrium $[H^+][HCO_3^-]/[CO_2]$); hence, only a fraction (0.46) all species of CO_2 exists as bicarbonate at the pH 6.0 of this experiment. Taking this into consideration, the K_i for bicarbonate derived from the data of Figure 4-4 is 1.1 ± 0.1 mM.

Bicarbonate at chemical equilibrium exists at about 1% of the concentration of CO_2 in solution at the pH 4.2 used in the experiments in (Figures 4-1, 4-3, and 4-5). As shown in Figure 4-1, we measured concentrations of CO_2 less than 5 mM in these experiments. Bicarbonate formed from this product CO_2 would accumulate to a maximum of 0.05 mM. With the K_i for bicarbonate near 1 mM cited above, we estimate that there is negligible inhibition by bicarbonate affecting our results in Figures 4-1, 4-3, and 4-5.

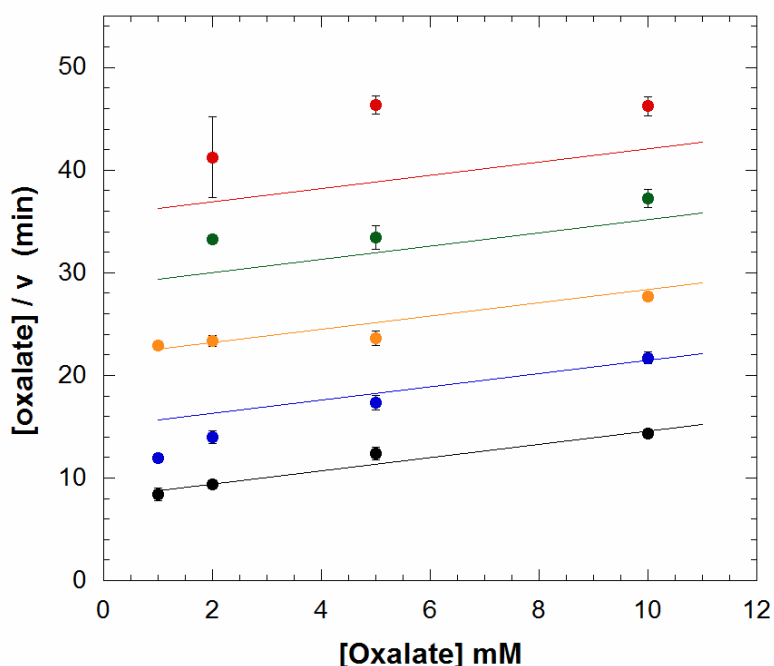


Figure 4-4. Inhibition by bicarbonate of catalysis by OxDC. Hanes plot of initial catalytic rates using 0.6 μM OxDC in the presence of (black) 0 mM, (blue) 2 mM, (orange) 4 mM, (green) 6 mM, and (red) 8mM potassium bicarbonate. Other components were 0.2 Triton X, and 100 mM piperazine at pH 6.0. Solid lines represent the fit of all data to a competitive inhibition model using a v^4 algorithm with K_i for bicarbonate at 1.1 ± 0.1 mM. $R^2 = 0.999$

Bicarbonate caused a competitive inhibition of catalysis with K_i near 1 mM (Figure 4-4). Competitive inhibitors are often associated with substrate analogues, and bicarbonate is only very loosely analogous with the structure of oxalate. Formate and acetate ($K_i > 100$ mM) are better analogs but are very weakly inhibitory. Glycolate, an

even closer analog of oxalate than formate and acetate, is not inhibitory to the enzyme (unpublished data). These features are consistent with the known high specificity of OxDC in catalysis. The competitive inhibition by bicarbonate then emphasizes a possible effect of the third oxygen atom of bicarbonate, which is lacking in formate, acetate, and glycolate. This third oxygen atom may overlap an oxygen atom of the cofactor O_2 in the uninhibited pathway, structure B of Scheme 1 (23). These data raise an interesting possibility that bicarbonate may be a product of the catalysis by OxDC. The half-life for the uncatalyzed conversion of bicarbonate to CO_2 at pH 4 is near 0.1 s so substrate bicarbonate would not be detected in our experiments. None of these mechanisms currently proposed for OxDC suggests bicarbonate as a product (5).

Azide and Thiocyanate

Unlike the observed effects from halides, which were initially perceived to be small enough to access the catalytic site, considerable inhibition was observed from linear anions such as thiocyanate and azide. (Figure 4-1) From these anions, we have observed yet a third mode of inhibition. The data for azide inhibition are best fit to a noncompetitive model as demonstrated by the convergence of lines on the abscissa of the Hanes plot of Figure 4-5. These lines represent a fit of the entire data set of Figure 4-4 to the noncompetitive model using v^4 weighting, as described in the Experimental section (50, 52). It was a feature of several of our inhibitors that the highest inhibitor concentration used did not adhere well to our models. This feature is exaggerated by the emphasis of v^4 weighting on the points representing higher initial velocities and the nature of the Hanes plot containing reciprocal velocities on the ordinate. Nevertheless, this poor fit suggests more complex modes at higher concentrations of these anions, perhaps due to the effect of secondary binding sites. A fit of the data of Figure 4-5 to a

noncompetitive model using v^4 weighting gave $K_i = 14 \pm 9$ mM when we neglected the data at the highest inhibitor concentration. Inhibition by thiocyanate was also determined to be best described as noncompetitive with K_i determined near 4 mM.

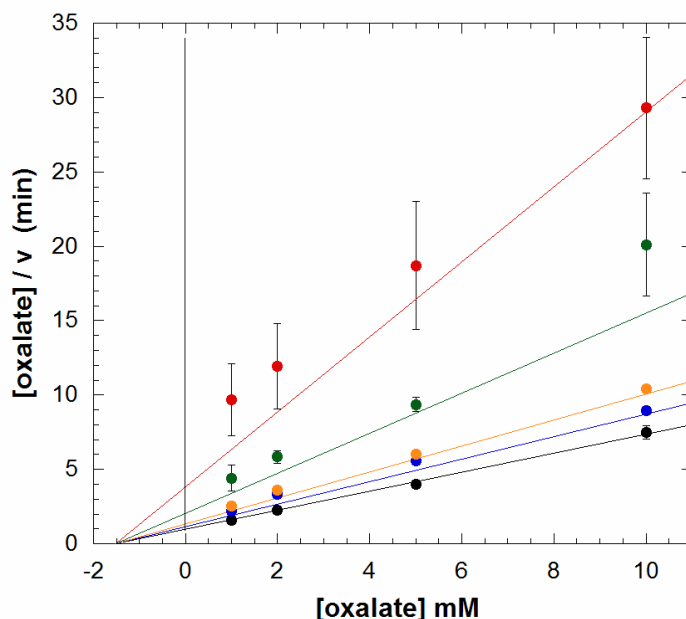


Figure 4-5. Mode of inhibition by azide of catalysis by OxDC. Hanes plot of initial catalytic rates using $1.44 \mu\text{M}$ OxDC in the presence of (black) $0 \mu\text{M}$, (blue) 2.5 mM , (orange) 5 mM , (green) 15 mM , and (red) 40 mM sodium azide at pH 4.2. Solutions were as described in Experimental section. Data points are the least-squares slopes of the initial velocity of single experiments as shown in Figure 4-1. Lines represent a fit of all the data to a noncompetitive inhibition model using a v^4 algorithm with K_i for azide at 14 ± 9 mM.

There are at least two possibilities in explaining the noncompetitive mode: 1) that these anions interact with the enzyme at a location other than that for substrate; 2) or that these anions bind to and inhibit a species of the enzyme that is different from that to which substrate binds. As an example of the latter, the dissociation of product formate may leave the enzyme in an inactive form requiring conformational change or reduction of Mn(III) to become active. The binding of azide to the inactive form would result in a noncompetitive inhibition.

It is interesting that *B. subtilis* OxDC has coordinating amino-acid ligands of the catalytic manganese similar to that of manganese superoxide dismutase (MnSOD) (three histidine residues and a carboxylate of Glu for OxDC (9) and Asp for MnSOD (63). However, MnSOD is characterized predominantly as Mn(III)SOD which as a d^4 ion prefers a pentacoordination; in fact, MnSOD has a single solvent molecule in the inner sphere of coordination (63). In contrast, OxDC is isolated predominantly as Mn(II)OxDC which as a d^5 ion prefers to coordinate a sixth ligand and is characterized as a hexacoordinate with two solvent molecules in the inner sphere (9, 10).

Of the many anions and NO investigated here, only azide has been reported to inhibit MnSOD, binding to Mn(III)SOD in a predominantly outer-sphere complex at room temperature (64, 65). In contrast, substrate analogs such as azide bind directly to the metal in Mn(II)SOD, consistent with the property of the d^5 configuration to bind ligands more tightly to the metal (66, 67). By analogy we may expect azide to bind directly to the manganese of OxDC. The active-site cavity of MnSOD is more sterically constrained than for OxDC (9, 63), which may explain why OxDC is susceptible to inhibition by a wider range of anions. An oxidized metal of Mn(III)OxDC has not been observed in the wild-type. Future EPR experiments have been proposed to investigate whether or not azide binds to the Mn(II) of OxDC. If the inhibitory complex involves azide bound directly to the metal of Mn(II)OxDC displacing the solvent ligand, the resulting noncompetitive inhibition implies that the substrate does not bind directly to the metal. The binding of azide to *E. coli* MnSOD has a binding constant near 7 mM (67), near the value of 14 mM found for OxDC (Figure 4-5). The binding of azide to oxalate

oxidase, which has an active site very similar to OxDC (8), is also in the millimolar range (68).

Experimental Section

His6-tagged Oxalate Decarboxylase Expression and Purification

Protein samples were prepared as described in Chapter 2.

Membrane Inlet Mass Spectrometry (MIMS)

Description of the instrument and settings are as described in Chapter 2.

Reaction Mixtures

Unless otherwise stated, all 2-mL reaction mixtures contained 0.2% Triton X-100, 1 – 10 mM ($^{13}\text{C}_2$ -labeled or unlabeled) potassium oxalate, and 50-100 mM of buffer at pH 4.2 – 6.0. Buffers used were 50 mM acetate or 100 mM citrate for experiments performed at pH 4.2; and 100 mM piperazine for those performed at pH 6.0. Prior to catalysis, reaction mixtures were either equilibrated by the bubbling of CO_2 -free air, or deoxygenated by the bubbling of helium gas. However, catalyses were initiated by the addition of (5 – 20 μL s) air-equilibrated enzyme stocks in order to provide the oxygen that is reported necessary for catalysis (7). Reactions were initiated by the addition of 0.3 – 1.44 μM OxDC and maintained at 25 $^\circ\text{C}$ throughout each experiment by a circulating water bath. Stock solutions of double labeled carbon-13 oxalate ($^{13}\text{C}_2$ -labeled oxalic acid; 99% ^{13}C ; Cambridge Isotope Laboratories - Andover, MA) were prepared by dissolving the pre-weighed solid and adjusting the pH to 4.2 with minimum amounts of KOH.

Anion Inhibition

Unless otherwise noted, the following were tested at pH 4.2 as possible anionic inhibitors from 0.5 – 1.0M stocks: 50 - 200 mM sodium pyruvate, 50 – 200 mM sodium

formate, 100 – 200 mM potassium nitrate, 50 mM ammonium nitrate, 100 – 200 mM sodium sulfate, 5 – 40 mM sodium azide, 50 mM sodium cyanate, 0.75 – 50 mM sodium thiocyanate, 1 – 50 mM sodium bicarbonate (at pH 6.0), 100 – 200 mM sodium chloride, 100 – 200 mM sodium bromide, 2.5 – 200 mM potassium iodide, 20 – 200 mM potassium phosphate (at pH 6.0), 50 - 200 mM sodium citrate, and 50 – 200 mM sodium acetate. Solutions containing these ions, except bicarbonate, were deoxygenated by bubbling of helium prior to each experiment. Experiments using bicarbonate were carried out by the addition of sodium bicarbonate to degassed buffer solutions one minute prior to the initiation of catalysis. Inhibitory effects were detected as reduced rates product formation measured as ion currents for m/z 44 ($^{12}\text{CO}_2$) or m/z 45 ($^{13}\text{CO}_2$) in catalytic mixtures containing varying concentrations substrate and inhibitor.

Initial Rates

Calculations for initial rates of catalysis and associated errors are as described in Chapter 2.

Mode of Inhibition and Statistical Estimation of Parameters

The mode of inhibition and statistical estimation of inhibition constants were determined by a least-squares, best-fit approximation using v^4 weighting factors (50, 52), where v is initial velocity. Data were globally fitted to a kinetic model for simple competitive, simple noncompetitive, and simple uncompetitive inhibition (69) to derive a best-fit estimate of the inhibition constant. In each of the Hanes plots showing inhibition, each data point represents a single measurement of initial velocity. The solid lines on the Hanes plots represent the calculated values of v using the parameters estimated by the least-squares procedures.

CHAPTER 5 CONCLUSIONS AND FUTURE WORK

MIMS and OxDC Catalysis

MIMS provides a direct, continuous, sensitive, and real time assay to monitor decarboxylase activity, yielding results comparable to those acquired from traditional indirect endpoint assays. Importantly, MIMS provides the added feature of simultaneously monitoring other gaseous species providing, for example, a concomitant measure of oxidase activity of OxDC. MIMS measures isotopically labeled products providing a wide flexibility in monitoring effects on reaction catalysis such as addition of inhibitors and changes in reaction conditions. This renders MIMS a versatile tool in studying enzymic catalysis in CO₂ generating reactions

Study of the reversible inhibition of NO as an analogue of dioxygen was a considerable step forward in further understanding OxDC catalysis and assessing the value of the MIMS assay. The ability to narrow down the inhibitory form of NO on OxDC from a range of possibilities was not trivial, considering its limited stability in acidic solution and its potential reactivity with known radical intermediates formed in OxDC catalysis. The interesting uncompetitive mode of inhibition determined through this approach provides useful suggestions on the possible order of binding of substrate and oxygen cofactor, if not conditions in which the putative oxygen pocket is more accessible. Furthermore, it provides more information for optimizations on crystallographic approaches in determining the yet unelucidated Michaelis-Menten complex of OxDC.

An actual look into the suspected product inhibition of OxDC from the perspective of formate and carbon dioxide was a noteworthy achievement delivered by MIMS. The

ability to utilize this method to screen for inhibitors based on structural and size homology with substrate, product and cofactor supports the speculated high specificity of the enzyme. The different modes of inhibition observed here for catalysis by OxDC emphasize the complexity of this catalysis and suggest further experiments to identify inhibition targets and multiple forms of the enzyme required to carry out catalysis. The exact locations of inhibitor binding and enzyme species to which they bind are uncertain at this point. However, the implications of these inhibition studies provide vital ideas in optimizing further crystallographic and spectroscopic experiments investigating the key steps in the mechanism of OxDC.

Insights on Future Work

Findings reported in this work have demonstrated the potential of the MIMS assay on the continued study of OxDC. Optimized experimental conditions in this work have facilitated preliminary work on other aspects of the enzyme; thus laying the groundwork for continued endeavors in better understanding OxDC and its catalytic mechanism.

Michaelis Menten Complex of OxDC

Implications of Chapter 3 on nitric oxide provide a wellspring of information for studying the Michaelis Menten complex of OxDC. Although it is known that oxalate binds to the catalytic site and that dioxygen is required, very little is known on the mode in which substrate binds. Furthermore, it also remains a question as to where the dioxygen cofactor binds and the role it plays in catalysis. Current ideas on the mechanism pictures the Michaelis Menten complex as limited to the N-terminal Mn(II) site. If NO does not directly interact with the N-terminal Mn(II), which is responsible for the unperturbed smaller fine structure in the cw-EPR spectra of NO-inhibited OxDC, then a picture of the Michaelis-menten complex may either include the C-terminal Mn(II)

or a region much wider than the constraints of the N-terminal active site. Since the uncompetitive inhibitors with the lowest K_i s were NO (40 μ M) and its oxidation product anion NO_2^- (2 mM), attempts in crystallizing the MM complex may be facilitated by experimental conditions parallel to the nonaerobic buffer conditions of the MIMS experiments in the presence of oxalate substrate.

Competitive inhibition by bicarbonate ($K_i \sim 1$ mM) albeit at a slightly elevated pH, likewise opens doors for potentially utilizing ^{13}C -labeled bicarbonate and EPR spectroscopy in determining the binding mode of the inhibitor. Although bicarbonate more closely resembles formate product than oxalate substrate, the fact that it targets the same form of the enzyme as oxalate presumably during turnover may give structural insights on the early stages of catalysis.

Oxygen-binding site and Oxygen Dependence

Earlier described experiments on the reversal of nitric oxide inhibition on OxDC by the addition of hemoglobin were vital in showing that molecular NO inhibited the enzyme and not a reaction product/adduct with the enzyme. However, further refinements and additional experiments are necessary to more clearly demonstrate that reversal of inhibition was a result of enzyme-bound NO being “pulled” out by hemoglobin in solution, which is presumed to have a higher affinity for it. Since hemoglobin rapidly oxidizes into its unreactive met-form at acidic pH of 4.2, conducting these experiments using deoxygenated hemoglobin at a slightly higher pH of 5 or 6 may facilitate the opportunity to simultaneously capture a UV spectrum of NO-bound hemoglobin from the reaction vessel, while observing the recovery of catalytic CO_2 from the MIMS instrument. In addition, experiments involving varied concentrations of NO and supplied dioxygen are necessary to unequivocally demonstrate that the time lag

preceding the reversal of NO inhibition by abundant dioxygen is indeed due to an oxidation reaction on enzyme-bound NO rather than simple displacement by O₂.

Overall value of the nitric oxide studies on OxDC is anchored on studying the reported dependence of catalysis on dioxygen and the search for the putative binding pocket for it on the enzyme. Earlier approaches toward these endeavors involved site-directed mutagenesis on OxDC residues, (e.g. Isoleucine-142), hypothesized to define the putative pocket for the dioxygen cofactor. Residues of interest were identified from computer-simulated models of the presumed Michaelis-Menten complex using the enzyme's crystal structure as template. The biggest hurdle in characterizing these enzyme constructs, especially from the perspective of oxygen dependence, was the set of limitations inherent to the FDH endpoint assay. Preliminary kinetic characterization of site-specific OxDC mutants on I142 have so far indicated unperturbed profiles of catalytic effects of oxygen. Continued approaches or refinements of the MIMS method may be employed to characterize other targeted site-specific mutants, or reaction conditions aimed at assessing the oxygen dependence of OxDC.

MIMS and Site-specific Mutants

One of the main roadblocks previously mentioned in kinetically characterizing mutants of OxDC is having a mutant enzyme construct which is neither dead nor active to a considerable magnitude within the detection limits of the FDH endpoint assay. The versatility of MIMS is not limited to the variety of buffer conditions one may perform with the method. The range of sensitivity of the instrument can be set in detecting even minute amounts of CO₂ generated in solution. This vital feature revives the potential of earlier approaches in studying OxDC through site-directed mutagenesis, rendering

MIMS as a powerful tool in kinetically characterizing weakly active mutants demonstrating roles of other vital conserved residues.

Effect of Periodate and bisulfite anions

Preliminary characterization by MIMS, of anions with oxidizing and reducing properties, have shown considerable magnitudes of inhibition with approximated K_i s in the low millimolar range. However an interesting feature in these experiments was an apparently transient enhancement in catalytic generation of CO_2 prior to inhibition at high concentrations of inhibitor versus substrate. From these experiments one may speculate that the anion may be oxidizing/reducing the catalytic Manganese to a state that is favorable for one step of catalysis, but rendering the enzyme unable to turnover. This may not be surprising since other manganese-containing enzymes such as oxalate oxidase and Mn-SOD, rely on a continuous toggle between two oxidation states of manganese (Mn^{2+} and Mn^{3+}) throughout their catalytic cycles. There has so far been no evidence for Mn^{3+} in catalysis by wild-type OxDC, although one cannot rule out the possibility of a rapidly transient (and yet undetected) existence of it during turnover.

One may also argue that strong oxidizing agents may oxidize unreacted substrate and thus create artifactual generation of detected carbon dioxide. Regardless, it would be interesting to know whether anions capable of redox chemistry can be instrumental in uncovering more information on the chemistry of the catalytic manganese of OxDC.

Predictions on inhibitory molecules for OxDC have been patterned after precedents reported on other manganese-containing enzymes of analogous metal environments in their catalytic sites. How the chemistry of these enzymes relate to one another remains a broad question motivating ongoing work in this project.

APPENDIX A
EXPRESSION AND PURIFICATION OF BACILLUS SUBTILIS OXDC

Comparative table of expression and purification schemes for untagged and polyhistidine-tagged *B. subtilis* oxalate decarboxylase in BL21 (DE3) *E. coli* cells (10, 14, 18).

	Untagged <i>Bs</i> OxDC	C-terminally His₆-tagged <i>Bs</i> OxDC
	Yvrk gene/pET 9a plasmid construct	Yvrk gene/pET 32a plasmid construct
EXPRESSION:		
	Overnight cultures grown in 50mL LB with 50µg Kanamycin	Overnight cultures grown in 50mL LB with 100µg Ampicillin
Reinoculation of overnight cultures in:	3-Liters of LB and grown at 37°C until Induction OD ₆₀₀ = 0.6	1-L of LB at 37°C and grown until Induction OD ₆₀₀ = 0.3
	Heat Shock at 42°C for 10mins	Heat Shock at 42°C for 18mins
	Addition of: 1mM isopropyl-β-D-thiogalactopyranoside 5mM Manganese Chloride	
	Grow for 4 hours at 30°C	Grow for 4 hours at 37°C
	Harvest cells and Lyse by Sonication (70% Amplitude)	
	Overnight Extraction in : 50mM Imidazole-Cl pH 7.0 1.0M NaCl 0.1% Triton X-100 10mM 2-mercaptoethanol	↓
PURIFICATION:	Removal of cell debris by centrifugation	
COLUMN 1	DEAE Sepharose (Anion Exchange)	Nickel (Ni-NTA) Affinity column
	Salting in 1.7M Ammonium Sulfate to precipitate out unwanted proteins	↓
COLUMN 2	Phenyl Sepharose (HIC)	
	Concentrate eluted fraction pool and dialyze overnight into Storage buffer: 20mM Hexamethylenetetramine-Cl 500mM NaCl pH 6.0	Buffer exchange eluted fraction pool into Storage buffer: 50mM Tris-Cl 500mM NaCl pH 8.5
Removal of adventitious metals	Buffer exchange into Chelex-100 (BioRad) treated "metal-free" storage buffer	Treat buffer-exchanged protein solution with Chelex-100 (BioRad) resin
	Concentrate metal-free protein solution to 7-8mg/mL via YM-30 Centriprep (Millipore)	

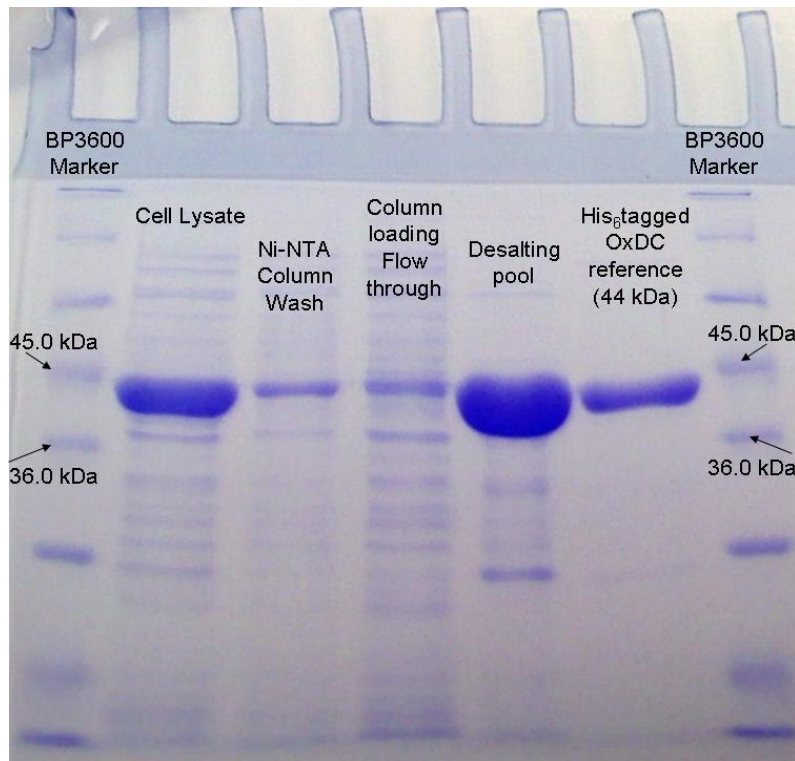


Figure A-1. 12% SDS PAGE gel of fractions from the expression and purification of C-terminally His₆-tagged wild-type *BsOxDC*.

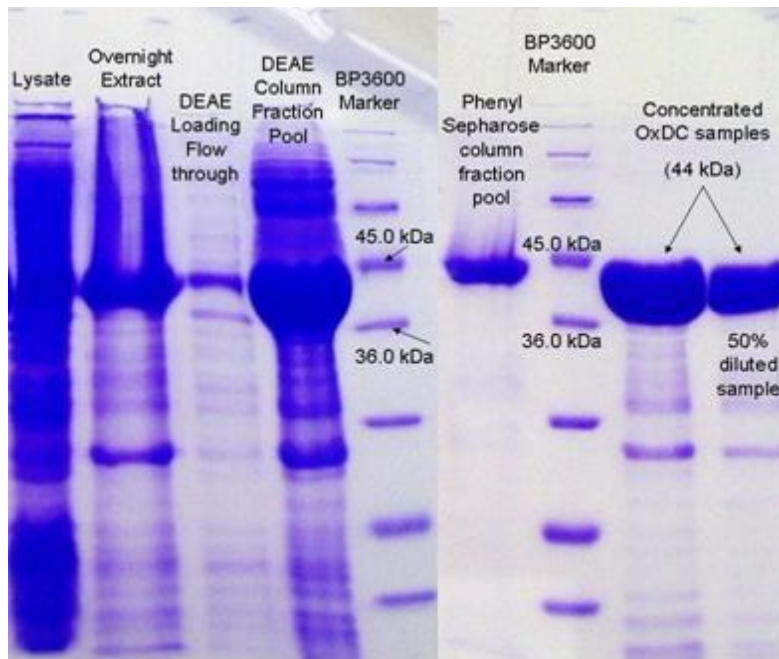


Figure A-2. 12% SDS PAGE gel of fractions from the expression and purification of untagged wild-type *BsOxDC*.

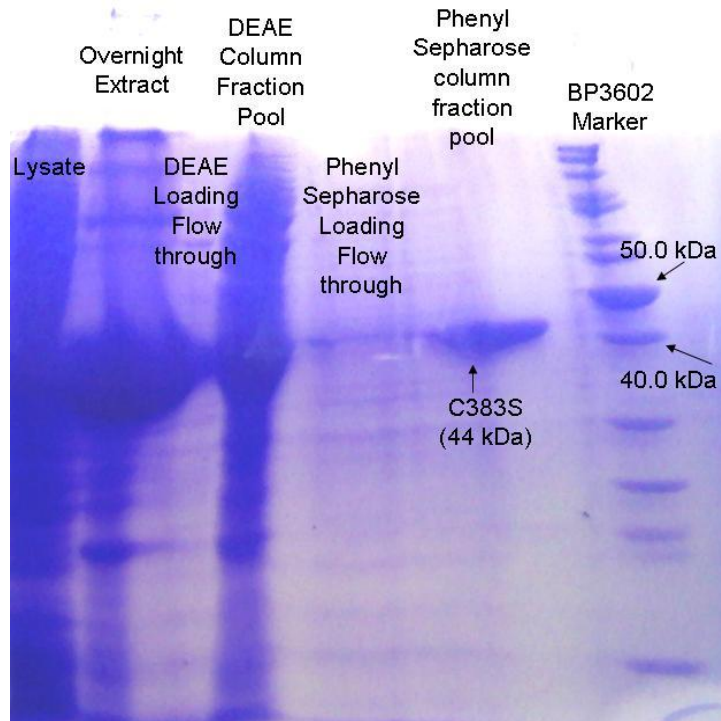


Figure A-3. 12% SDS PAGE gel of fractions from the expression and purification of untagged C383S *BsOxDC* mutant.


```

B.subtilis_OxDC -----
B.amyloliquefaciens_OxDC -----
A.niger_OxDC --MQLTLPPRQLLLSFATVA-----ALLDPSHGGVPVNEAYQQLLQIPA- 42
C.subvermispora_OxOx MNEKLVSVFCAILVAISVSARPTGNDVFYLPRAVAVSSAGASSPASLSSG 50

B.subtilis_OxDC -----MKK-----QNDIPQPIRGDKGATVKIP 22
B.amyloliquefaciens_OxDC -----MKKLIQQLASKHLPPQPIRGRKGATDEGP 28
A.niger_OxDC ---SSPSIFFQDKPFTPDHRDPYDHKVDAIGEGHEPLPWRMGDGTIMGP 89
C.subvermispora_OxOx TESSAAEPTETVPFASDDPNRLWNIDT-QDLSVVAPERGPLGAKIIGP 99
. * * * * *

B.subtilis_OxDC RNIERDRQNPDMLVPPETDHGTVSNMKFSFSDTHNRLEKGGYAREVTVRE 72
B.amyloliquefaciens_OxDC RNLARDFQNPDMLVPPSTDAGTVQNLKFSFSDTHMRLEDGGWSREVTVRE 78
A.niger_OxDC RNKDREQRQNPDMLRPSTDHGNMPPNRWSFADSHIRIEEGGWTRQTTVRE 139
C.subvermispora_OxOx DNLPLDIQNADTLAPPTTDSGSI PNAKWPFA LSHTLYTGGWVRIQNNEV 149
* : *. * * * * * . : * : : * : * : * : * . .

B.subtilis_OxDC LPISENLASVNMRLKPGAIRELHWHKEAEWAYMIYGSARVTIVDEKGRSF 122
B.amyloliquefaciens_OxDC LPVSKNIAAVNMRLKPGAVRELHWHKEAEWGYVINGGVRLTAVDQNGRNF 128
A.niger_OxDC LPTSKELAGVNMRLDEGVIRELHWHREAEWAYVLAGRVVVTGLDLEGGSF 189
C.subvermispora_OxOx LPIAKAMAGVNMRL EAGTIRELHWHNTPEWAYI LKGTQTITAVDENGKNY 199
** : : : * . * * * * . * . : * * * * . . * : : * : * : * :

B.subtilis_OxDC IDDVGEGLDWYFPSGLPHSIQALE---EGAEFLLVFDGGSFSENSTFQLT 169
B.amyloliquefaciens_OxDC IDNVSEGLDWYFPSGIPHSIQGLE---QGSEFLLVFDGGSFSENSTFSVT 175
A.niger_OxDC IDDLLEGLDWYFPSGHPHSLQGLSP--NGTEFLLIFDDGNFSEESTFLLT 237
C.subvermispora_OxOx LANVGPGLDWYFPEGMPHSLQGTNASDEGSEFLLIFPDGTFDASNQFMIT 249
: : : * * * * * . * * * * : . : * : * * * * . . * : *

B.subtilis_OxDC DWLAHTPKEVIAANFGVTKEEISNLPGKEYIFENQLPGSLKDDIVEGPN 219
B.amyloliquefaciens_OxDC DWFAHTPRSVLEANFGVSGYDLAYIHKKERYMFQLEPPPPPIERA AVSSPE 225
A.niger_OxDC DWIAHTPKSVLAGNFRMRPQTFKNI PPSEKYIFQGSVPDSIPKELPRNFK 287
C.subvermispora_OxOx DWLAHTPKDVI AKNFGVDISEFDRLP SHDLYIFPGVAP-PLDATAPEDPQ 298
** : * * * * : * : : : * : * * * * . : :

B.subtilis_OxDC GEVYPYFTYRLLQEPIESEGGKVYIADSTNFKVSKTIASALVTVEPGAM 269
B.amyloliquefaciens_OxDC GTVLEPFYSYKLSRQEPLVTSGGRVKIVDSKTFKVSKTIAAALVEVEPGGM 275
A.niger_OxDC ASKQR-FTHKMLAQEPEHTSGGEVRITDSSNFPISKTVAAAHLTINPGAI 336
C.subvermispora_OxOx GTIPLPYSFEFSKVVPTQYAGGTVKIADTRTFPISKTISVAEITVEPGAM 348
. : : : : * * * * * . * : * * * * : * : : * * :

B.subtilis_OxDC RELHWHPNTHEWQYYISGKARMTVFASDGHARTFNYQAGDVGYVVPFAMGH 319
B.amyloliquefaciens_OxDC RELHWHPNNTDEWQYYLSGEAKMTVFAAEGRARTFNYQASDVGYVPIAMGH 325
A.niger_OxDC REMHWHPNADEWSYFKRGRARVTIFAAEGNARTFDYVAGDVGIVPRNMGH 386
C.subvermispora_OxOx RELHWHPTEDEWTFEIEGQARVTLFAGESNAQTYDYQGGDIAYIPTAYGH 398
** : * * * * . * * : : * . * : : * * . . * : : * *

B.subtilis_OxDC YVENIGD-EPLVFLEIFKDDHYADVSLNQWLAMLPETFVQAHLDLG-KDF 367
B.amyloliquefaciens_OxDC YVQNTGD-TVLRFLFIFKSDRFEDVSLNQWLALTPQRFVEQTLNVS-PAF 373
A.niger_OxDC FIENLSDDEEVEVLEIFRADRFDFSLFQWMGETPQRMVAEHVFKDDPDA 436
C.subvermispora_OxOx YVENSNGN-TTLRFLFIFNSPLFQDVSLTQWLANTPRAIVKATLQLS-DNV 446
: : * : : : * * * * . : * . * * * * . * : * :

B.subtilis_OxDC TDVLSKEKHPVVKKCKSK--- 385
B.amyloliquefaciens_OxDC ARRLKSKKSPVVKWKHKQ--- 391
A.niger_OxDC AREFLKSVESGEKDP IRSPSE 457
C.subvermispora_OxOx IDSLNKS KAFVVASD----- 461
: * .

```

Figure B-2. Amino acid sequence alignment of bacterial and fungal OxDC with the (blue) bicupin oxalate oxidase (OxOx) from yeast. Alignment was created using ClustalW 2.1 (<http://www.ebi.ac.uk/Tools/msa/clustalw2/>).

(A)

```
1 MKKQNDIPQP IRGDKGATVK IPRNIERDRQ NPDMLVPPET DHGTVSNMKF SFSDTHNRLE
61 KGGYAREVTV RELPISENLA SVNMRLKPGA IRELHWHKEA EWAYMIYGSA RVTIVDEKGR
121 SFIDDVGEED LWYFPSGLPH SIQALEEGAE FLLVFDDGSF SENSTFQLTD WLAHTPKEVI
181 AANFGVTKEE ISNLPGKEKY IFENQLPGSL KDDIVEGPNG EVPYPFTYRL LEQEPIESEG
241 GKVYIADSTN FKVSKTIASA LVTVEPGAMR ELHWHPNTHE WQYYISGKAR MTVFASDGHA
301 RTFNYQAGDV GYVPFAMGHY VENIGDEPLV FLEIFKDDHY ADVSLNQWLA MLPETFVQAH
361 LDLGKDFTDV LSKEKHPVVK KKCSK
```

(B)

```
1 atgaaaaaac aaaatgacat tccgcagcca attagaggag acaaaggagc aacggtaaaa
61 atccccgcgca atattgaaag agaccggcaa aaccctgata tgctcgttcc gcctgaaacc
121 gatcatggca ccgtcagcaa tatgaagttt tcattctctg atactcataa ccgattagaa
181 aaaggcggat atgcccggga agtgacagta cgtgaattgc cgatttcaga aaaccttgca
241 tccgtaaata tgcggctgaa gccagggcgcg attcgcgagc ttcactggca taaagaagct
301 gaatgggctt atatgattta cgggaagtgc agagtcacaa ttgtagatga aaaagggcgc
361 agcttttattg acgatgtagg tgaaggagac ctttgggtact tcccgtcagg cctgcccgcac
421 tccatccaag cgctggagga gggagctgag tcctgctcg tgtttgacga tggatcattc
481 tctgaaaaca gcacgttcca gctgacagat tggctggccc aactccaaa agaagtcatt
541 gctgcgaact tcggcgtgac aaaagaagag atttccaatt tgcctggcaa agaaaaatat
601 atatttgaia accaacttcc tggcagttta aaagatgata ttgtggaagg gccgaatggc
661 gaagtgcctt atccatttac ttaccgcctt cttgaacaag agccgatcga atctgagggg
721 ggaaaagtat acattgcaga ttcgacaaac ttcaaagtgt ctaaaacat cgcatcagcg
781 ctcgtaacag tagaaccggg cgccatgaga gaactgcact ggcacccgaa taccacgaa
841 tggcaatact acatctccgg taaagctaga atgaccgttt ttgcatctga cggccatgcc
901 agaacgttta attaccaagc cggatgatgc ggatgatgac catttgcaat gggtcattac
961 gttgaaaaca tcggggatga accgcttgtc tttttagaaa tcttcaaaga cgaccattat
1021 gctgatgtat ctttaaacca atggcttgcc atgcttcctg aacatctgt tcaagcgcac
1081 cttgacttgg gcaaagactt tactgatgtg ctttcaaaag aaaagcacc agtagtgaaa
1141 aagaaatgca gtaataaa
```

Figure B-3. (A) amino acid and (B) *yvrk* gene sequences of oxalate decarboxylase from *B. subtilis*. Highlighted residue in red (C383) is the only cysteine in the amino acid sequence.

LIST OF REFERENCES

1. Emiliani, E., and Bekes, P. (1964) Enzymatic Oxalate Decarboxylation in *Aspergillus Niger*, *Arch Biochem Biophys* 105, 488-493.
2. Shimazono, H. (1955) Oxalic Acid Decarboxylase, a New Enzyme from the Mycelium of Wood Destroying Fungi, *J Biochem-Tokyo* 42, 321-340.
3. Tanner, A., and Bornemann, S. (2000) *Bacillus subtilis* YvrK is an acid-induced oxalate decarboxylase, *J Bacteriol* 182, 5271-5273.
4. Jonsson, S., Svedruzic, D., Wroclawska, E., Chang, C. H., and Richards, N. G. J. (2003) Structure and mechanism of enzymes mediating oxalate metabolism., *Biochemistry* 42, 8617-8617.
5. Svedruzic, D., Jonsson, S., Toyota, C. G., Reinhardt, L. A., Ricagno, S., Lindqvist, Y., and Richards, N. G. J. (2005) The enzymes of oxalate metabolism: unexpected structures and mechanisms, *Arch Biochem Biophys* 433, 176-192.
6. Lane, B. G. (1994) Oxalate, germin, and the extracellular matrix of higher plants, *FASEB J* 8, 294-301.
7. Tanner, A., Bowater, L., Fairhurst, S. A., and Bornemann, S. (2001) Oxalate decarboxylase requires manganese and dioxygen for activity - Overexpression and characterization of *Bacillus subtilis* YvrK and YoaN, *J Biol Chem* 276, 43627-43634.
8. Woo, E. J., Dunwell, J. M., Goodenough, P. W., Marvier, A. C., and Pickersgill, R. W. (2000) Germin is a manganese containing homohexamer with oxalate oxidase and superoxide dismutase activities, *Nature Structural Biology* 7, 1036-1040.
9. Anand, R., Dorrestein, P. C., Kinsland, C., Begley, T. P., and Ealick, S. E. (2002) Structure of oxalate decarboxylase from *Bacillus subtilis* at 1.75 angstrom resolution, *Biochem* 41, 7659-7669.
10. Just, V. J., Stevenson, C. E., Bowater, L., Tanner, A., Lawson, D. M., and Bornemann, S. (2004) A closed conformation of *Bacillus subtilis* oxalate decarboxylase OxdC provides evidence for the true identity of the active site, *J Biol Chem* 279, 19867-19874.
11. Dunwell, J. M. (1998) Cupins: a new superfamily of functionally diverse proteins that include germins and plant storage proteins, *Biotechnol Genet Eng Rev* 15, 1-32.
12. Dunwell, J. M., Culham, A., Carter, C. E., Sosa-Aguirre, C. R., and Goodenough, P. W. (2001) Evolution of functional diversity in the cupin superfamily, *Trends Biochem Sci* 26, 740-746.

13. Dunwell, J. M., Purvis, A., and Khuri, S. (2004) Cupins: the most functionally diverse protein superfamily?, *Phytochemistry* 65, 7-17.
14. Burrell, M. R., Just, V. J., Bowater, L., Fairhurst, S. A., Requena, L., Lawson, D. M., and Bornemann, S. (2007) Oxalate decarboxylase and oxalate oxidase activities can be interchanged with a specificity switch of up to 282,000 by mutating an active site lid, *Biochemistry* 46, 12327-12336.
15. Just, V. J., Burrell, M. R., Bowater, L., McRobbie, I., Stevenson, C. E., Lawson, D. M., and Bornemann, S. (2007) The identity of the active site of oxalate decarboxylase and the importance of the stability of active-site lid conformations, *Biochem J* 407, 397-406.
16. Tabares, L. C., Gatjens, J., Hureau, C., Burrell, M. R., Bowater, L., Pecoraro, V. L., Bornemann, S., and Un, S. (2009) pH-dependent structures of the manganese binding sites in oxalate decarboxylase as revealed by high-field electron paramagnetic resonance, *J Phys Chem B* 113, 9016-9025.
17. Angerhofer, A., Moomaw, E. W., Garcia-Rubio, I., Ozarowski, A., Krzystek, J., Weber, R. T., and Richards, N. G. (2007) Multifrequency EPR studies on the Mn(II) centers of oxalate decarboxylase, *J Phys Chem B* 111, 5043-5046.
18. Moomaw, E. W., Angerhofer, A., Moussatche, P., Ozarowski, A., Garcia-Rubio, I., and Richards, N. G. (2009) Metal dependence of oxalate decarboxylase activity, *Biochemistry* 48, 6116-6125.
19. Dunwell, J. M., and Gane, P. J. (1998) Microbial relatives of seed storage proteins: conservation of motifs in a functionally diverse superfamily of enzymes, *J Mol Evol* 46, 147-154.
20. Khuri, S., Bakker, F. T., and Dunwell, J. M. (2001) Phylogeny, function, and evolution of the cupins, a structurally conserved, functionally diverse superfamily of proteins, *Mol Biol Evol* 18, 593-605.
21. Svedruzic, D., Liu, Y., Reinhardt, L. A., Wroclawska, E., Cleland, W. W., and Richards, N. G. (2007) Investigating the roles of putative active site residues in the oxalate decarboxylase from *Bacillus subtilis*, *Arch Biochem Biophys* 464, 36-47.
22. Chang, C. H., Richards, N. G. J. (2005) Intrinsic carbon-carbon bond reactivity at the manganese center of oxalate decarboxylase from density theory, *J. Chem. Theory Comput.* 1, 994-1007.
23. Reinhardt, L. A., Svedruzic, D., Chang, C. H., Cleland, W. W., and Richards, N. G. (2003) Heavy atom isotope effects on the reaction catalyzed by the oxalate decarboxylase from *Bacillus subtilis*, *J Am Chem Soc* 125, 1244-1252.

24. Imaram, W., Saylor, B. T., Centonze, C. P., Richards, N. G. J., and Angerhofer, A. (2011) EPR spin trapping of an oxalate-derived free radical in the oxalate decarboxylase reaction, *Free Radical Biol. Med.* 50, 1009-1015.
25. Magro, P., Marciano, P., and Dilenna, P. (1988) Enzymatic Oxalate Decarboxylation in Isolates of Sclerotinia-Sclerotiorum, *Fems Microbiology Letters* 49, 49-52.
26. Schute, H., Flossdorf, J., Sahm, H., and Kula, M. R. (1976) Purification and properties of formaldehyde dehydrogenase and formate dehydrogenase from *Candida boidinii*, *European Journal of Biochemistry* 62, 151-160.
27. Muthusamy, M., Burrell, M. R., Thorneley, R. N., and Bornemann, S. (2006) Real-time monitoring of the oxalate decarboxylase reaction and probing hydron exchange in the product, formate, using fourier transform infrared spectroscopy, *Biochemistry* 45, 10667-10673.
28. Gross, J. H. (2006) *Mass spectrometry : a textbook*, 1st ed., Springer, New York.
29. Kortz, L., Helmschrodt, C., and Ceglarek, U. (2011) Fast liquid chromatography combined with mass spectrometry for the analysis of metabolites and proteins in human body fluids, *Anal. Bioanal. Chem.* 399, 2635-2644.
30. Matros, A., Kaspar, S., Witzel, K., and Mock, H. P. (2011) Recent progress in liquid chromatography-based separation and label-free quantitative plant proteomics, *Phytochemistry (Elsevier)* 72, 963-974.
31. Hoch, G., and Kok, B. (1963) A mass spectrometer inlet system for sampling gases dissolved in liquid phases, *Arch Biochem Biophys* 101, 160-170.
32. Itada, N., and Forster, R. E. (1977) Carbonic anhydrase activity in intact red blood cells measured with ¹⁸O exchange, *J Biol Chem* 252, 3881-3890.
33. Tu, C., Wynns, G. C., McMurray, R. E., and Silverman, D. N. (1978) CO₂ kinetics in red cell suspensions measured by ¹⁸O exchange, *J Biol Chem* 253, 8178-8184.
34. Brodbelt, J. S., Cooks, R. G., Tou, J. C., Kallos, G. J., and Dryzga, M. D. (1987) In vivo mass spectrometric determination of organic compounds in blood with a membrane probe, *Anal Chem* 59, 454-458.
35. Silverman, D. N. (1982) Carbonic anhydrase: oxygen-18 exchange catalyzed by an enzyme with rate-contributing proton-transfer steps, *Methods Enzymol* 87, 732-752.
36. Moral, M. E. G., Tu, C., Richards, N. G. J., and Silverman, D. N. (2011) Membrane inlet for mass spectrometric measurement of catalysis by enzymatic decarboxylases, *Anal. Biochem.* 418, 73-77.

37. Emiliani, E., and Riera, B. (1968) Enzymatic Oxalate Decarboxylation in *Aspergillus Niger*. 2. Hydrogen Peroxide Formation and Other Characteristics of Oxalate Decarboxylase, *Biochimica Et Biophysica Acta* 167, 414-&.
38. Delieu, T., and Walker, D. A. (1972) Improved Cathode for Measurement of Photosynthetic Oxygen Evolution by Isolated Chloroplasts, *New Phytologist* 71, 201-225.
39. Patil, P. V., and Ballou, D. P. (2000) The use of protocatechuate dioxygenase for maintaining anaerobic conditions in biochemical experiments, *Analytical Biochemistry* 286, 187-192.
40. Lehninger, A. L., Nelson, D. L., and Cox, M. M. (2000) *Lehninger principles of biochemistry*, 3rd ed., Worth Publishers, New York.
41. Cornish-Bowden, A. (1979) *Fundamentals of enzyme kinetics*, Butterworths, London ; Boston.
42. Olivares, J. A. (1988) Inductively-coupled plasma mass spectrometry, *Methods Enzymol* 158, 205-232.
43. Shimazono, H., and Hayaishi, O. (1957) Enzymatic decarboxylation of oxalic acid, *J Biol Chem* 227, 151-159.
44. Tu, C., Swenson, E. R., and Silverman, D. N. (2007) Membrane inlet for mass spectrometric measurement of nitric oxide, *Free Radic Biol Med* 43, 1453-1457.
45. Mikulski, R., Tu, C., Swenson, E. R., and Silverman, D. N. (2010) Reactions of nitrite in erythrocyte suspensions measured by membrane inlet mass spectrometry, *Free Radic Biol Med* 48, 325-331.
46. Hrabie, J. A., Klose, J. R., Wink, D. A., and Keefer, L. K. (1993) New Nitric Oxide-Releasing Zwitterions Derived from Polyamines, *Journal of Organic Chemistry* 58, 1472-1476.
47. Keefer, L. K., Nims, R. W., Davies, K. M., and Wink, D. A. (1996) "NONOates" (1-substituted diazen-1-ium-1,2-diolates) as nitric oxide donors: convenient nitric oxide dosage forms, *Methods Enzymol* 268, 281-293.
48. Maragos, C. M., Morley, D., Wink, D. A., Dunams, T. M., Saavedra, J. E., Hoffman, A., Bove, A. A., Isaac, L., Hrabie, J. A., and Keefer, L. K. (1991) Complexes of .NO with nucleophiles as agents for the controlled biological release of nitric oxide. Vasorelaxant effects, *J Med Chem* 34, 3242-3247.
49. Hughes, M. N. (2008) Chemistry of nitric oxide and related species, *Methods Enzymol.* 436, 3-19.

50. Cleland, W. W. (1979) Statistical analysis of enzyme kinetic data, *Methods Enzymol* 62, 151-160.
51. Wilkinson, G. N. (1961) Statistical estimations in enzyme kinetics, *Biochem. J.* 80, 324-332.
52. Cleland, W. W. (1967) Statistical analysis of enzyme kinetic data, *Adv. Enzymol. Relat. Subj. Biochem.* 29, 1-32.
53. Copeland, R. A. (2005) *Evaluation of enzyme inhibitors in drug discovery : a guide for medicinal chemists and pharmacologists*, Wiley-Interscience, Hoboken, N.J.
54. Moral, M. E. G., Tu, C. K., Imaram, W., Angerhofer, A., Silverman, D. N., and Richards, N. G. J. (2011) Nitric oxide reversibly inhibits *Bacillus subtilis* oxalate decarboxylase, *Chemical Communications* 47, 3111-3113.
55. Koppenol, W. H. (1998) The basic chemistry of nitrogen monoxide and peroxyxynitrite, *Free Radic Biol Med* 25, 385-391.
56. Hess, D. T., Matsumoto, A., Kim, S. O., Marshall, H. E., and Stamler, J. S. (2005) Protein S-nitrosylation: purview and parameters, *Nat Rev Mol Cell Biol* 6, 150-166.
57. Reed, G. H., and Markham, G. D. (1984) EPR of Mn(II) Complexes with Enzymes and Other Proteins, in *Biological Magnetic Resonance* (Berliner, L. J., and Reuben, J., Ed.), pp 73-142, Plenum Press, New York.
58. Hoffman-Luca, C. G., Eroy-Reveles, A. A., Alvarenga, J., and Mascharak, P. K. (2009) Syntheses, structures, and photochemistry of manganese nitrosyls derived from designed Schiff base ligands: potential NO donors that can be activated by near-infrared light, *Inorg Chem* 48, 9104-9111.
59. Eroy-Reveles, A. A., Leung, Y., Beavers, C. M., Olmstead, M. M., and Mascharak, P. K. (2008) Near-infrared light activated release of nitric oxide from designed photoactive manganese nitrosyls: strategy, design, and potential as NO donors, *J Am Chem Soc* 130, 4447-4458.
60. Ford, P. C., Fernandez, B. O., and Lim, M. D. (2005) Mechanisms of reductive nitrosylation in iron and copper models relevant to biological systems, *Chem Rev* 105, 2439-2455.
61. Chang, C. H., Svedruzic, D., Ozarowski, A., Walker, L., Yeagle, G., Britt, R. D., Angerhofer, A., and Richards, N. G. (2004) EPR spectroscopic characterization of the manganese center and a free radical in the oxalate decarboxylase reaction: identification of a tyrosyl radical during turnover, *J Biol Chem* 279, 52840-52849.

62. Samouilov, A., Kuppusamy, P., and Zweier, J. L. (1998) Evaluation of the magnitude and rate of nitric oxide production from nitrite in biological systems, *Archives of Biochemistry and Biophysics* 357, 1-7.
63. Borgstahl, G. E., Parge, H. E., Hickey, M. J., Beyer, W. F., Jr., Hallewell, R. A., and Tainer, J. A. (1992) The structure of human mitochondrial manganese superoxide dismutase reveals a novel tetrameric interface of two 4-helix bundles, *Cell* 71, 107-118.
64. Lah, M. S., Dixon, M. M., Patridge, K. A., Stallings, W. C., Fee, J. A., and Ludwig, M. L. (1995) Structure-function in *Escherichia coli* iron superoxide dismutase: Comparisons with the manganese enzyme from *Thermus thermophilus*, *Biochemistry* 34, 1646-1660.
65. Miller, A.-F., Padmakumar, K., Sorkin, D. L., Karapetian, A., and Vance, C. K. (2003) Proton-coupled electron transfer in Fe-superoxide dismutase and Mn-superoxide dismutase, *J. Inorg. Biochem.* 93, 71-83.
66. Jackson, T. A., Karapetian, A., Miller, A.-F., and Brunold, T. C. (2005) Probing the Geometric and Electronic Structures of the Low-Temperature Azide Adduct and the Product-Inhibited Form of Oxidized Manganese Superoxide Dismutase, *Biochemistry* 44, 1504-1520.
67. Whittaker, J. W., and Whittaker, M. M. (1991) Active-Site Spectral Studies on Manganese Superoxide-Dismutase, *Journal of the American Chemical Society* 113, 5528-5540.
68. Satyapal, and Pundir, C. S. (1993) Purification and properties of an oxalate oxidase from leaves of grain sorghum hybrid CSH-5, *Biochimica Et Biophysica Acta* 1161, 1-5.
69. Purich, D. L. (2010) *Enzyme Kinetics Catalysis and Control : A Reference of Theory and Best-Practice methods*, Elsevier, Amsterdam.

BIOGRAPHICAL SKETCH

Mario Moral was born in Naples, Italy in 1971. He received his BS Chemistry degree in the Philippines in 1994 from the Ateneo de Manila University, where he was immediately invited to teach for the Department of Chemistry. In 1997 he entered the religious order of the Society of Jesus and left the congregation upon completion of his novitiate formation. He worked for the Philippine Institute of Pure and Applied Chemistry (PIPAC) in collaborative projects with the Philippine government's Food and Nutrition Research Institute while doing graduate coursework in molecular biology and biochemistry under the Department of Chemistry at the University of the Philippines in Diliman. Mario started graduate studies in the Department of Chemistry at the University of Florida in 2006, where he joined the research group of Nigel G. J. Richards. He graduated in December of 2011.